# Mass Transfer and Dispersion Processes in Connected Conductivity Structures: Simulation, Visualization, Delineation and Application

by

Brendan Anderson Zinn

B.S., Physics, University of Virginia (1996)

Submitted to the Department of Civil and Environmental Engineering
In partial fulfillment of the requirements for the degree of

Doctor of Philosophy in Hydrology

at the

MASSACHUSETTS INSTITUTE OF TECHNOLOGY

June 2003

Author.......................................

Department of Civil and Environmental Engineering
April 18, 2003

Certified by.......................................

Charles F. Harvey
Associate Professor, Civil and Environmental Engineering
Thesis Supervisor

Accepted by............

Oral Buyukozturk
Chairman, Department Committee on Graduate Students

# Mass Transfer and Dispersion Processes in Connected Conductivity Structures: Simulation, Visualization, Delineation and Application

by

Brendan Anderson Zinn

Submitted to the Department of Civil and Environmental Engineering
on May 9, 2003, in partial fulfillment of the
requirements for the degree of
Doctor of Philosophy in the field of Hydrology

## Abstract

This thesis focuses on mass transfer behavior, i.e., tailing, in solute transport, and on hydraulic conductivity heterogeneity. Macrodispersive theory, generally used to incorporate heterogeneity into solute transport, does not account for this tailing and makes assumptions about the structural characteristics of the heterogeneity, specifically that the field is multivariate gaussian.

We move away from the multigaussian assumption to focus on the concept of connected pathways of high or low conductivity. We first motivate the importance of connected extreme conductivity values through the numerical creation of two-dimensional conductivity fields with nearly identical univariate conductivity distributions and covariances, but with varying connectedness of extreme values. We simulated flow and transport through these fields, using a particle tracking approach that incorporates advection and diffusion. We demonstrate that connectedness impacts flow by influencing the effective conductivity of the field, and connected high conductivity fields with relatively high variance displayed mass transfer behavior, driven by both advective and diffusive processes.

We then conducted laboratory experiments to study three flow situations demonstrated by the first part of the work – classic dispersion, diffusion-driven mass transfer, and advection-driven mass transfer. By simultaneously measuring outflow concentration and the spatial distribution of solute in the tank, we demonstrate different breakthrough characteristics driven by different small-scale processes. Outflow concentrations match excellently with established models in the case of diffusive mass transfer and dispersion, and relatively well with a model we developed for the advective mass transfer scenario. We generalized the experimental results by creating connected binary conductivity fields, delineating the conditions of connectedness and conductivity contrast that drive the various transport.

Finally, we examine the implications of our earlier work, particularly the interplay between advection and diffusion in mass transfer. The presence of both processes creates late-time concentrations that are complex, but partially dependant on hydraulic gradients. We apply this to a hypothetical scenario of a pump-and-treat remediation – the existence of advective mass transfer creates situations in which solute mobilization can be sped up by pumping rate choices, and the complex interaction between mass transfer processes leads to more complex pumping rate decisions.

Thesis Supervisor: Charles F. Harvey
Title: Associate Professor, Civil and Environmental Engineering

# Acknowledgements

Reality can be a difficult concept to grasp, and I don't just say that because it took seven years to assemble this monstrosity. Reality, here and now, requires an uncountable number of events to have occurred in precisely the way they did. Thus, statistically speaking (in keeping with the theme of this thesis), the likelihood of things being the way they are is astronomical, bordering on impossible. And yet, all of those events must have happened, because here we are. I write this not because I plan to switch to a degree in philosophy, but merely to point out that the number of people and events that deserve credit for making this thesis possible are simply innumerable. There are, however, some people that deserve special recognition.

Firstly, I must thank the taxpayers of the United States for their financial support for seven years of work. Specifically, this support has come through research grants from the Department of Energy and National Science Foundation.

I would like to thank my intellectual mentors in this project. My professors, who taught me numerous things, both practical and theoretical, deserve thanks. My committee members, professors McLaughlin, Culligan, and Hemond provided valuable advise and had several helpful suggestions at various points. My work at Sandia National Laboratories would have been impossible without the assistance of several people – Bob Glass, who was generous with lab space and resources; Lucy Meigs, whose knack for organization and practical problem-solving was essential; Will Peplinski, the man who had the answer to every question; Roy Haggerty, who had many long-distance ideas; and to the others who helped out with advise, extra hands, and lunchtime repartee – Claudius Freiherr von Schwerin, Vince T. and Vince R., and Jim Brainerd. And special thanks to Sheila A., without whom I never would have gotten reimbursed for all of those trips.

And of course, by far my largest mentor on this project, my advisor, Professor Harvey. He is a man of boundless ideas, with an unflagging optimism for problem solving. Without these things, this thesis would not have been possible, and I hope these attributes have rubbed off at least a little.

I would like to thank my friends, both proximal and distant, who helped me keep my sanity at least partially intact. To Nagini, Karen, and Tres, with whom I exchanged so many emails that I finally learned how to touch-type. To Scott, Johanna, Holly, and Winston, with whom I wasted many an hour or lunchtime in conversation. True, we wasted so much time that you probably tacked on an extra year to completing this work, but it was definitely worth it.

Lastly, I must single out my family for eternal gratitude – mother, father, and brother. You've been there from the beginning as teachers, mentors, role models, and friends. Of all of the improbable variables that led to this point, yours was the most improbably wonderful, and the most impossibly important.

# Contents

# List of Figures

## Chapter 3

## Chapter 4

**Figure 4-3:** The completed experimental setup from two different perspectives. Shown at the top is the view, as seen by the camera, of the system, with the lightbox behind the tank. The valve system is used to flush the reservoir in the inflow manifold clean of dye prior to the experiment (see step #6 in the procedure). Clean water is then flushed through the dye-saturated tank, with tank outflow sent to the photometer. The bottom figure shows a side view of the path that light follows from the light box to the camera. 94

**Figure 4-4:** Experimental methodology checks. 4A shows mean estimated concentrations using the Beer-Lambert assumption versus the known actual concentration for several small areas in one of the tanks. Although linearity is maintained, the slope differs slightly from Beer-Lambert assumption. A best fit to our data is shown. 4B shows the coefficient of variation of the concentration estimates. Variability remains low until a sharp increase at a concentration of 0.1mg/l, which displays variability comparable to the magnitude of the measurement. 4C shows the percent error in total dye mass remaining calculated by tank image as compared to the actual dye mass (using known flow rates and volumes), for the three tanks. Errors tend to increase with time, in part due to deterioration in our accuracy as mean concentrations decrease. 95

**Figure 4-5:** Series of color images representing solute concentration as a function of time for each of the three tanks, all run with the same flowrate. Concentration is represented as fraction of initial, as noted on colorbar to the right. Close up of a single emplacement is shown for the two mass transfer cases, illustrating fundamentally different behavior, with one dominated by diffusion and the other by advection. 96

**Table 4-2:** Parameter estimates for the six breakthrough curves from the experiment. For all six, a mobile domain velocity and dispersivity were calculated. For the advective-diffusive and diffusive mass transfer experiments, a rate coefficient and partition coefficient were also calculated, with an assumed model of cylindrical diffusion. For the advective mass transfer case, we used are own model, estimating instead the (slow) velocity inside the emplacement, and the longitudinal dispersivity of this slow advection. Experiments were done by flow rate rather than hydraulic gradient, but the gradient for all experiments was on the order of 0.1. 97

**Figure 4-6:** Advective-dispersive experiment breakthrough curve data and best fits. Shape of the curves (and parameter estimates) indicates little mass transfer (tailing) is occurring. Sporadic data and noisy data was caused by air in outflow, necessitating use of hand samples instead of continuous flow cell reading in photometer. 98

## Chapter 5

## Chapter 6

## Appendix A

# Chapter 1

# Introduction

## 1.1 The Importance of Groundwater and Remediation

Groundwater is a resource of vital importance, as the vast majority of the planet's fresh water (in liquid form) is stored in the subsurface. Groundwater also interacts significantly with surface water bodies, and thus the health of groundwater has substantial implications for the health of rivers and lakes. With water demand increasing throughout the world, the importance of groundwater quality will continue to grow commensurately. Conflicts over groundwater allocation already occur in many arid parts of the world. In most places these conflicts are confined to the legal system, rather than violent struggle, but groundwater quality and allocation rights do play a role in violent conflicts, as well (e.g., the Gaza Strip).

Groundwater quality can be adversely affected by numerous sources. In some cases, contamination comes from accidental or negligent actions in a single location. In other cases, the contamination is caused by low-level effects from numerous sources (for example, pollution from lawn or crop fertilizer). Pollutants can take several different forms, ranging from NAPL's (non-aqueous phase liquids), which are not generally water-soluble, to contaminants that react with soils (e.g., arsenic), to conservative contaminants – chemicals that dissolve readily in water and are not generally reactive. Society must develop effective means to predict the fate and transport of solutes (contaminants that are dissolved into the groundwater) in order to predict the potential threat and pathways of dangerous chemicals in the subsurface.

Unfortunately, fate and transport in groundwater can be difficult to study, because, to state the obvious, it occurs underground. In the field it is often difficult to observe flow and transport at anything but large scales with sparse data, despite the fact that the subsurface in highly heterogeneous at a wide range of distance scales. This necessitates what are generally referred to as 'upscaled' models – because we are unable to explicitly describe undetectable small-scale variations in the subsurface, we try to incorporate the small-scale heterogeneity into a framework that successfully describes overall behavior at the large scale, which is generally our practical concern.

Remediation of groundwater is heavily reliant on upscaled models, as data about the details of the subsurface are usually limited. Estimated costs for remediating contaminated groundwater in the United States alone vary from tens of billions of dollars to more than one trillion dollars. Much of the variability in these cost projections stem from our uncertainty about the hydraulic characteristics of contaminated aquifers. In some cases, these characteristics can lead to a significant problem that has been observed at many remediation sites – the presence of rate-limited, or nonequilibrium, mass transfer. This creates what is commonly referred to as 'plume tailing', a long period of moderate to low concentrations of contaminant behind the main body of the contaminant plume. These tails can dramatically increase remediation time and costs. Further, the most commonly used upscaled solute transport model, macrodispersion, does not generally predict the occurrence of this behavior. In some cases, this nonequilibrium behavior is driven by particular characteristics of the contaminant, such as chemical interaction (e.g., sorption) between the contaminant and the soil or slow dissolution of nonaqueous phase liquids. However, many field sites have observed this behavior with conservative solutes, including the MADE site in Mississippi [*Harvey and Gorelick*, 2000] and the Livermore site in California [*LaBolle and Fogg*, 2001]. Clearly something must be occurring relatively small scales in the aquifer that the assumptions of macrodispersion do not account for. Sometimes this behavior is accounted for by grain-scale processes, such as intragranular diffusion, but this cannot explain all systems. In this thesis, we attempt to determine what kinds of heterogeneous structures might cause mass transfer behavior, and what some of the implications of these heterogeneities are. We restrict our study to conservative solutes, that is to say, contaminants that dissolve completely into the groundwater and do not react with any chemical components of the soil or groundwater, nor degrade or chemically change over time. This assumption may not be true for many (indeed most) contaminants, but the results from such studies allow for the greatest general applicability.

## 1.2 Thesis Structure – Aquifer Heterogeneity, Solute Transport Models and Our Work

Many researchers have considered how spatial heterogeneity in hydraulic conductivity affects fluid flow and solute transport through porous media. This heterogeneity is often characterized by a distribution, or histogram, of conductivity values, combined with a covariance, or variogram, function of separation distance. The histogram can be summarized by its mean and variance, and the spatial covariance can be described by its integral scale. When these statistics differ between two conductivity fields, the flow and transport behaviors through the two fields may be very different, while fields with similar first and second-order statistics are assumed to have similar flow and transport behaviors. In chapter 2, we detail background on the subject of aquifer structure and solute transport modeling. We discuss the multigaussian model of aquifer conductivity structure and the stochastic theory that derives from it. We also discuss the mass transfer model of solute transport, as well as the memory function method of describing tailing and late-time concentration. We also briefly discuss previous experiments in flow visualization, and how our experiments detailed in this thesis differ from them.

In chapter 3 of this work, we demonstrate that substantially different flow and transport behaviors can occur in isotropic log-conductivity fields. These fields share the same Gaussian histogram and the same covariance functions, and possess identical integral scales that are a small fraction of the total domain length. Thus, conductivity fields with the same conventional spatial statistics may produce very different groundwater fluxes, solute travel times, and solute spreading, because of spatial patterns that are not characterized by these conventional statistics. In other words, the full univariate distribution of conductivity values and the spatial covariance function for these values may not provide sufficient information to estimate effective flow and transport parameters. This can be particularly problematic for field characterization, where data is often quite sparse and first and second-order spatial statistics are the only characteristics easily ascertained. The reason behind this marked difference in behavior is due to the connectedness of extreme conductivity values, as we describe in detail in subsequent chapters of this work. Fields in which high values of conductivity are most connected possess effective conductivities that are higher than the multigaussian field, while fields with low conductivities most connected tend to have lower effective conductivities than multigaussian fields.

The primary focus of the work in this thesis is on those characteristics of conductivity fields that cause nonequilibrium mass transfer behavior, i.e., tailing. As noted in the previous section, mass transfer is often not considered for conservative solutes in smooth conductivity fields, but we demonstrate that it is possible simply by virtue of the structure of a field. We show that mass transfer can occur in conductivity fields that have the same histogram and covariance as a traditional multigaussian field, even though the multigaussian field does not demonstrate significant mass transfer behavior. The essential component for mass transfer is that the high values of conductivity are well-connected, and that the field possesses a relatively high conductivity variance. We also show that mass transfer behavior can be caused by both diffusion and advection in low velocity regions, and these processes produce solute tailing that appears qualitatively similar. Distinguishing between the two processes is important because tailing caused by slow advection will be affected by changes in hydraulic gradients, such as increased gradients induced by higher pumping rates from remediation wells.

Having used smooth, theoretical fields to motivate the importance of connectedness in causing tailing, we transition in chapter 4 to studying an actual, albeit artificial, porous medium with binary conductivity distribution in order to examine quantitative and qualitative behaviors predicted for connected fields. The experimental setup enables us to observe the processes occurring in a physical system and examine its output, i.e., we can simultaneously measure both the small-scale and upscaled transport behavior. This creates a real "aquifer" that confirms predictions from strictly numerical work. Our ability to control the conductivity structure and visualize the solute plume in fine detail marks a departure from field work, where even highly detailed field sites require a great deal of extrapolation from limited data points. Our ability to control the conditions of the experiment also allowed us to perform experiments under a relatively large range of scenarios, such as modifying head gradients and the conductivity contrasts. The experimental visualization successfully demonstrated the existence of three regimes of solute transport – traditional advection and dispersion, diffusion-dominated mass transfer, and advection-dominated mass transfer. The experiments further demonstrated that these different small-scale behaviors led to substantially different upscaled behaviors, which were able to observe in the breakthrough curves produced by the experiments. The design of the experiments also allowed us to check upscaled results for some experiments against known analytical solutions, and we found good agreement between analytical models and our results in such cases. In the case of the advective mass transfer scenario, we developed our own simple model to fit the breakthrough.

In Chapter 5, we extend the results of the specific system used in chapter 4 to more generalized conclusions. This is done with numerical simulations performed on binary conductivity fields in which one of the two conductivity values was more connected that the other. The results of these simulations agreed well with the results of the experiments. Numerical simulations allowed us to create more complex structures and control solute and aquifer characteristics more easily, and such simulations are much less time intensive than laboratory experiments. From these simulations (with support from the experimental visualizations), we were able to draw conclusions regarding the approximate conductivity contrasts and process timescale ratios required to drive the various behaviors associated with connected fields.

We found from these simulations that solute transport in these binary fields can fundamentally be divided into fields with mass transfer (requiring high conductivity variance and that the larger conductivity be the most connected), and fields without mass transfer (all other combinations of variance and connectedness). Within the fields that display mass transfer behavior, the type of mass transfer depends on the ratios of various process time scales. If the average time to advect through the mobile domain is larger than both the characteristic time to advect through low velocity regions and the characteristic time to diffuse through low velocity regions, equilibrium mass transfer dominates. If the characteristic time to advect and diffuse is smaller than mobile domain advection time, then either advective or diffusive mass transfer will occur, with whichever process is faster dominating the overall mass transfer.

This regime delineation that we develop has significant applicability for solute transport in connected conductivity fields with approximately bimodal conductivity distributions. We demonstrate this by showing agreement between our results and the detailed studies and simulations performed at the Livermore site [*LaBolle and Fogg,* 2001].

Finally, in Chapter 6, we examine our work in the context of the memory function model of mass transfer, as well as the practical meaning of our work in the previous three chapters. We demonstrate that the memory function can be partially dependent on the hydraulic gradient of a system. This goes against the general assumption that the memory function is an inherent property of an aquifer, unaffected by outside forcing. Despite this, we find that the memory function model is a relatively good predictor of late-time concentrations for alternate initial conditions, despite the fact that it does not account for advective mass transfer.

We also examine the implication of mass transfer that is controlled by both advection and diffusion and draw conclusions about the effect on late-time concentrations when both processes occur, as opposed to one process by itself. We find that overall rates of mass transfer are substantially higher when both processes are operating than either process by itself, and in some cases, they actually act to accelerate each other. However, we are confined to only general conclusions due to the fact that the specific breakthrough characteristics are highly dependent on the geometry of low velocity regions.

Lastly, we examine some practical applications to the presence of both advective and diffusive mass transfer. Because we can affect advective rates of mass transfer through pumping, the presence of advective mass transfer has important implications for remediation strategies, particularly in the case of pump-and-treat decisions. We attempt to minimize remediation costs that are a function of constant maintenance costs plus costs associated with treating solute-laden water. We find that optimal decisions can run counter to conventional decisions – in the case of an aquifer beginning saturated with solute, we sometimes find optimal pumping rates higher than the lowest possible rate. This is driven by the fact that we can control an aspect of the tailing to some degree, via our pumping choice, which introduces a complexity not usually accounted for.

In chapter 7, we close with general conclusions from the thesis. We also suggest several potential avenues of future study. Lastly, we include two appendices. One details our derivation of the change in covariance from the absolute value transform of a multigaussian field (discussed in Chapter 3), the other describes the simple used to fit the case of slow advection through a cylinder (Chapter 4).

## 1.3 Notation

We try throughout this work to be relatively consistent with notation, but it is impossible to avoid some changes as we change models, correlation lengths, or processes modeled. We have generally tried to at least keep parameters consistent in terms of what process they describe – for example, the Peclet number always relates macrodispersivity, not diffusion, to some length scale. The normalized diffusion coefficient is always represented by d′, though the length of normalization changes from field to field. Hopefully, the variable choices are sensible and self-evident, and we have tried to make sure each one is explicitly described within the text.

## 1.4 A Nota Bene About This Work

It will be abundantly clear, when reading through this thesis, that the issues we discuss in this work cover a huge amount of intellectual territory. This is mostly a product of the topics that our work touches on, rather than epic pretensions or aspirations of the work itself. Because of this, we try to keep the work focused with a combination of simplicity and pragmatism. Stochastic methods could be applied to our fields. Using multi-rate mass transfer models would give more complete descriptions of breakthrough tails. It would be helpful to apply this work to reactive transport. There are numerous avenues of research that are that are left open for study.

But these things distract from the basic questions we want to answer – does the advective-dispersive model best explain solute breakthrough in all conductivity fields, or should we use the mass transfer model? If both models have some degree of applicability, under what conditions would we want to choose one or the other? What processes fundamentally drive tailing in a conservative solute, and can we actually demonstrate their existence? What are the basic implications of having multiple processes drive mass transfer?

These questions tend not to have answers than can be summarized with a single number or ratio. We have not developed some master equation that accurately characterizes all solute transport scenarios. We cannot use the results of this work to characterize the breakthrough characteristics of a particular aquifer with an R-squared of 0.95. Our results are simply too general for that.

But the generality of the results is what makes them useful, in concert with effective site characterization. We can use the results to predict, for example, whether a certain aquifer might display significant tailing or not (as we do in the case of the Livermore site). We can guess whether advection or diffusion would dominate the tailing. And the results could be useable in reverse, i.e., we could determine aquifer characteristics from tracer tests, and whether they display tailing.

Ultimately, the specifics of any geologic site are unique to that location, and our work simply cannot incorporate that. Hopefully, though, when future hydrogeologists try to predict solute transport behavior in a specific aquifer, our work can provide some helpful hints as to what upscaled model will best describe the behavior.

# Chapter 2

# Background

Because the work detailed in this thesis is built atop a rather lengthy foundation of previous work, we have chosen to separate the background into it's own chapter. We further subdivide the background, covering conductivity structure and variability, solute transport modeling (macrodispersion and mass transfer), and experimental visualization of flow and transport in porous media.

## 2.1 Hydraulic Conductivity Structure and Variability

### 2.1.1 Multigaussian Fields and Connectedness

The multigaussian distribution is the standard statistical model used to describe spatially heterogeneous hydraulic conductivity. Our use of the term multigaussian is shorthand for a multivariate Gaussian distribution, which is detailed at length in numerous sources (e.g., *Anderson,* 1958). Conductivity values are lognormally distributed, described entirely by a mean and variance, and the structure of the field is described entirely by its covariance function. The multigaussian model is relatively tractable, and is the basis of analytical solutions for effective conductivity and macrodispersion fluxes [e.g., *Gelhar,* 1993*; Dagan,* 1989*; Cushman,* 1990]. While such solutions do not explicitly require multigaussian conductivity structure, the assume a field structure that is explained entirely by its mean and covariance, requiring a multigaussian structure if the correlation length is finite and significantly smaller than the size scale of the field.

One characteristic of multigaussian fields is that extreme values in the field are the least connected [e.g. *Journel and Deutch* 1993], which is to say that extreme values tend to cluster in isolated blobs, rather than form channels or structures that span the entire length of the field.

These characteristics have been quantified by *Journel* [1983], *Journel and Alabert* [1989], and *Gomez-Hernandez and Wen* [1998] using indicator variograms. *Xiao* [1985] showed that the integral scale for the median indicator is maximal, and symmetrically decreases at higher or lower values. This motivates our study of connectedness – we attempt to discern differences in flow and transport properties when the extreme values of conductivity form field-spanning structures instead of the median values.

### 2.1.2 Earlier Studies that Deviate from the Multigaussian Assumption

As mentioned in the introduction, the primary method of describing aquifer heterogeneity is through the univariate distribution of conductivity values and the covariance of these values. Although the multigaussian structural assumption is common, there are several scenarios that are known to deviate from it:

**(1)** Conductivity fields with a bi-modal distribution of values. Solute transport through these fields may display behavior best modeled by mass transfer, creating solute plumes with longer, more dilute tails than plumes transported through unimodal conductivity fields. [*Desbarat,* 1990; *Dagan and Lessoff,* 2001*; LaBolle and Fogg,* 2001*; Guswa and Freyberg,* 2000]

**(2)** Conductivity fields that are described by covariance functions with long integral scales relative to the domain length. Such fields exhibit large-scale structures, flow barriers and/or channels, that may control flow and transport, driving behaviors that differ from flow and transport in conductivity fields with short integral scales. [e.g., *Di Federico et. al.,* 1999]

**(3)** Conductivity fields that are composed of aligned layers. These fields have effective conductivity values and solute spreading behavior that differs from statistically isotropic fields. [*Matheron and de Marsily,* 1980]

As we demonstrate in this thesis, all of these behaviors can actually occur in a continuous conductivity field of gaussian univariate distribution and short correlation length, with tortuous instead of layered pathways. Thus these models may not necessarily be the explanation of mass transfer behavior in an aquifer – it may be connectedness that is driving the tailing.

### 2.1.3 Aquifers with Connected Pathways and Large Conductivity Variance

Conductivity fields with connected paths of extreme values may occur in a variety of geological formations. Several papers address the occurrence of flowpaths at both the small and large scales, as well as methods for characterizing such heterogeneity [e.g., *Anderson,* 1989; *Koltermann and Gorelick,* 1996; *Western, et al.,* 2001]. *Fogg* [1986], found that large scale structures in the Wilcox aquifer in Texas consisted of interconnected bodies of sands and clays, with flow controlled by the "continuity and interconnectedness" of the sands. *Labolle and Fogg* [2001] determined that high conductivity channels dominated the flow behavior at the Livermore site. Connectedness also has a clear presence in fracture flow, where, for example, *Silliman and Wright* [1988] concluded that connected higher conductivity channels existed in fractured granite in Arizona. On smaller scales, *Journel and Alabert* [1989] found connected channels in Berea Sandstone, as did *Tidwell and Wilson* [1999]. Connectedness may be an important feature in many conductivity fields, and therefore an important, if not dominant, control on solute transport.

In addition to connected conductivity structures, our results suggest that mass transfer behavior also requires large variance in hydraulic conductivity, variances that are higher than generally considered in macrodispersive stochastic theory. However, large variances in ln(K) are often found in nature. An aquifer composed of equal volumes of silt regions with $K=10^{-6}$ m/s and sand regions with $K=10^{-3}$ m/s, would have a ln(K) variance of 12. The MADE site in Mississippi, which has both small silt and sand regions, may have a centimeter-scale ln(K) variance as large as 20 [*Harvey and Gorelick,* 2000], although variance at the meter-scale (which averages out small-scale variability) is considerably smaller, ~4 as measured by borehole flowmeters [e.g., *Feehley, et al.,* 2000]. The Wilcox aquifer in Texas [*Fogg,* 1986] has high variance (ln(K) variance ~ 10), as does the Livermore site (ln(K) variance > 20), but at a large scale [*LaBolle and Fogg,* 2001]. Well tests on the Culebra Dolemite, a key facies at the WIPP site, showed a variation in hydraulic conductivity of six orders of magnitude [*Meigs and Beauheim,* 2001]. Our results agree in general terms with results from these sites, suggesting that our general conclusions about connectedness and high variance in conductivity fields are applicable to these field sites, and probably others.

It is important to note that although many aquifers do show connectedness and high variance, these characteristics are not present in all aquifers. For example, the Cape Cod and Borden sites display relatively low variance in hydraulic conductivity, and there are certainly aquifers in which lognormal distributions of conductivity seem accurate (e.g., *Hoeksema and Kitanidis*, 1985). It is also important to keep in mind the question of scale, as the variance of conductivity in an aquifer is highly dependent on the scale at which it is studied. The work by *Tidwell and Wilson* [1999] suggests that as the scale of measurement increases, the variability of conductivity decreases. This also seems to be the case at the MADE site, where large-scale ln(K) variance is approximately 4, but the centimeter-scale variance is closer to 20. We do not claim that higher or lower variance fields are inherently more accurate, only that one must be careful in assumptions about variance and distance scale. Fortunately, our work in this thesis covers a range of variance scales and multiple formulations of conductivity structure, so the results can describe many (though certainly not all) aquifers in the real world.

### 2.1.4 Previous Study of Connected Conductivity Fields

Both *Wen and Gomez-Hernandez* [1997] and *Western, et al.* [2001] compared transport through two-dimensional conductivity fields that had similar spatial statistics but where some fields contained large-scale connected features. *Wen and Gomez-Hernandez* [1997] modified an isotropic multigaussian field to create anisotropic non-multigaussian fields with layered structures of high or low conductivity. They showed that advective transport in these anisotropic fields differed from advective transport in the isotropic multigaussian conductivity field, despite identical histograms and non-directional covariance functions (which averaged out anisotropy in the field with connected structures). *Western, et al.* [2001] constructed two continuous fields with similar non-directional covariance functions; one with disordered statistically isotropic high conductivity regions, and one crossed by two large flow channels that created quick solute breakthrough. They characterized the difference between the two fields with connectivity statistics, a function that charts the probability that a certain subset of conductivity values are all connected to one another by values within that same subset (similar to the concept of percolation thresholds). Both of these studies, which consider solute advection but not diffusion, best describe transport through large-scale heterogeneity where the effects of small scale mixing can be ignored.

To our knowledge, this is the first study to compare upscaled flow and transport behavior in fields with the same Gaussian log-conductivity histogram and second order statistics including the same directional covariance functions with no artificially imposed large structures. We compare behavior among statistically isotropic fields, rather than between an isotropic field and an anisotropic field. This study also differs from previous studies in that it considers diffusion, allowing the work to be applied to both small and large scales.

## 2.2 Modeling of Flow and Transport in a Multigaussian Field – Macrodispersion

### 2.2.1 Effective Conductivity

The effective hydraulic conductivity of a multigaussian field appears to be well described by Matheron's [*1965*] conjecture [e.g., *Dagan, 1989; Gelhar,1993; Renard and de Marsily, 1997*], which, for an isotropic two-dimensional log-conductivity field, reduces to the geometric mean. This holds true even for high variance mulitgaussian fields, but does not hold true for other isotropic fields such as blobs of one conductivity embedded in a matrix of a different uniform conductivity. Upper and lower bounds can be set on the effective conductivity of any heterogeneous collection of conductivity values. The upper bound of the effective conductivity is the arithmetic mean, and the lower bound is the harmonic mean, which correspond to flow through a perfectly layered system, parallel and perpendicular to the layering, respectively.

### 2.2.2 Velocity Variability and Macrodispersion Coefficients

Solute transport in porous media is often described with the advective-dispersive model:

$$\frac{\partial C}{\partial t} = -\bar{v}\nabla C + \nabla\left(\bar{\bar{D}}\nabla C\right) \qquad (1)$$

Where C is the solute concentration, v is the fluid velocity vector, and D is the dispersion coefficient tensor. A large body of literature relates the dispersion coefficient, or macro-dispersion coefficient, to the variance and integral scale of the log-conductivity field, as reviewed in *Dagan* [1989], *Gelhar* [1993] and *Cushman* [1990]. The macrodispersion coefficient describes solute spreading due to variation in the velocity caused by spatial heterogeneity of conductivity at a smaller scale than is explicitly modeled. The first-order approximation of velocity variance in both the x- and y-directions (parallel and perpendicular to flow, respectively), for a two-dimensional, isotropic multigaussian field from *Gelhar and Axness* [1983] is:

$$\sigma_{v_x}^2 \approx \frac{3}{8}\sigma_Y^2 K_{\mathrm{eff}} i \qquad (2a)$$

$$\sigma_{v_y}^2 \approx \frac{1}{8}\sigma_Y^2 K_{eff} i \tag{2b}$$

where Y=ln(K) and $\sigma_Y^2$ is the variance of Y. $K_{eff}$ is the effective conductivity (geometric mean) of K, and i is the hydraulic gradient. The late-time macrodispersion coefficient for relatively small variance is derived from the velocity statistics to be:

$$D = A\overline{v} \approx \lambda\sigma_Y^2\overline{v} \tag{3}$$

where A is the macrodispersivity, $\overline{v}$ indicates mean velocity, and the integral scale, λ, is assumed to be finite. Many studies consider extensions and improvements of these equations. Here, we found that the simple first-order results were sufficiently accurate to describe our numerical results in multigaussian conductivity fields.

We also found it useful to compare some of our results to analytic results for macrodispersion in stratified aquifers. For flow perfectly parallel to layered conductivity variations, *Gelhar, et al.* [1979] found that if the hydraulic conductivity is described by a restricted class of covariance functions that integrate to zero (i.e. hole effect covariance functions), then the macrodispersion coefficient asymptotically approaches a value that increases quadratically with the mean velocity and decreases with the diffusion coefficient:

$$D = d + B\frac{\overline{v}^2}{d} \tag{4}$$

where d is the apparent diffusion coefficient and B is a coefficient that depends on the statistics of the conductivity layers. These results are analogous to classical Taylor-Aris dispersion in laminar flow through straight tubes or fractures [*Taylor,* 1953*; Aris,* 1956]. *Matheron and deMarsily* [1980] showed that if the hydraulic gradient is not exactly parallel to stratification, as often happens under natural conditions, the macrodispersion coefficient approaches an asymptote that also increases quadratically with the mean velocity and decreases with the diffusion coefficient. In this case, the covariance function need not integrate to zero, so the result holds true for commonly used covariance functions.

## 2.3 The Mass Transfer Model

Researchers have also employed rate-limited mobile-immobile domain mass transfer models to describe solute transport through heterogeneous media. In addition to describing intragranular diffusion and sorption, these models are often used to describe transfer of solute in and out of low conductivity regions [e.g., *Barenblatt.,* 1960]. Most studies consider physical mass transfer to be driven by diffusion, but some consider slow advection in and out of low permeability regions. Recently, *Harvey and Gorelick* [2000] have used simple mass transfer models to explain non-reactive transport through the sedimentary aquifer at the MacroDisperison Experiment (MADE) field site. *Feehley, et al.* [2000] and *Julian, et al.* [2001] have corroborated these results. In that particular aquifer, the variability in hydraulic conductivity is large and the macrodispersion model failed to describe the observed solute behavior as well as it has in more homogeneous aquifers [e.g., *Freyberg,* 1986; *Hess, et al.,* 1992]

### 2.3.1 First-Order Mass Transfer Model

The first-order mass-transfer equation may be coupled with the advective dispersive equation as:

$$\frac{\partial C}{\partial t} + \beta \frac{\partial S}{\partial t} = -v_{\mathrm{mobile}} \nabla C + \nabla\left(\underline{\underline{D}} \nabla C\right) \tag{5a}$$

$$\frac{\partial S}{\partial t} = \alpha(C - S) \tag{5b}$$

where S is the concentration of the solute in the immobile domain. This model assumes that there is a mobile domain (i.e., a region through which solute advects at the groundwater velocity in mobile region, $v_{\mathrm{mobile}}$), and an immobile domain, with solute transfer between the two domiains rate-limited. The ratio of rate-limited or nonequilibrium immobile domain pore space to mobile domain pore space is given by the capacity coefficient, $\beta$. The rate at which solute moves between these two domains is controlled by $\alpha$, which depends on the particular size and geometry of these regions. More sophisticated diffusive mass transfer models account for a range of mass-transfer rate coefficients [*Haggerty and Gorelick,* 1995], and have been shown to better represent field data [*McKenna et al.,* 2001]. However, multi-rate mass transfer entails much more complicated estimation, and hence we chose to use a simpler model in this thesis.

Some researchers [e.g. *Griffioen, et al.,* 1998] have also considered advective mass-transfer. *Guswa and Freyberg* [2000] recently demonstrated that advection through low permeability inclusions can lead to breakthrough curves with tailing very similar to that caused by diffusion in and out of low permeability regions. Thus, from a single experiment, it could be very difficult to tell the two processes apart.

### 2.3.2 The "Memory Function" Model of Mass Transfer

The so-called memory function, which we will often refer to as g(t) from this point forward, falls out of a formulation of mass transfer that does not prescribe a specific model to the mass transfer. This model is discussed at length in *Haggerty, et al.* [2000].

The memory function method classifies mass transfer as a general source-sink term, dependent on time and space, but not necessarily explicitly described. In one-dimensional form, the transport equation is expressed as:

$$\frac{v_x}{R_x}\left(\alpha_L \frac{\partial C}{\partial x} - C\right) = \frac{\partial c}{\partial t} + \Gamma(x,t) \qquad (6)$$

with $R_x$ the retardation factor (which we set to 1 for all of our work), $\alpha_L$ the longitudinal dispersivity, $v_x$ the mobile domain velocity in the x-direction, and $\Gamma(x,t)$ the source-sink term. The derivation assumes that solute has a characteristic advection time through the mobile domain, $t_{ad}$, which leads to the assumptions at late time that:

$$\alpha_L \frac{\partial C}{\partial x} << C, \qquad t >> t_{ad} \qquad (7a)$$

$$\frac{\partial C}{\partial t} << \Gamma(x,t), \qquad t >> t_{ad} \qquad (7b)$$

Note that this requires the time scale of mass transfer to be significantly larger than the time scale of advection. These two equations are simply mathematical expressions of the fact that at late time (i.e., in the tail of the plume), dispersion has a minimal effect, and the immobile domain dominates the solute concentration instead of variations in the mobile domain. Factoring equations 7a and 7b into equation 6 gives us:

$$-v_x \frac{\partial C}{\partial x} = \Gamma(x,t) \qquad (8)$$

Again, assuming late time (and we have dropped the retardation factor). The derivation also assumes that $\Gamma(x,t)$ is spatially uniform (that is, we assume one value of $\Gamma(x,t)$ for the entire domain), allowing us to calculate concentration by integrating equation 8 over space:

$$C(x = L,t) = -\int_0^L \frac{\Gamma(t)dx}{v} \qquad (9)$$

where L is the distance traveled. Solving the integral gives a late-time concentration:

$$C(x = L,t) = -t_{ad}\Gamma(t), \qquad t >> t_{ad} \tag{10}$$

Dealing with the source-sink term requires an assumption of linearity in the mass transfer process, and spatially-uniform initial conditions. We can then express Γ(t) as a convolution (following the method of *Carrera, et al.* [1998]):

$$\Gamma(t) = \int_0^t g(\tau)\frac{\partial C(t-\tau)}{\partial \tau} = \frac{\partial C}{\partial t} * g = C * \frac{\partial g}{\partial t} + cg_0 - c_0 g \tag{11}$$

where g(t) is commonly referred to as the "memory function" (units of inverse time). A closed-form expression is created by applying temporal boundary conditions for a specific solute transport scenario (again, detailed at greater length in *Haggerty, et al.*, 2000). If we assume that the immobile domain begins with no solute in it, and a dirac pulse of solute is input to the domain at time zero, we can approximate the concentration by:

$$C \cong m_0\delta(t) \tag{12}$$

In addition to the zero time boundary, we can impose an infinite time boundary, which requires that concentration go to zero. Applying these boundary conditions and exploiting the convolution, gives a solution for the source-sink term of:

$$\Gamma(x,t) \cong m_0\frac{\partial g}{\partial t} - C_0 g \tag{13}$$

and finally, plugging this expression into equation 10 gives us:

$$C \cong t_{ad}\left(C_0 g - m_0\frac{\partial g}{\partial t}\right), \qquad t >> t_{ad} \tag{14}$$

which is the late-time concentration of the solute plume. This particular form is highly advantageous due to the fact that one of the two terms will drop out in most transport scenarios, as $C_0$ is the concentration in the immobile domain at time zero, and $m_0$ is the solute mass injected at time zero. For a case where the mobile and immobile domains begin at uniform concentration (i.e., equilibrium), and we flush domain with clean water, the $m_0$ term drops out. For a case where the domain is initially clean, and we inject a dirac pulse (for example, the flux-proportional line used in some of our particle tracking simulations), the $C_0$ drops out.

## 2.4 Evolution of Transport Coefficients over Travel Path

The macro-dispersion literature describes solute transport as pre-asymptotic before the time-rate-of-growth of the second spatial moments of a plume stabilizes both from an Eulerian [e.g., *Gelhar,* 1993] and Lagrangian [e.g., *Dagan, et al.,* 1992] point of view. The travel distance for the effective dispersion coefficient to approach asymptotic conditions has been calculated to be on the order of 10 correlation lengths [*Dagan,* 1984]. This notion of pre-asymptotic behavior does not apply directly to mass transfer models, as the spreading and tailing caused by mass-transfer occur only over time scales on the order of $\alpha^{-1}$. In contrast to the macro-dispersive model, the mass transfer model predicts a non-constant time-rate-of-growth of the second spatial moments of a plume over times scales on the order of $\alpha^{-1}$, even though all of the coefficients are constant. At time scales much larger than $\alpha^{-1}$, transport may be modeled with a simple retardation factor, and the effects of rate-limited mass transfer are no longer evident. Thus the tailing behavior that the mass transfer model produces is a pre-asymptotic effect. However, it is this effect that we wish to understand and to model because of its importance for practical problems such as contaminant cleanup.

## 2.5 Visualization of Flow in Porous Media

Visualization of flow in naturally occurring rocks and soils is an inherently difficult process, as it generally involves imaging of tracers in an opaque sample. Modern technology may eventually enable detailed three-dimensional images of solute transport (for example, use of MRI techniques [e.g., *Ogawa et al,* 2001*; Chen et al.*, 2002]). However, traditional methods of imaging real rock have used high-energy visualization methods that can penetrate the medium, depth-averaged into a two-dimensional image [e.g., *Tidwell and Glass,* 1994*; Altman et al.*, 1998; *Tidwell et al,* 2000].

An alternative is to construct the porous medium and forgo using real rock. Fabrication can be done in a way to target specific characteristics of interest, which is a potential advantage. However, the creation of an artificial porous medium can be troublesome, with the risk of the medium not properly mimicking the desired physical characteristics. It is also difficult, if not impossible, to create a sample which can entirely mimic depositional patterns, diagenesis, or consolidation.

Another issue of consideration is the size of the experiment, as a range of experimental scales is feasible [e.g., *Silliman*, 1995; 2001; *Tidwell et al*, 1995; *Lennox*, 1997; *Schroth, et al*, 1997]. The scale will affect the time scale of relevant processes (e.g., diffusion), and can affect resolution, though this is also a function of imaging technique

A common technique for porous medium visualization is the use of visible light transmission [e.g., *Tidwell and Glass*, 1994, *Darnault et al*, 1998*; Welker et al.*, 1999*; Gramling et al.*, 2002]. This method generally requires that the medium be transparent or very thin, and needs a powerful light source to achieve good concentration resolution. One method for creating a translucent porous medium with a feasible magnitude of light transmission is to use glass beads [e.g., *Oostrom et al.*, 1992*; Corapcioglu and Fedirchuk*, 1999]. High-quality packed beads possess many useful characteristics, including high transparency, relatively predictable conductivity and porosity, low reactivity, low intragranular porosity, and good durability. The colored dye FD&C Blue #1 (a.k.a. Brilliant Blue FCF) possesses several favorable characteristics for simulating and visualizing a conservative solute, including strong linearity, low reactivity, and a distinct primary absorbance peak [*Norton and Glass,* 1993; *Flury and Fluhler*, 1995*; Darnault et al*, 1998]. The one concern with the dye is that it can react with organic components in natural soils [e.g., *Allaire-Leung et al.*, 1999], but this is not an issue for our experiment.

Conductivity contrasts of the size we are interested in have rarely been studied in the laboratory, particularly for visualization purposes. This is especially true of artificially constructed porous media, which are difficult to create. Artificially constructed laboratory visualization studies have generally possessed a conductivity contrast of no more than a factor of 20 between the highest and lowest conductivity values [*Silliman*, 1995; 2001; *Schroth et al*, 1997; *Berkowitz et al*, 2000; *Glass, et al*, 2000]. The one exception in which conductivity contrast is large is the case of fracture flow [e.g., *Tidwell, et al.*, 1995]. Tailing has been observed in some of these experiments, but the behavior is generally due to other factors such as NAPL dissolution [*Schroth et al*, 1997] or preasymptotic length scales [*Berkowitz et al*, 2000], while we are interested in tailing for conservative solutes at relatively large ($\geq 10\lambda$) distance scales.

# Chapter 3

# The Importance of Connected Conductivity Structures

## 3.1 Introduction

As previously mentioned, the standard approach to modeling transport of conservative solutes is with macrodispersion and associated stochastic methodologies, and implicit in these is an assumption of multigaussian conductivity structure. In this chapter, we motivate the importance of connected conductivity. We do this by comparing flow and transport in a standard multigaussian field, in which median conductivities are the most connected, to flow and transport in fields with high conductivities most connected and fields with low conductivity values most connected. Despite the fields having different characteristics of connectedness, they are specifically designed to have nearly identical univariate conductivity distributions and covariance structures.

It should be noted that although connected features certainly appear in natural geologic formations, geology is not always as smooth as our fields. Despite that, we focus on fields with continuous distributions in order to demonstrate the importance of connected extreme values of conductivity. By keeping the fields smooth and continuous, we ensure that the only significant structural difference between the fields is their connected structures, and thus that any flow and transport differences are driven by that connectedness. We attempt to address geologies possessing less continuous distributions of conductivities in subsequent chapters.

We show that connectedness does indeed influence both flow and transport by means of particle tracking simulations modeling advection and diffusion, and demonstrate that fields with connected high conductivities display effective conductivities that are higher than those of the multigaussian field. These fields also display mass transfer at higher variances. The multigaussian fields and fields with connected low conductivity values display little or no mass transfer. We also find mass transfer driven by both slow advection in low conductivity areas and diffusion into and out of these low conductivity areas.

All of this points to the conclusion that connectedness actually does have a huge impact on flow and transport. Not only can it drive changes in basic parameters, such as mean fluid velocity in the field, it can actually affect what upscaled model is required to describe conservative solute transport in that field.

## 3.2 Methods

### 3.2.1 Generation of Connected Fields

We modeled transport behavior in three types of conductivity fields: (1) a standard multigaussian field; (2) a field with connected patterns of high conductivity (which we henceforth refer to as the "connected" field), and; (3) a field with disconnected high conductivity, but connected patterns of low conductivity (the "disconnected" field). All three of these fields share nearly identical univariate distributions and spatial covariance functions. Thus, all three conductivity fields share the same basic statistics (the first and second statistical moments) but their structures differ in how the high and low values are connected.

The isotropic multigaussian field (figure 1a) consisted of a regular grid of 800 by 500 point values representing grid blocks generated by the sequential Gaussian simulation algorithm [*Deutch and Journel*, 1997] using a Gaussian covariance function. The correlation of the field as a function of separation distance is shown in figure 2. The integral scale is approximately 1.1 percent of the length of the field, 9 blocks.

The connected (figure 1c) and disconnected fields were generated through a transformation of the multigaussian field in four steps:

**(1)** The absolute value of the multigaussian field (zero-mean, unit-variance) in figure 1a was calculated. This transform shifts extreme values to become high values, and values originally close to the mean become low values.

**(2)** The histogram of the values in the field was converted back to a univariate Gaussian distribution by mapping the CDF value at each point to a standard normal CDF. This transformation can be written explicitly as:

$$Y' = \sqrt{2}\mathrm{erf}^{-1}\left(2\mathrm{erf}\left(\frac{Y}{\sqrt{2}}\right) - 1\right) \tag{1}$$

where Y′ are the transformed values of ln(K) and Y are the original values. This creates a field in which the extreme low values are connected and the high values form isolated blobs – the field shown in figure 1b.

**(3)** The block size of the field was increased so that the integral scale matched that of the original multigaussian field. This provided the final disconnected field.

**(4)** The connected field (figure 1c) was then generated from the disconnected field by reflecting the values of the disconnected field around the mean, so connected patterns of low conductivity become connected flow paths of high conductivity.

Appendix A gives an analytical solution for the covariance of the transformed field (after step 1, but before step 2), and shows how the integral scale is reduced by the absolute value transform, which necessitates step 3. The correlation functions for the multigaussian field and the connected fields, along with the analytic results, are shown in figure 2. The results from Appendix A are in close agreement with the calculated correlations from the realization, indicating that the normal-scores transform (step 2) has only a minor effect on the covariance function, despite the fact that the transform is non-linear. The integral scale of the multigaussian field and the connected field differ by a factor of 1.86. Therefore, the separation distance between points was increased by the factor of 1.86 (step 3, shown above), and the number of rows and columns was reduced by a factor of 1.86 in order to maintain the same domain size.

An alternative approach is to use the covariance function of the connected field (after steps 1 and 2) to generate a new multigaussian field. This approach provides the possibility of producing identical, rather than nearly identical, covariance functions. However, for a single random field the variability between the experimental correlation function and the function used to generate the field is typically as large as the difference between our connected and multigaussian fields.

Figure 1c shows the final connected field after all four of the steps above. The disconnected field is simply the inverse, or reflected, version of the connected field, so the high conductivity flow channels become low conductivity barriers. The connected and disconnected fields now have histograms and experimental covariance functions (figure 2) that are nearly identical to those of the multigaussian field. These ln(K) fields are used in all of the following simulations of flow and transport in this chapter.

### 3.2.2 Simulation of Flow and Transport

A head gradient was applied across the field, with constant head boundaries on the left and right borders, and no-flow boundaries on the top and bottom, driving flow from left to right. The steady-state, two-dimensional flow equation was solved with a finite difference approximation. The velocity field was calculated along block edges by taking the difference in the heads of the two adjoining blocks, multiplying by the mean conductivity, and dividing by a uniform porosity.

Although we will work with dimensionless parameter groups, it is perhaps useful to think of the following possible parameter values: a length of 8m (800 1cm square blocks), effective conductivity of $1.8*10^{-6}$ m/s (16 cm/day ), gradient of 0.02, and porosity of 0.3. This leads to a mean flow velocity for the multigaussian field (shown in figure 1a) of approximately $1.2*10^{-7}$ m/s (1.1 cm/day). Note that flow velocities in the other fields will be different, as discussed in the results section.

Conservative solute transport (advection and diffusion) was simulated with particle tracking by combining two commonly used methods – the constant time-step method [e.g., *Goode*, 1990] and the "boundary to boundary" method [*Pollock*, 1988]. The boundary method is more accurate and computationally efficient than the time step method when only advection is simulated. However, it cannot be directly implemented when diffusion is considered.

We combined the strengths of both approaches (at some cost in computational efficiency) by modeling diffusion as random displacements during discrete time steps and using the boundary method to integrate the interpolated velocity over time steps. Instead of integrating the velocity over the particle's full path across the block domain, we integrated through time for a duration equal to the time step. This method has the advantages of tracking advective trajectories, while approximating the simultaneity of advection and diffusion. Positions of particles within a block after a certain amount of time has elapsed were solved analytically with linear interpolation using equation 12 from *Pollock* [1988]. Diffusive movement (with a spatially homogeneous diffusion coefficient) was then incorporated by adding a zero-mean normally distributed random displacement in both the x and y direction, $r_x$ and $r_y$, with

$\sigma = \sqrt{2d\Delta t}$. To insure against excessively large advective displacements in blocks with large velocities, we set $\Delta t$ such that the maximum velocity in the entire field multiplied by $\Delta t$ did not exceed a distance of $0.5*\Delta x$.

The numerical accuracy of the scheme was verified against two known solutions: the solution for Taylor dispersion in a parabolic velocity field [*Taylor,* 1953], and the solution for advection and diffusion through a high conductivity matrix with embedded circular impermeable regions [*Goltz and Roberts,* 1986], which includes sharp interfaces between zero and finite velocities. The simulations of the Taylor-Aris flow showed excellent agreement, with both the first and second spatial moments of a particle plume agreeing with the theoretical moments to within 0.1 percent. The comparison between the theoretical moments of the embedded cylinders scenario with our simulated particle plume were also good, with about 1 percent error on the second moment, which we believe is caused in part by the use of a finite number of particles, and in part by the fact that the circular regions must be approximated with a circular assemblage of squares.

In each of the numerical experiments described below, 1000 particles were initially distributed on a vertical line located 19 correlation lengths from the left boundary. We considered two distributions of particles along this vertical line. In the first method, the density of particles is proportional to the velocity at a given point. In the second method, the particles are evenly spaced. The first, flux-proportional, method has the advantage that it better simulates how particles would be introduced into an aquifer from a well screen, or into an experimental column or box along a constant head boundary. It is analogous to a dirac pulse in the flux concentration [*Kreft and Zuber*,1978]. The second method, in which particles begin evenly spaced, has the advantage that comparison to theoretical results from the advective-dispersive model is easier, with an initial condition that is simply a dirac pulse in the resident concentration. *Vanderborght, et al.* [1998] determined that for a two dimensional system with an exponential variogram and ln(K) variance of approximately 2.5, the choice of initial conditions could affect transport parameters to a distance of about three correlation lengths. Theoretical predictions with the mass-transfer model can easily be made with either initial distribution of particles. The velocity-proportional case corresponds to an initial condition with zero immobile solute, and the evenly spaced case corresponds to an initial condition where the mobile and immobile concentrations are at equilibrium.

Breakthrough was recorded at another vertical line that was 67 correlation lengths from the injection line (e.g., 600 blocks in the multigaussian field, 323 blocks in the connected and disconnected fields). This allows comparison of consistent tracking distances in the three fields, and is also a distance large enough to assure that the solute plume passed through many correlation lengths of heterogeneity.

### 3.2.3 Estimation of Effective Parameters from Breakthrough Curves

The solute transport model used to fit the simulated breakthrough curves incorporates both dispersion and mobile-immobile domain mass transfer. The immobile domain is divided into one subdomain that contributes to rate-limited mass transfer over the time scale of observations, and a second noncontributing subdomain in which mass transfer is too slow to significantly affect solute concentrations over the time scale of observations. Hence our model is a two-site model, where one portion of the immobile domain has a finite mass transfer rate coefficient, and another portion has a rate coefficient of zero. The mobile domain velocity is then:

$$v_{mobile} = \overline{v}(1+\beta_{tot}) = \overline{v}\left(1+\beta_{noncont}+\beta_{noneq}\right) \tag{2}$$

where $\overline{v}$ is the average velocity in the aquifer as a whole, and $\beta_{tot}$, the ratio of all immobile domain pore space to the mobile domain pore space, is the sum of the capacity coefficients for both the noncontributing subdomain, $\beta_{noncont}$ and the nonequilibrium subdomain, $\beta_{noneq}$.

In this chapter, we will employ the one-dimensional form of the mass transfer equation (equation 5 in chapter 2), which (incorporating equation 2) is:

$$\frac{\partial C}{\partial t}+\beta_{noneq}\frac{\partial S}{\partial t} = -\overline{v}\left(1+\beta_{noncont}+\beta_{noneq}\right)\frac{\partial C}{\partial x}+A\overline{v}\left(1+\beta_{noncont}+\beta_{noneq}\right)\frac{\partial^2 C}{\partial x^2} \tag{3a}$$

$$\frac{\partial S}{\partial t} = \alpha(C-S) \tag{3b}$$

This form is similar to that used by *Harvey and Gorelick* [2000] to model transport at the MADE site, with the exceptions that they incorporated a retardation factor to describe pore-scale immobile regions, and they did not consider a noncontributing domain. Because the mean groundwater velocity was not known at the MADE site, the effects of such a noncontributing domain, if it existed, would have been accounted for by a larger estimate of the mean velocity.

Equation 3 can then be non-dimensionalized by normalizing the distance by the length of the domain, L, and time by $L/\bar{v}$, the mean time for fluid to flow across the domain:

$$\frac{\partial C}{\partial t'} + \beta_{noneq}\frac{\partial S}{\partial t'} = -\left(1 + \beta_{noncont} + \beta_{noneq}\right)\frac{\partial C}{\partial x'} + \frac{\lambda}{L}\mathrm{Pe}\left(1 + \beta_{noncont} + \beta_{noneq}\right)\frac{\partial^2 C}{\partial x'^2} \tag{4a}$$

$$\frac{\partial S}{\partial t} = \mathrm{Da}(C - S) \tag{4b}$$

where the non-dimensional parameters are:

$$x' = \frac{x}{L} \tag{5a}$$

$$t' = t\frac{\bar{v}}{L} \tag{5b}$$

$$\mathrm{Pe} = \frac{A}{\lambda} \tag{5c}$$

$$\mathrm{Da} = \alpha\frac{L}{\bar{v}} \tag{5d}$$

Note that the capacity coefficients ($\beta$'s) are already dimensionless. Pe is the common notation for the Peclet number, while Da, the Damköhler number (sometimes denoted $D_a$), is similar to the parameter in *Bahr and Rubin* [1987] except that their Damköhler number is formulated for kinetic chemical sorption instead of diffusive mass transfer. Also note that equation 4a includes a non-dimensional factor that is the ratio of the integral scale to the length of the domain ($\lambda/L$). We address the importance of this parameter in a later section of this chapter.

An analytical solution to the first-order mass transfer equation was fit to the simulated breakthrough curves to estimate the four effective parameters: Pe, $\beta_{noncont}$, $\beta_{noneq}$, and Da. The values of Da and $\beta_{noneq}$, in particular, quantitatively indicates the importance of nonequilibrium mass transfer, while the sum of $\beta_{noneq}$ and $\beta_{noncont}$ indicates the magnitude of the immobile domain.

The distribution of arrival times of particles was converted to a discrete series of concentration values by summing all of the particles that come through the breakthrough point between two times into a single total value. This total mass is then divided by the flux and the total time elapsed over which the particles were summed in order to give a concentration at the midpoint of each time interval. Once we had the results in terms of concentration, we estimated the four parameters with the Eulerian analytical solution of *Goltz and Roberts* [1987] modified for our parameter groups:

$$\overline{C}(x',s') = \frac{M e^{x' / 2\frac{\lambda}{L}Pe}}{2\Omega(s')\sqrt{\frac{\lambda}{L}Pe(1+\beta_{tot})}} \exp\left\{ -\frac{x'\Omega(s')}{\sqrt{\frac{\lambda}{L}Pe(1+\beta_{tot})}} \right\} \qquad (6)$$

Where $\overline{C}(x, s)$ is solute concentration in the Laplace domain, and $\Omega(s)$ is defined by:

$$\Omega(s') = \sqrt{\frac{1+\beta_{tot}}{4\frac{\lambda}{L}Pe} + \frac{Da\beta_{noneq}s'}{s'+Da} + s'} \qquad (7)$$

s' is the normalized Laplace parameter, s, $s' = s\frac{L}{\overline{v}}$, and M is the initial solute mass. The concentration in time was then calculated by inverse Laplace transform of $\overline{C}(x,s')$ using the algorithm from *Hollenbeck* [1998; *ftp://ftp.mathworks.com/pub/contrib/v4/math/invlap.m*] by way of *de Hoog, et al.* [1982]. The theoretical breakthrough curve was fit to the simulation breakthrough curve by simple least-squares minimization.

We found that considering the entire breakthrough curve, rather than just temporal or spatial moments of the solute plume, provided more accurate parameter estimates. Estimating mass-transfer parameters from moments requires the calculation of higher order moments, which are subject to increasing errors as more weight is applied to extreme values [*Harvey and Gorelick*, 1995].

## 3.3 Results

### 3.3.1 Characteristics of the Flow Fields

**Effective Conductivity**

The effective conductivity of each field was calculated by averaging the specific discharge in the x-direction (the primary direction of flow) over any transect perpendicular to flow and dividing by the hydraulic gradient. The resulting effective conductivities, normalized by the geometric mean conductivity, are plotted in figure 3 as a function of the ln(K) variances of the fields. This figure compares the effective conductivities for each of the three fields (connected, disconnected, and multigaussian) to the geometric, arithmetic, and harmonic mean conductivities, which are the same for all three fields because the fields share the same histogram.

The effective conductivity for the multigaussian field agrees well with theory – for all variance values it remains close to the geometric mean, the theoretical value. The effective conductivities of connected and disconnected fields deviate significantly from the geometric mean. For the connected field, the effective conductivity exceeds the geometric mean, and for the disconnected field is below the geometric mean. These differences increase as the variance increases.

### Velocity Variability

The connected field shows by far the largest velocity variation (figure 4), and one that steadily increases with increasing conductivity variance. The multigaussian field matches the theoretical prediction quite well in the x direction and at low variance in the y direction, but does not match as well at high variance in the y direction. Higher-order approximations for velocity variance have shown some potential for deviation from the first order model in directions perpendicular to flow [e.g., *Deng and Cushman,* 1998]. These results suggest that solute spreading, and hence effective dispersivities, should increase in all three field types as the variance increases, and that the connected field may have higher dispersivities than the multigaussian field, which may be higher than the disconnected field.

### 3.3.2 Solute Transport – Mass Transfer Behavior

The simulated breakthrough curve and model fits in figure 5 demonstrate that incorporating the mass-transfer model can significantly improve the model fit to simulated solute transport. In the case of the connected conductivity field with a ln(K) variance of 9 and no diffusion, both models adequately fit the peak of the breakthrough curve. However, the macrodispersive model alone poorly fits the tail of the breakthrough curve (figure 5). This tail is frequently a problem in real-world situations, and thus its characterization is of primary importance. The tail is a significant percentage of the total mass, and breakthrough of this mass continues well after the macrodispersive model predicts insignificant concentrations, as is clear in the cumulative breakthrough curve.

Attempting to fit the breakthrough curve with $\beta_{noncont}$ set to zero (figure 6) demonstrates the importance of modeling a subdomain that does not affect solute over the time scale of the numerical experiment. Figure 6 shows that either the peak of the curve (the sharp ascent at the front of the curve) or the tail of the curve can be matched, but without the use of $\beta_{noncont}$, the complete curve cannot be reproduced. Thus, there appears to be a significant fraction of the domain through which very little solute passes over the time-scale of this particular simulation. Combining a nonequilibrium and noncontributing immobile domain, we can match the breakthrough curve quite well, as can be seen from figures 5 and 6.

### Transport through Connected, Multigaussian, and Disconnected Conductivity Fields

The breakthrough curves (figure 7) are substantially different for the three different fields, although they share the same basic statistics. Much of the differences among these breakthrough curves is explained by the difference in mean fluid velocity (effective conductivity), discussed in the previous section. However, there are also significant differences in spreading and tailing, as demonstrated in figure 8, where the breakthrough curves are plotted against normalized time. The figures show breakthrough curves for various values of normalized diffusion coefficient:

$$d' = \frac{dL}{\overline{v}\lambda^2} \tag{8}$$

where d is the diffusion coefficient of the solute in the porous media. This normalized diffusion coefficient represents the ratio of the rate of diffusion in and out of structures with characteristic length, $\lambda$, to the rate of advection through the field. If the value is greater than 1, then the mean time to diffuse in and out of statistical structures in the field is smaller than the mean time to advect across the field.

The breakthrough curve for the connected field (figure 8) shows tailing in the high variance cases, with the most significant tailing occurring with low and intermediate diffusion coefficients. The multigaussian field has very small tails in its breakthrough curves in the high variance case, which disappears for high diffusion coefficients. The disconnected field does not appear to have significant tailing. The difference between the curves for different conductivity fields diminishes for high values of the diffusion coefficient.

### 3.3.3 Breakthrough Curve Analysis – Parameter Estimates

The qualitative observations described above are quantified by estimating transport and mass transfer parameters from the simulated breakthrough curves. The four parameters estimated were: the Peclet number, Pe (the non-dimensionalized form of the macrodispersivity), the two capacity coefficients, $\beta_{noncont}$ and $\beta_{noneq}$, and the Damköhler number, Da (the non-dimensionalized form of the nonequilibrium mass transfer rate coefficient). A complete summary of the estimated parameters is shown in figure 9, which is a series of contour plots of the four parameters for the three different patterns for hydraulic conductivity (multigaussian, connected, and disconnected). The parameters shown are those estimated with the flux-proportional starting conditions. The x-axis of each plot indicates the normalized diffusion coefficient (d'). The y-axis of each plot indicates the ln(K) variance of the conductivity field. The contour plots show the estimated parameter for the particular field type as a function of these two variables.

Because the parameters are in non-dimensional groups, these simulations may be applicable over a large range of length and time scales. However, it is useful to check that the values plotted in figure 9 may represent practical situations. For example, if we consider transport over a length of 6m, for a groundwater velocity of $3.5*10^{-7}$ m/s (3 cm/day), an apparent diffusion coefficient of 0.35 $cm^2$/day ($4*10^{-10}$ $m^2$/s, approximately the diffusion coefficient in porous media for many dyes), and a representative length of heterogeneities of 9 cm, then the normalized diffusion coefficient, d' (eq 8), is approximately 1, which falls near the center of the x-axis of each plot.

**Dispersivity (Pe):** The normalized dispersivity results in figure 9 are consistent with the trends in velocity variances. For all three fields, the estimated dispersivity increases with variance in ln(K) and hence with velocity variance. Also, the estimated dispersivity in the connected field is greater than the multigaussian field, which in turn is greater than the disconnected field, again consistent with velocity variance.

The first-order approximation (chapter 2, eq. 3) for the dispersivity in a multigaussian field is simply the variance in ln(K) when normalized by the correlation length. Because we have already normalized our dispersivity estimates by the correlation length, the contours of our estimates should intersect the ln(K) axis at the value of the contour lines, if the first-order multigaussian result applies. For the connected field, this is clearly not the case. The dispersivity values are significantly larger than the multigaussian theory predicts. For the disconnected field, the estimated dispersivities are much lower at high ln(K) variance than predicted. For the multigaussian field, the results are much closer to the theory, but do not perfectly agree. This discrepancy may be caused by the inclusion of mass-transfer processes in our model, which will lead to lower estimates of dispersivity because some of the spreading is accounted for by the mass transfer parameters, or by the flux-proportional initial conditions.

The estimated dispersivity for the connected field is generally decreasing with an increasing diffusion coefficient, d'. This is similar to the results for dispersion in stratified media [*Matheron and deMarsily*, 1980], which also has continuous paths of relatively high velocity. An exception exists for small diffusion coefficients and large ln(K) variances, where the dispersivity, in fact, increases. The disconnected field shows increasing dispersivity with increasing ln(K) variance, but exhibits little dependence on diffusion coefficient. The multigaussain field shows evidence of dispersivities that increase with the diffusion coefficient and increase with increasing field conductivity variance.

**Noncontributing Capacity Coefficient ($\beta_{noncont}$):** The noncontributing capacity coefficient (second column of figure 9) indicates the proportion of the flow field from which solute is excluded. In conjunction with the nonequilibrium capacity coefficient, it also indicates how much faster the average advective flow of solute in the field is relative to the average fluid velocity in the field.

The values of $\beta_{noncont}$ are relatively large in the connected field at high variance. At a variance of 9 with no diffusion, the value of $\beta_{noncont}$ reaches 1.7, indicating that solute is not interacting with a large portion of the conductivity field. As the diffusion coefficient increases, the non-contributing capacity coefficient steadily decreases because diffusion mixes solute into a larger proportion of the domain. The multigaussian and disconnected fields show substantially smaller values of $\beta_{noncont}$.

**Nonequilibrium Capacity Coefficient ($\beta_{noneq}$):** The nonequilibrium capacity coefficient (third column of figure 8) describes the ratio of the pore volume subject to nonequilibrium, or rate-limited, mass transfer, to the pore volume of the mobile domain. In concert with a value of Da on the order of 1, a high value of $\beta_{noneq}$ indicates that significant nonequilibrium mass transfer occurs.

By far the largest amount of nonequilibrium mass transfer occurs in the connected field, with $\beta$ reaching a maximum value of 0.82 for a ln(K) variance of 9, and normalized diffusion coefficients greater than 0 but less than 1. The disconnected field shows $\beta_{noneq}$ values that are no greater than 0.1, indicating only minimal nonequilibrium mass transfer. The multigaussian field also shows relatively small $\beta_{noneq}$ values. The highest value of $\beta_{noneq}$ in the multigaussian field is 0.2, which occurs in the multigaussian field with variance of 9 and with normalized diffusion coefficients near 0.5. While much less significant than the values for the connected field, this value is high enough to cause the slight tailing noted earlier in the qualitative descriptions. In all three fields the value of $\beta_{noneq}$ increases with increasing ln(K) variance, consistent with the idea that as the variance of the fields increase, the proportion of conductivity values that are sufficiently low to be treated as immobile also increases.

Although the largest values of $\beta_{noneq}$ in the connected field are found when d' is greater than 0, but less than 1, significant values of $\beta_{noneq}$ are also observed when the normalized diffusion coefficient is 0, indicating advective-driven mass transfer. The relative importance of advective and diffusive driven mass transfer is discussed latter.

**Rate Coefficient (Da):** The mass transfer rate coefficient (nondimensionalized as Da in the last column in figure 9) indicates how quickly solute is moving in and out of effectively immobile zones if nonequilibrium mass transfer is occurring. Values on the order of 1 indicate that the timescale of mass transfer is comparable to the time to advect across the field. If Da is much higher than 1, then mass transfer is occurring so quickly that equilibrium mass transfer is present instead of nonequilibrium mass transfer. If Da is much lower than 1, then the solute does not have sufficient time to move into the immobile regions, and thus, during the timescale of the simulations, these regions remain inaccessible. Such processes would be accounted for by the estimated $\beta_{noncont}$. The value of Da is only meaningful when it is associated with a significant immobile volume as indicated by a value of $\beta_{noneq}$ significantly larger than 0. Thus, the mass transfer rate coefficients for the connected case are meaningful. For the multigaussian and disconnected fields, the value of Da is less important.

The estimated Da's for the connected field increase with increasing variance in ln(K). This indicates that the effective rate that solute is transferred between mobile and immobile regions also increases as the contrast between high and low conductivity regions increases (and the volume of the immobile region subject to nonequilibrium mass transfer increases). We also find that for high ln(K) variances, the rate coefficient is highest when there is no diffusion. These results are at odds with the notion that mass transfer is caused exclusively by diffusion. If mass transfer was caused by diffusion in and out of immobile regions of a size characterized by the correlation length, $\lambda$, then the estimated values of Da would increase linearly with increasing diffusion coefficients (d').

### 3.3.4 Advective Mass Transfer

Several results from the previous section indicate that mass transfer is controlled in some cases by advection through low conductivity regions rather than diffusion. First, the nonequilibrium capacity coefficients were estimated to be significantly large in simulations in which the diffusion coefficient was zero. Without diffusion, the only process driving mass-transfer in and out of immobile regions in these simulations is advection. Second, the rate coefficient did not increase in direct proportion to the diffusion coefficient, as would be expected if mass transfer were driven by diffusion.

To examine the effects of advection on mass-transfer for different diffusion coefficients, solute transport was simulated through the conductivity fields with the head gradient increased by a factor of two, doubling all velocities, while other conditions were held constant. The importance of advection is then ascertained by examining the estimated rate coefficients, $\alpha$, from the subsequent breakthrough curves. If nonequilibrium behavior is entirely advection-dependant, the estimate of $\alpha$ will also increase by a factor of two, as the rate of transfer in and out of immobile regions driven entirely by advection will scale identically with velocity. The assumptions for both fields, in both simulations, were that the mean conductivity was 8 cm/day, the hydraulic gradient was 0.01, and the total travel distance was 6m.

The results for the two connected fields with ln(K) variances of 6.25 and 9 (figure 10) demonstrate that there is an advective component to the nonequilibrium behavior in both of these fields. In the absence of diffusion, estimated rate coefficient values, $\alpha$, double when the velocity is doubled, indicating that mass transfer is driven only by advection. As the diffusion coefficient is increased, the estimates of $\alpha$ converge to the same value for both velocities, indicating that diffusion is the dominant process, overwhelming advection. Parameters are shown in dimensional form because increasing the velocity by a factor of two causes the normalized coefficients of the two cases to vary. To prevent confusion, the estimates are shown as their actual values.

We can gain some insight into conditions under which mass-transfer is dominated by diffusion or advection by considering the ratio of the estimated $\alpha$'s for the two different velocity conditions. A ratio that is less than 1.5 suggests diffusion is more important. By this criterion, in the connected field with variance of 6.25, advective mass transfer dominates up to a diffusion coefficient of 0.24 $cm^2$/day, which corresponds to a normalized diffusion coefficient in the base case of about 2. Though diffusion appears to be the more dominant mass transfer process above this threshold, the capacity coefficient is small ($\beta_{noneq} < 0.2$), so there is actually very little rate-limited mass transfer at these high diffusion coefficients. Thus, overall, advective mass transfer may be the dominant nonequilibrium process in the connected field with ln(K) variance of 6.25. For the connected field with a variance of 9, advective mass transfer dominates up until a diffusion coefficient of 0.21 $cm^2$/day, which corresponds to a normalized diffusion coefficient of approximately 0.8. Since the immobile domain is still significant ($\beta_{noneq} > 0.7$) at this diffusion coefficient, diffusive mass transfer plays an important role in this conductivity field.

We also found that increasing the velocity significantly increased the estimated dispersivity in the connected field, but did not significantly affect the estimates of $\beta_{noneq}$ and $\beta_{noncont}$ (maximum change of 12%). For large diffusion coefficients ($d' = 3$), the effective dispersivity increased by a factor of 3.2 for a doubling of the velocity. This increase approaches the increase of a factor of 4 predicted for transport in layered systems by *Gelhar, et al.* [1979], and *Matheron and de Marsily* [1980]. At lower diffusion coefficients, we did not find as large an increase in the estimated dispersion coefficient with velocity. We believe this is because of the initial conditions that place particles only in high velocity paths, which is analyzed below.

### 3.3.5 Initial Conditions

In the simulations described so far, the spacing of particles introduced along the injection line was proportional to fluid flux, the approach of *Desbarats [1990]*. This starting condition was modeled with the mass-transfer model by setting the initial immobile concentration to zero.

We now consider an alternative initial positioning, equidistant placement along the vertical line. For this placement, we change the initial conditions for the mass transfer model to equal concentrations of immobile and mobile solute, i.e., equilibrium. It should be noted that *Vanderborght, et al.*[1998], suggested that the flux proportional method is generally preferable since it does not bias late-time parameter estimates with early-time anomalies. They also suggested that this initial condition bias is removed from the transport relatively quickly (a few correlation lengths). However, they dealt with only multigaussian fields at relatively low ln(K) variance (approximately 2.5), so results in our fields may differ.

The greatest effects on the breakthrough curve are seen for a ln(K) variance of 9 for the connected field (figure 11). Little difference is seen at low variance between the different starting conditions, or at high variance for the multigaussian and disconnected fields, and the estimated parameters change by less than 15%. However, for the connected field with ln(K) variance of 9, the estimated dispersivity and $\beta_{noncont}$ are significantly different between the two initial particle placements. At a diffusion coefficient of zero, the estimated dispersivity increased by a factor of three for the equally spaced starting position. This may be due to the fact that in the connected field, the flow channels are contiguous throughout the entire domain. In the case where starting positions are proportional to velocity, most particles start out in fast moving streampaths, and in the absence of diffusion, stay in those paths. In the case with starting positions equidistant, the particles start out in and remain in a wider variety of velocities, so the effective dispersivity is larger. This explanation is supported by the fact that when a relatively small amount of diffusion is introduced (normalized diffusion coefficient, d', equal to 0.3), the difference in dispersivities drops to a factor of two, and decreases even further as more diffusion is added. Diffusion allows faster mixing across flow paths, thereby negating the effects of the starting positions. This explanation is also consistent with the result that the estimated fraction of the domain in which significant solute does not pass, $\beta_{noncont}$ is significantly smaller with the initial conditions of evenly spaced particles. The initial equal spacing places particles in all parts of the domain, so at least initially, no region of the domain is outside of the path of particles.

It is important to note that the different parameter estimates for both $\beta_{noncont}$ and the dispersivity do not indicate that different initial conditions drive fundamentally different behavior. Conductivity fields that are dominated by mass transfer in one case are also dominated by it in the other, while fields which are well-described by the advective-dispersive model in the flux-proportional initial condition will still be well-described by it when subjected to equilibrium initial conditions. However, the differences in parameters indicate that the initial conditions can have some influence on the evolution of the solute plume.

### 3.3.6 Evolution of Transport Parameters

Here we consider how estimated transport parameters may change for breakthrough curves at different downstream distances. All of the simulations discussed thus far have dealt with the same travel distance (67 correlation lengths). Now we consider estimated parameters 44 correlation lengths downstream of the injection distance with the particles started at the same location with the same initial starting positions (both proportional to velocity and with equidistant spacing). We ran the simulated flow and transport for all three field types at the highest variance (ln(K) variance of 9), where the largest differences, if any, should be found.

For the disconnected field, we found no significant change in any of the estimated parameters. For the multigaussian and connected fields, we found that the estimated dispersivities, rate coefficients, and nonequilibrium partition coefficients were all within close agreement (differences of less than 10 percent) with the same parameters estimated at the further downstream breakthrough curve. This held true for all values of the diffusion coefficient and for both initial conditions.

However, a larger noncontributing partition coefficient, $\beta_{noncont}$,was estimated from breakthrough curves recorded at 44 correlation lengths, as opposed to 67 correlation lengths, for both the connected and multigaussian fields when initial particle positions were proportional to velocity. The largest increase was estimated for no diffusion – in the multigaussian field, $\beta_{noncont}$ increased by 31 percent, and in the connected field it increased by 77 percent. The difference in estimated $\beta_{noncont}$ decreased as diffusion coefficient (d') increased, until at the largest value of diffusion coefficient (d' = 3), the estimates for both cases were nearly identical. When the starting positions of the particles were equally spaced, we found no substantial difference in the estimated values of $\beta_{noncont}$.

We attribute this increased estimate of $\beta_{noncont}$ to the same phenomena discussed in the previous section: the velocity-proportional initial conditions place the bulk of the particles in the fastest parts of the mobile domain, and the farther the particles travel, the more this initial bias is averaged out. Thus the average velocity of the particles in the mobile domain will be higher the closer the breakthrough point is to the starting point. This is consistent with the result that higher diffusion coefficients decrease the difference, since diffusion mixes particles out of fast paths more quickly. It is also consistent with the lack of significant differences in the estimated values of $\beta_{noncont}$ when the particles are started equally spaced, as there is no significant initial bias in the initial velocities with this starting condition. Also of note is that the multigaussian field does display some increase in $\beta_{noncont}$, but significantly less than the connected field. This is consistent with our earlier finding that there is a small, but real, $\beta_{noncont}$ in the high variance multigaussian field.

## 3.4 Discussion

Each of the three types of fields considered here has fundamentally different flow and transport behaviors.

In the connected field, the effective conductivity is greater than the geometric mean, velocity variations are much higher than the multigaussian equivalent, and solute transport is subject to significant mass transfer. The high conductivity zone forms a continuous network of paths through which fluid and solute move. Isolated low conductivity blobs are embedded in this network and form low velocity regions where solute is slowed or immobilized. Flow around these blobs creates a large variance in the velocity perpendicular to the mean direction of flow, and the sharp contrast between flow in the channels and the blobs creates a large variance in flow velocity in the mean direction of flow. For relatively low contrast ($\sigma_Y^2$ below approximately 4), mass transfer effects are not evident and transport can be accurately modeled by the advective-dispersion equation, although mean plume velocity is still greater than in the multigaussian case. If the contrast between the high conductivity paths and the low conductivity blobs is larger ($\sigma_Y^2$ above approximately 4 but below approximately 8), then advection through low permeability regions produces tailing. This advective process creates large-scale behavior similar to diffusive mass transfer, but the rates depend on head gradients rather than diffusion coefficients. If the contrast between the high and low conductivities becomes even larger, the size of the effectively immobile regions increases and the lowest conductivity regions become areas with no significant fluid flow. In this high variance case ($\sigma_Y^2$ above approximately 8), mass transfer is driven by both diffusion and advection.

At higher variances ($\sigma_Y^2$ above approximately 6), the effective dispersion coefficient for the connected field also shows characteristics similar to the effective dispersion coefficient in layered media [*Matheron and de Marsily,* 1980]. The effective dispersion coefficient decreases with an increasing diffusion coefficient, and the dispersion coefficient increases with velocity at a rate greater than linear, although not at the quadratic rate found for perfectly layered media. Thus, Matheron and de Marsily's theory, which considered flow that was not perfectly aligned with stratification, appears to also have some application to flow channels that are not straight.

Flow and transport in the connected field has many of the characteristics that are attributed to conductivity fields with layering, bimodal histograms, or large integral scales, described in the introduction. Yet, the connected field is isotropic, univariate lognormal, and has an integral scale much smaller than the domain length. The connected field has behaviors similar to a layered field because the high conductivity regions, although isotropic, form contiguous preferential channels for flow. It also may reproduce some of the behavior of nonstationary fields (i.e. field with integral scales larger than the domain size) because the high conductivity structures span the entire domain. Finally, the connected field can reproduce behaviors, such as nonequilibrium mass transfer, that are often attributed to fields with bimodal distributions, such as low conductivity blobs embedded in a matrix of uniformly higher conductivity. This is because the connected field also creates regions of low velocity embedded in channels of high velocity, even though the univariate distribution of ln(K) is Gaussian, and hence unimodal.

In the disconnected field, the effective conductivity is less than the geometric mean, the velocity variance is small, and mass transfer behavior does not occur. The contiguous structure of low conductivity areas in this field forces flow through low conductivity regions, so there are few, if any, isolated low velocity regions where mass transfer occurs. Flow lines are relatively straight, and the variance in fluid velocity is relatively low. Although the effective conductivity and dispersivity values are lower in this disconnected field than in the equivalent multigaussian field, the upscaled solute behavior in this type of field is similar to classical macrodispersion in a multigaussian field.

Flow and transport characteristics in the multigaussian field agree well with existing theory and are well modeled with the advective-dispersive equation. Thus, this field serves primarily as a control for numerical experiments in the connected and disconnected fields. Although the multigaussian field shows modest amounts of mass transfer at high variance, this behavior is not significant compared to the connected field. As with the disconnected case, there is no continuous high-velocity zone. Values close to the mean form a connected structure, spanning the domain, which isolates high conductivity blobs. A small volume of low conductivity blobs also exists and is of sufficient size and conductivity contrast to cause mass transfer, but this is a relatively minor part of the entire field.

The finding that mass transfer behaviors occur in fields with an effective conductivity greater than the geometric mean is consistent with the results of *Guswa and Freyberg* [2002]. They studied flow and transport through a homogeneous medium with elliptical inclusions (of varying shape, size, conductivity contrast, etc.) and also found that mass transfer occurs when the mean effective conductivity is greater than the geometric mean, but that transport is well described by the advective-dispersive model when the effective conductivity is at or below the geometric mean.

There are a variety of issues we did not consider. First, we have not studied the effective transverse dispersion of the solute movement through the various fields. Second, we neglected pore-scale, or mechanical, dispersion, and consider only small-scale mixing by diffusion. Third, we did not consider multiple rates of mass transfer for our effective model. A multirate mass transfer model could improve the breakthrough curve fits. However, our simple model provides qualitatively good fits and the parameter estimates give a clear quantitative characterization of the dominant transport processes in each scenario.

## 3.5 Conclusions

Our general conclusion is that very different flow and transport behaviors can occur in conductivity fields that all have nearly identical log-normal univariate conductivity distributions and nearly identical isotropic spatial covariance functions. Under many existing stochastic models, these fields would be identical in their predicted upscaled flow and solute transport behavior. A secondary conclusion is that significant rate-limited mass transfer may occur in smooth conductivity fields if the high values are well connected. This provides some theoretical basis for the application of mass transfer models to transport of conservative solutes in sedimentary aquifers with relatively high conductivity variance and connected high conductivities, such as the MADE site in Mississippi. Below, we list specific conclusions.

(1) Spatial patterns of hydraulic conductivity can be constructed with connected structures of either high or low conductivity, that have the same univariate probability density function and isotropic covariance function as a multigaussian field that does not have connected structures of extreme values. Although the integral scale of these connected fields is much smaller than the domain size, the connected structures of either low or high values span the entire domain.

(2) Matheron's conjecture that the effective conductivity in a two-dimensional conductivity field is the geometric mean does not apply to the connected conductivity fields considered here, although they are isotropic with log-normal univariate conductivity distributions. The effective conductivity is larger than the geometric mean for the field with connected high values of conductivity, and smaller for the field with connected low values.

(3) Velocity variability, and hence the effective dispersion coefficient, is substantially higher in the conductivity field with connected high values than in multigaussian field. The field with connected low values has substantially smaller effective dispersion coefficients than the multigaussian field.

(4) Rate-limited mass transfer, i.e., tailing, may be a significant process in conductivity fields with connected structures of high values. At variances in ln(K) above approximately 6, the majority of the field considered here is best modeled as immobile. A practical implication is that when the effective conductivity is significantly larger than predicted for multigaussian fields, mass transfer behavior may occur.

(5) Rate-limited mass transfer in hydraulic conductivity fields with connected high values can be driven by a complex interaction of advection and diffusion. For the cases considered here, mass transfer is primarily driven by advection below variances in ln(K) of approximately 8. For all values of conductivity variance, the largest total immobile domains are found when no diffusion is simulated. However, at higher variances, diffusion also plays a significant, and in some cases dominant, role. For higher values of the diffusion coefficient, the effective mass-transfer rate coefficients were reduced (contrary to the notion that the rate of mass

transfer is driven by the rate of diffusion), and the total proportion of the domain found to be effectively immobile was also reduced.

(6) Effective dispersion coefficients in the conductivity field with connected high values had characteristics similar to those of Matheron and de Marsily's [1980] dispersion coefficients for transport through layers, which also have continuous paths of high relative fluid velocity. The effective dispersion coefficient generally decreased with an increasing diffusion coefficient and increased with velocity at a rate greater than linear.

Most hydrogeologists will agree that large continuous flow channels have large effects on groundwater flow and solute transport. Here we demonstrate that significant effects of flow channeling may occur in statistically isotropic hydraulic conductivity fields that share the same basic statistics as stationary multigaussian fields with integral scales much less than the domain length. In particular, we find that rate-limited mass transfer may be a significant process during solute transport through a hydraulic conductivity field with a texture of connected high values, and that this mass transfer is driven by a complex interaction of both advection and diffusion. These results suggests that information on the connectedness of geologic media may be necessary not only to choose parameters for flow and transport models, but also to choose the form of the transport model. In conductivity fields with nearly identical conventional statistics, solute spreading may be well modeled by Fickian dispersion, or a mass transfer model may be required to adequately predict tailing, and the mass-transfer rate coefficient may depend on the hydraulic gradient, or on the apparent diffusion coefficient. Although characterizing patterns of connectedness in the field is an extremely difficult problem, these results suggest that representing spatial heterogeneity as multigaussian may not be a conservative assumption.

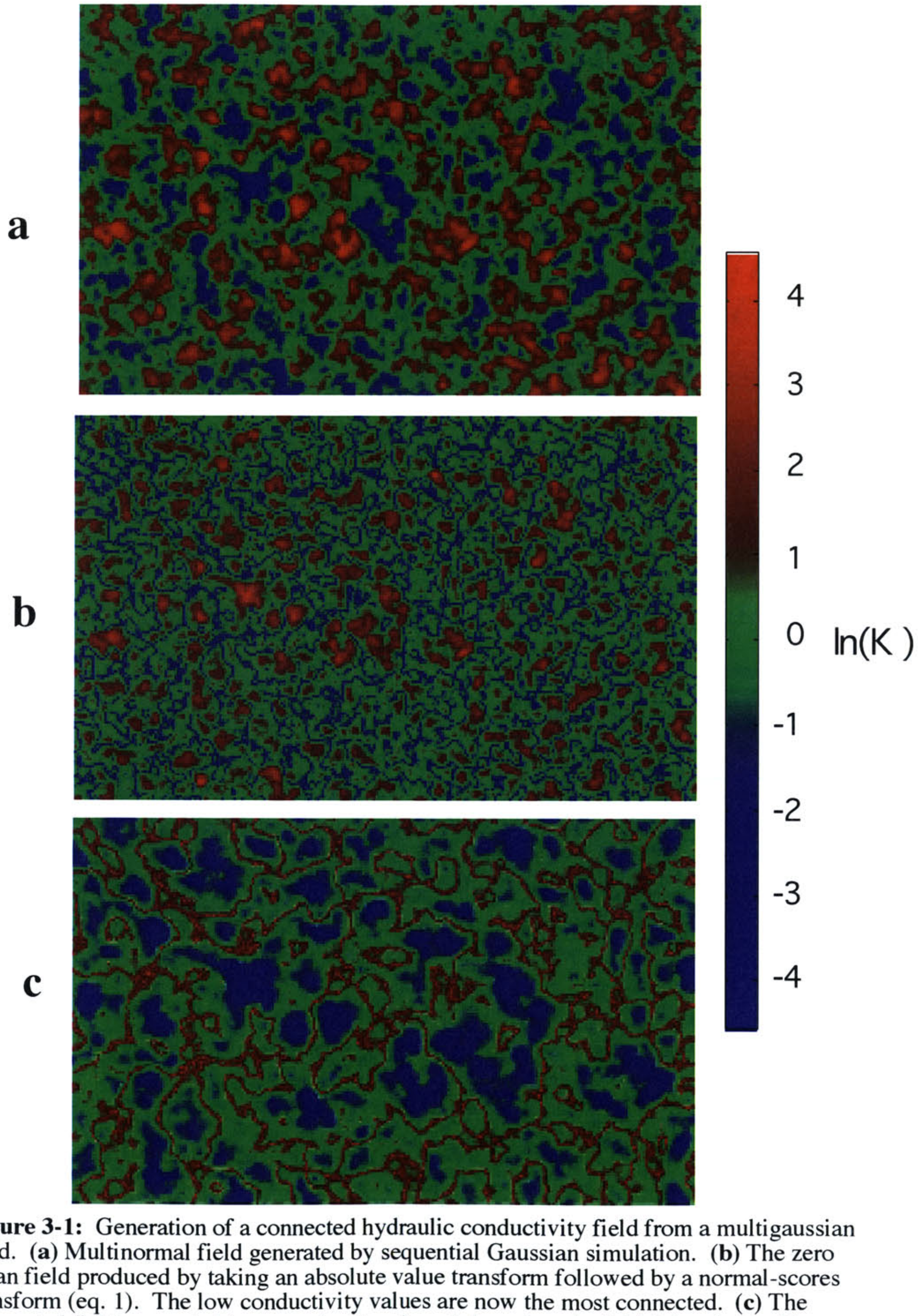

**Figure 3-1:** Generation of a connected hydraulic conductivity field from a multigaussian field. **(a)** Multinormal field generated by sequential Gaussian simulation. **(b)** The zero mean field produced by taking an absolute value transform followed by a normal-scores transform (eq. 1). The low conductivity values are now the most connected. **(c)** The connected field generated by reversing the sign of the values in field (b) and stretching the coordinate axis so that the field has the same correlation length as field (a).

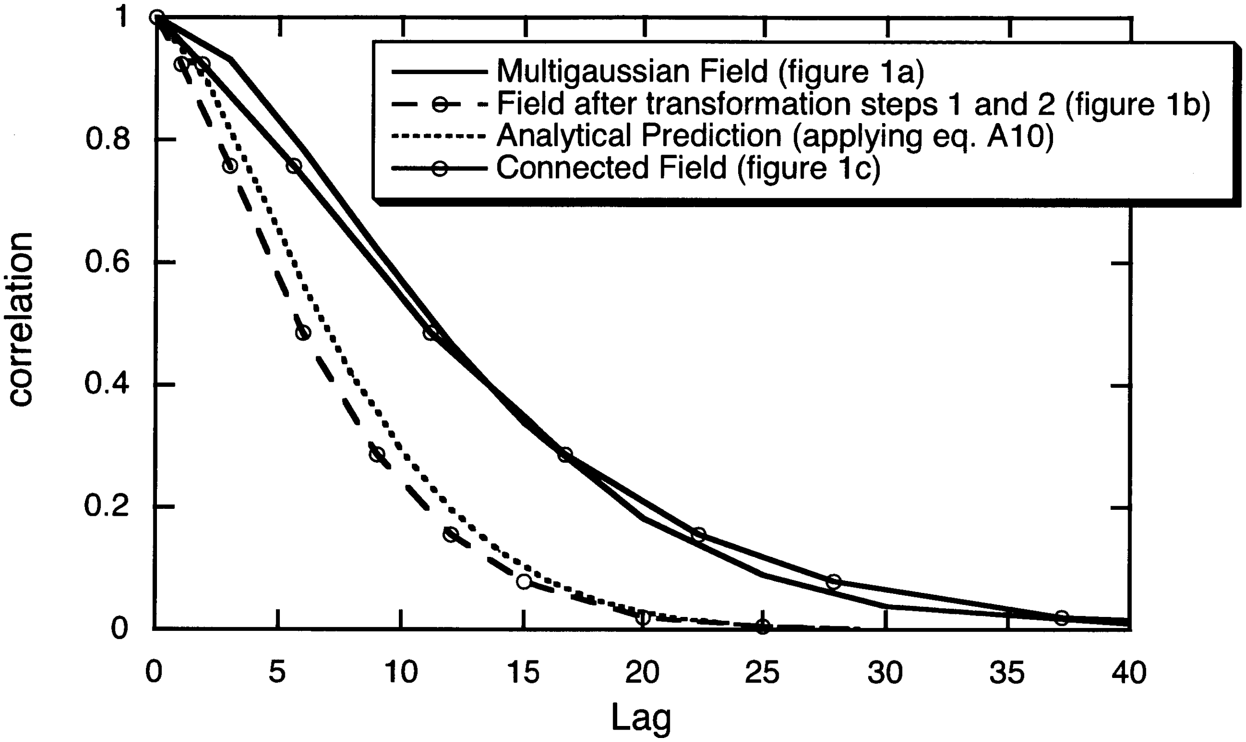

**Figure 3-2:** Comparison of spatial correlation functions for the multigaussian field (figure 1a) and the connected field (figure 1c) showing that they are nearly identical. Also shown are the theoretical correlation function of the absolute value transform of the multigaussian field (application of equation A10) and the calculated covariance of field (figure 1b), indicating that these are similar.

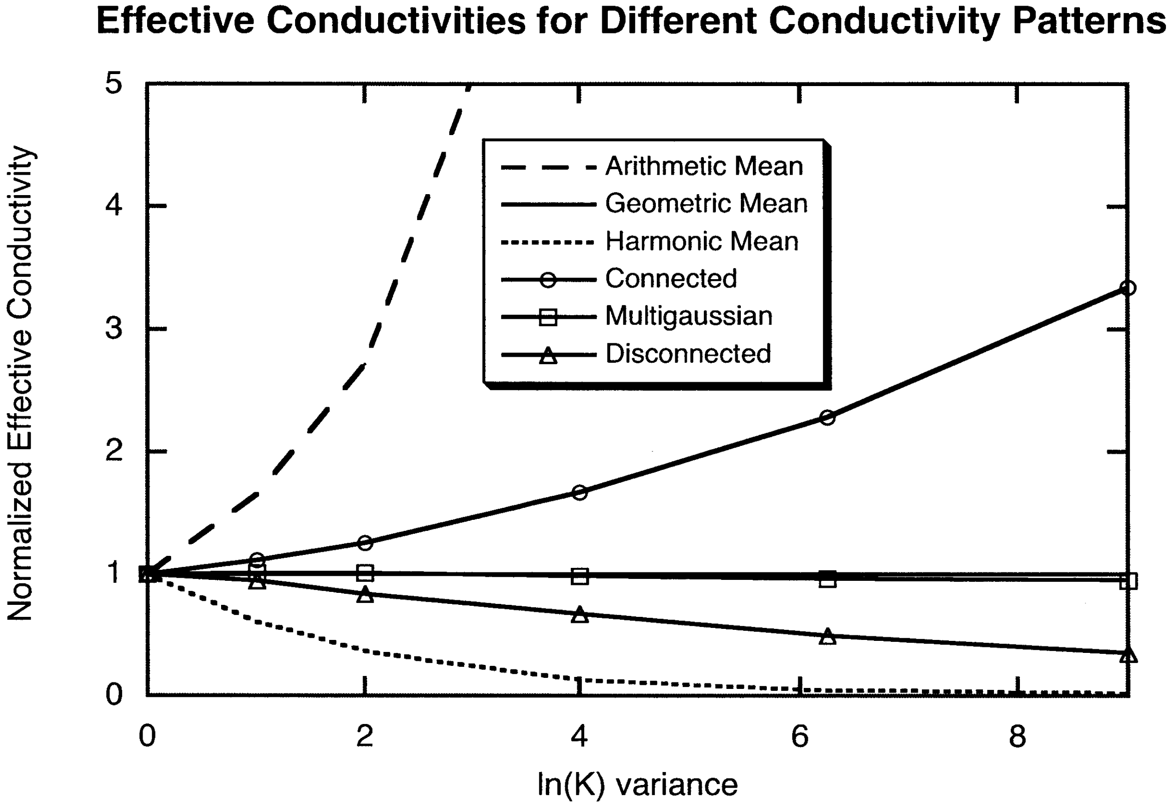

**Figure 3-3:** The effective conductivity for the three different conductivity fields: multigaussian, connected, and disconnected. These are shown as compared to the arithmetic, geometric, and harmonic means of the conductivity values. The values are all normalized by the geometric mean of the conductivity values.

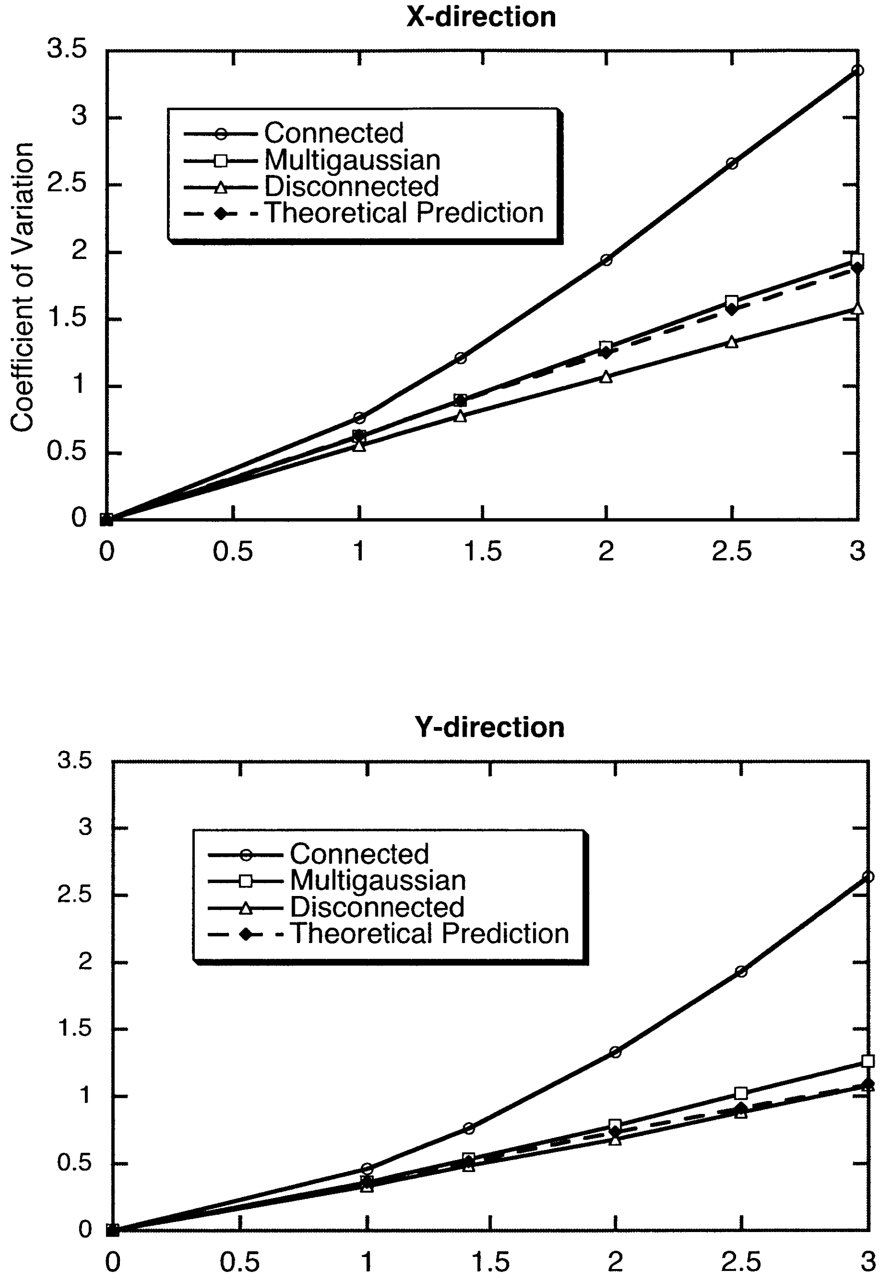

**Figure 3-4:** Coefficient of variation in velocity for the three different spatial patterns of conductivity as a function of the spatial variance of ln(K). Also shown is the theoretical prediction of the coefficients of variation. The left figure shows the variation in the direction of flow (x-direction) and the right-hand figure shows the variation perpendicular to the direction of flow (y-direction).

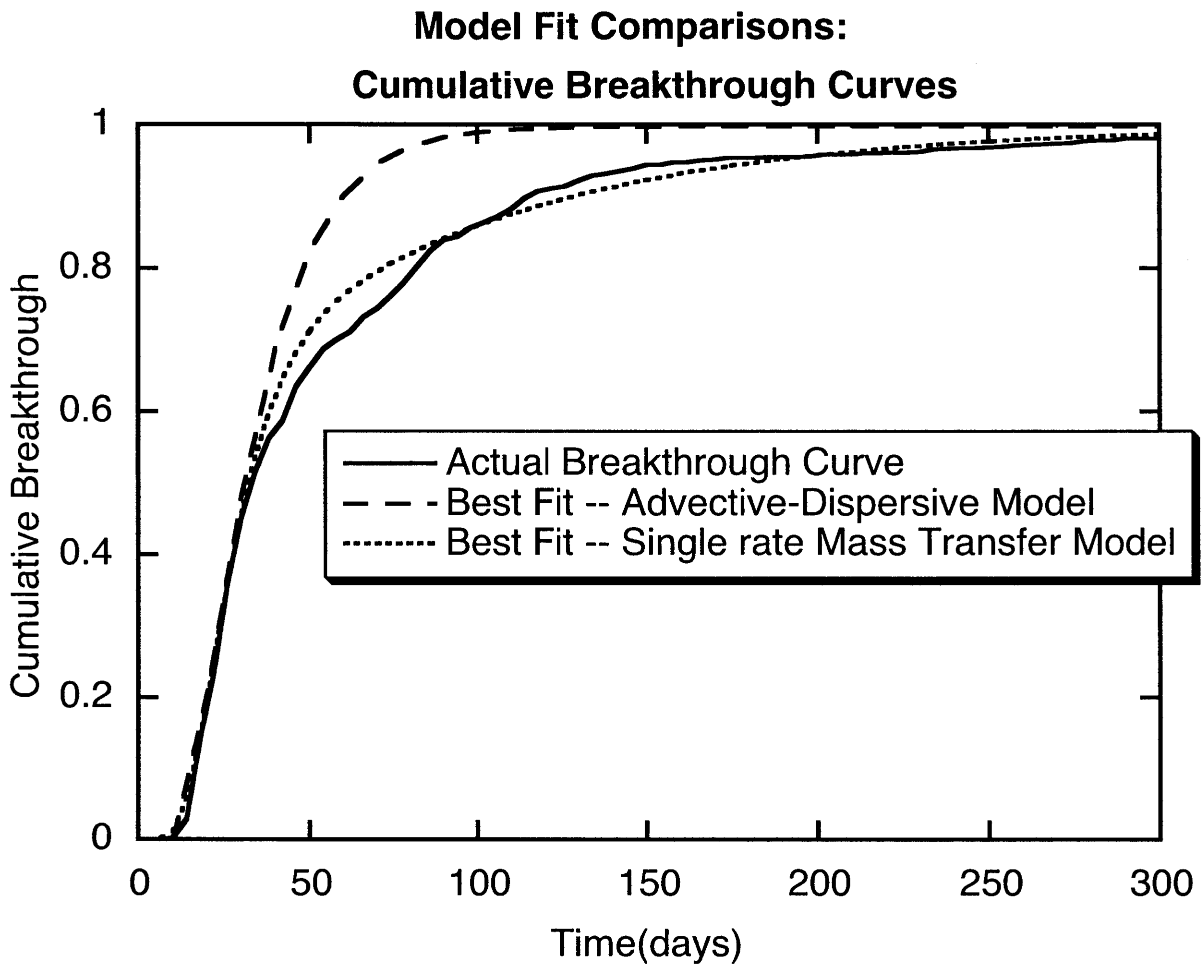

**Figure 3-5**: Comparison of breakthrough curve fits using the advective-dispersive model and the single-rate mass transfer model. The breakthrough curve was simulated in the connected conductivity field with a variance of 9 and no diffusion. The breakthrough curves are shown in the form of cumulative mass fraction breakthrough. The mass transfer model provides a better fit, especially in the tail.

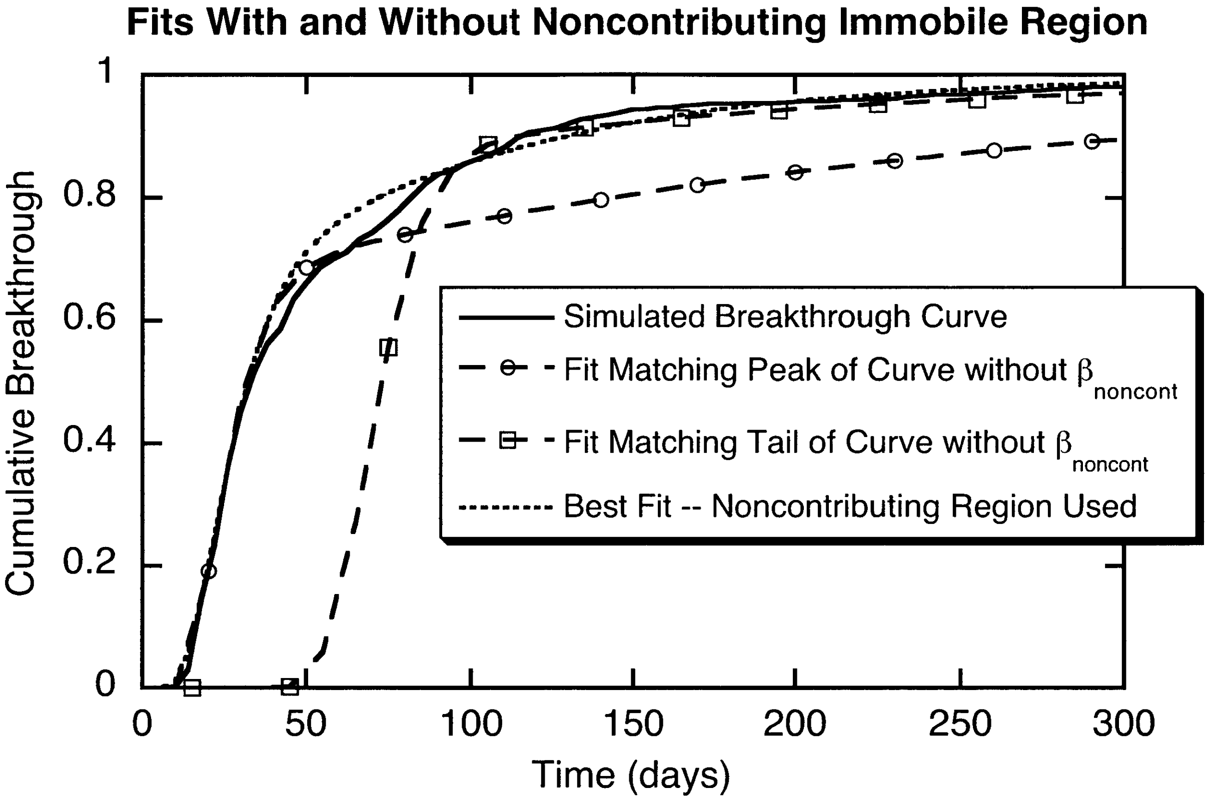

**Figure 3-6**: A simulated breakthrough curve, the best fit using the complete model equation (equation 4), and two fits made without considering a noncontributing immobile domain – one fits the peak of the breakthrough curve, one matches the tail. Neither do both, whereas the complete model better fits the curve at all times.

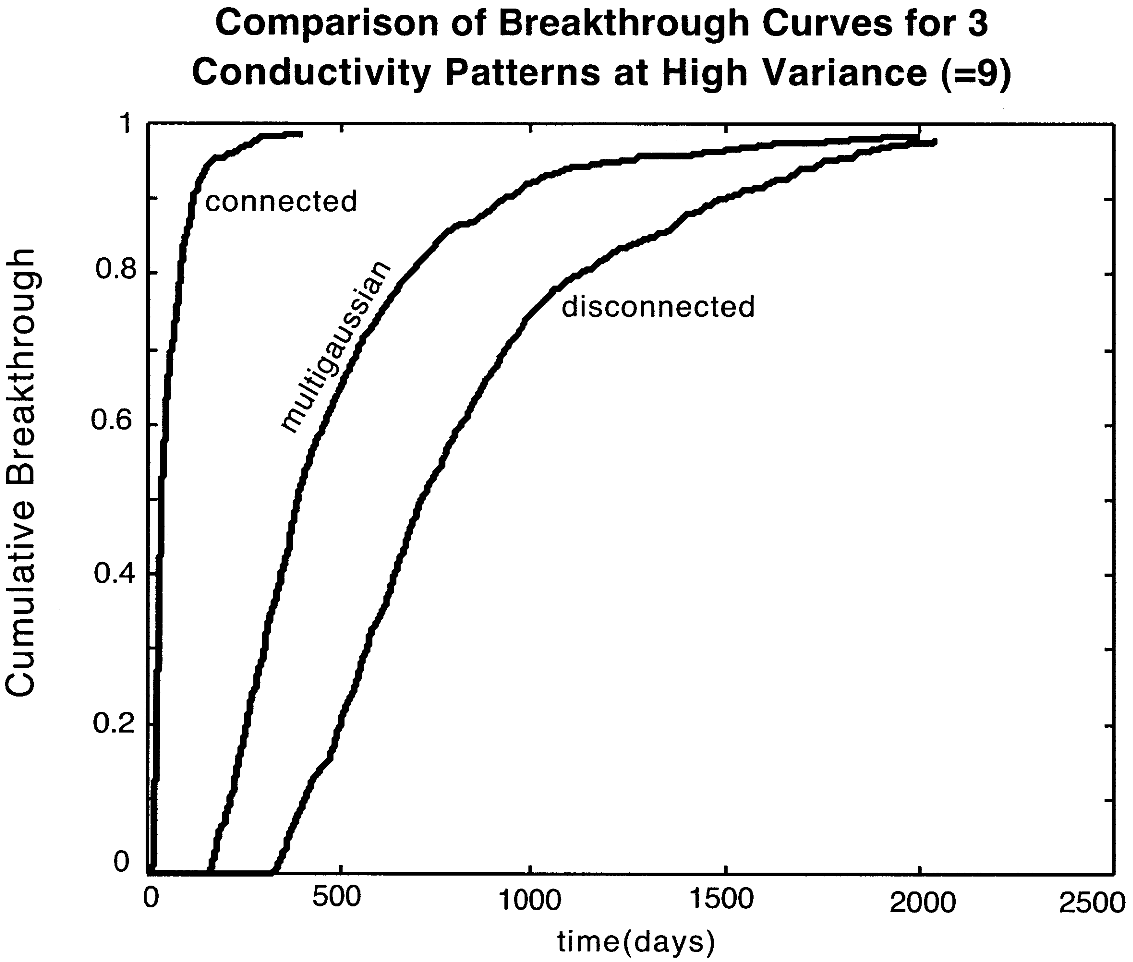

**Figure 3-7**: Breakthrough curves for the three different patterns of hydraulic conductivity with variance of 9 and no diffusion present. Demonstrates different mean arrival times

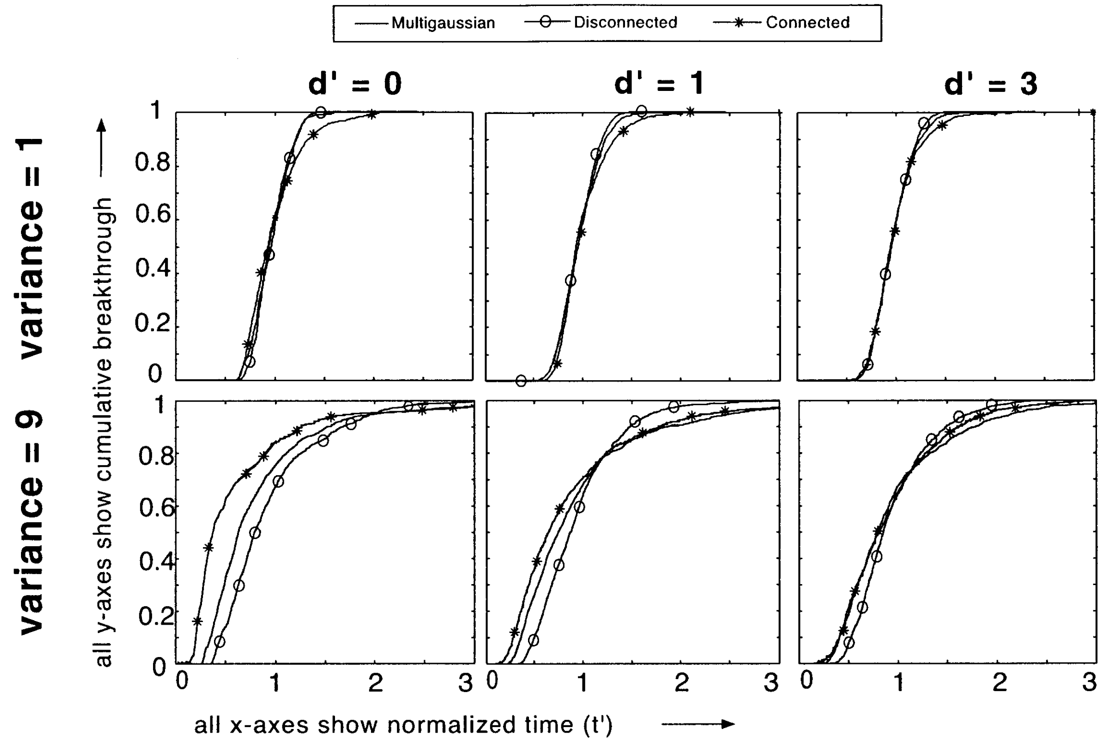

**Figure 3-8:** Cumulative breakthrough curves for the three different patterns of hydraulic conductivity after normalizing time by mean fluid travel time. Breakthrough curves are plotted for combinations of differing normalized diffusion coefficient (columns) and $\sigma^2_Y$(rows) for each of the three patterns of hydraulic conductivity.

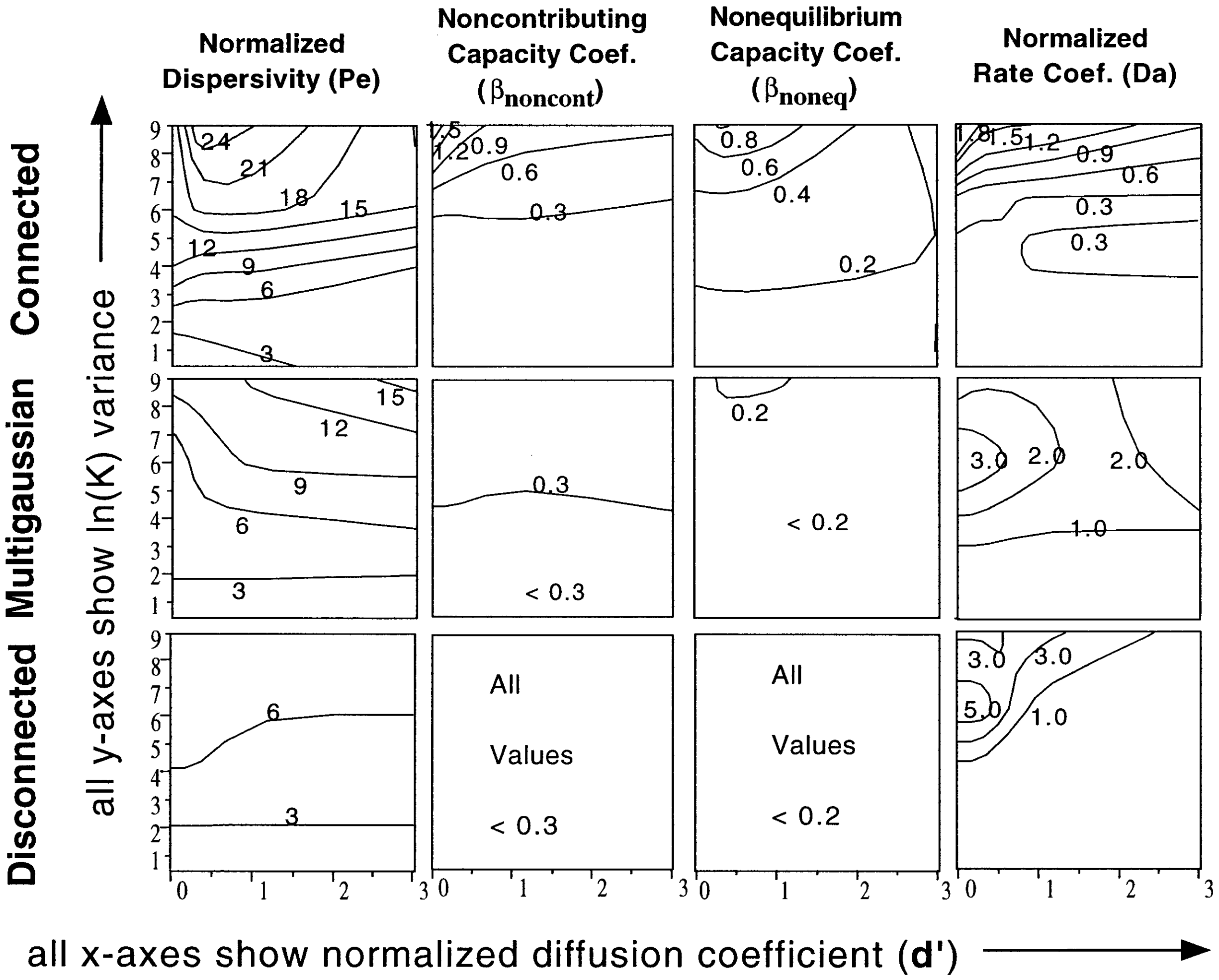

**Figure 3-9:** Estimated transport parameter values for each of the three different patterns of hydraulic conductivity. Each plot shows contours of an estimated parameter as a function of the field variance $\sigma^2_Y$ (y-axis) and the normalized diffusion coefficient d'(x-axis).

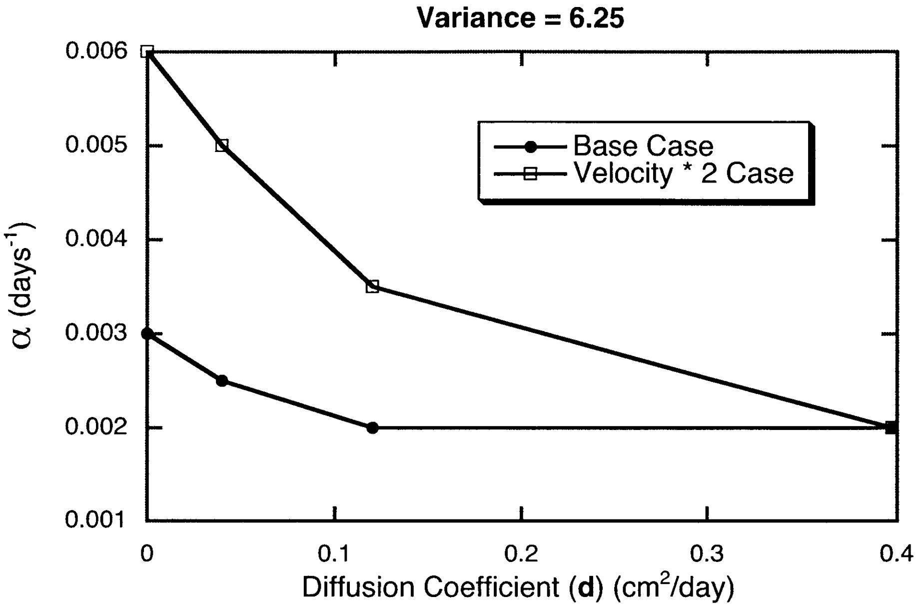

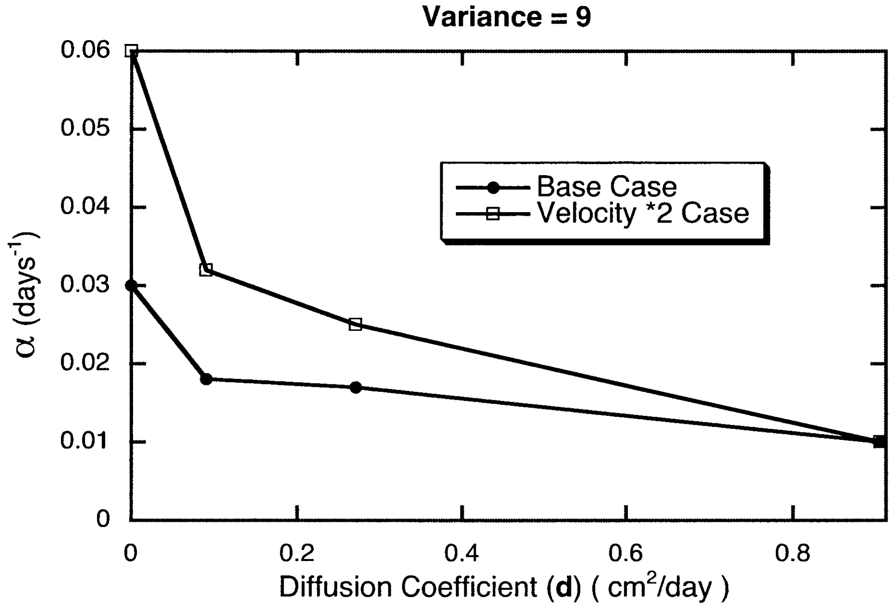

**Figure 3-10**: Estimated rate coefficients (α) as a function of the diffusion coefficient for the base conditions compared with estimated rate coefficients where the velocity (hydraulic gradient) is doubled. For zero diffusion the estimated rate coefficient doubled with a doubling of the velocity, indicating advective mass transfer.

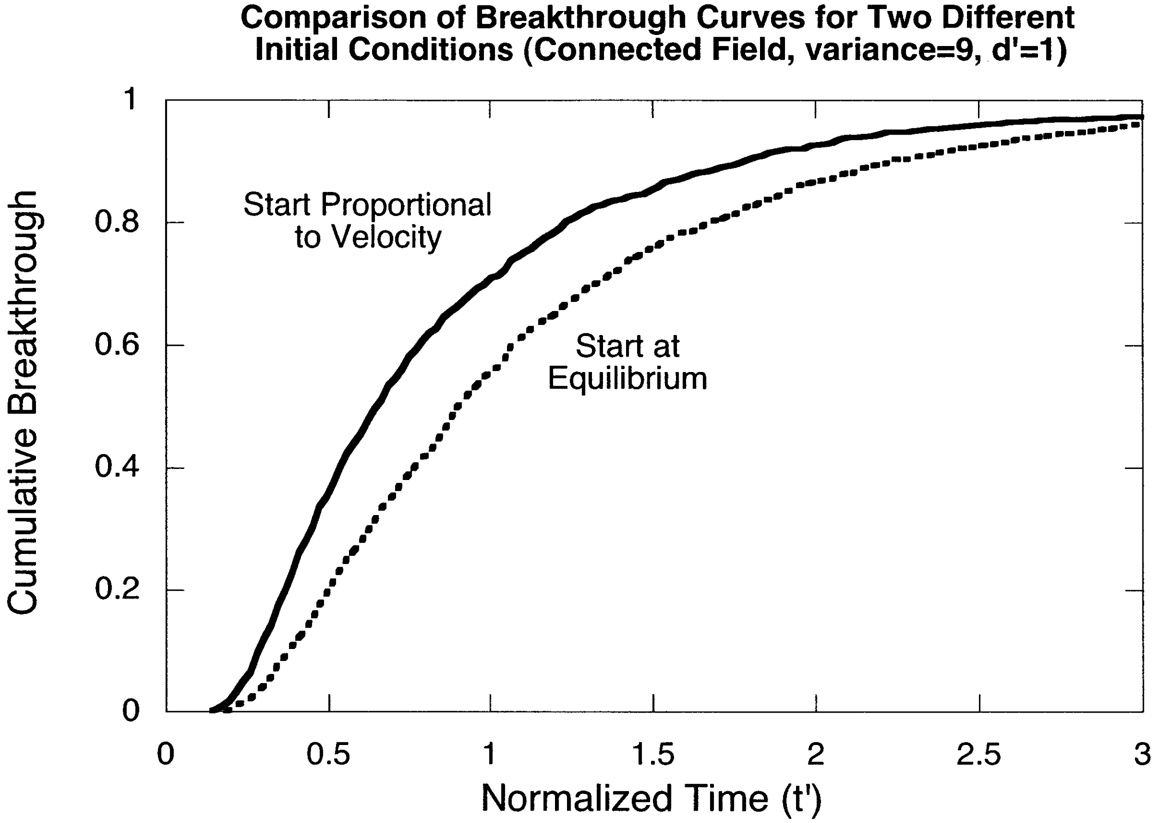

**Figure 3-11**: Normalized breakthrough curves for the connected field with $\sigma_Y^2=9$ and a normalized diffusion coefficient (d') equal to 1, with initial particle positions evenly spaced and proportional to velocity.

# Chapter 4

# Experimental Visualization of Solute Transport and Mass Transfer

## 4.1 Introduction

The work in the previous chapter demonstrates that connectedness can play a large role in solute transport, and that, particularly in fields with large differences between the upper and lower conductivities, could drive behavior that is fundamentally described by a mass transfer model instead of a macrodispersive model. In addition, the work in the previous chapter pointed to two possible processes driving mass transfer – advection and diffusion.

The results of the previous chapter, however, are completely theoretical. It is certainly legitimate to question whether a computer can successfully simulate reality, and more to the point, whether the conclusions we draw in the previous chapter are actually physically plausible. Is the existence of advective and diffusive processes driving mass transfer something we can actually demonstrate in a real porous medium? Can we actually observe a difference between advection-dominated mass transfer and diffusion-dominated mass transfer? Do observable differences in mass transfer at the small-scale actually amount to something relevant at a larger scale?

In this chapter, we attempt to answer these questions by means of a series of experiments conducted at the Flow Visualization Laboratory of the Sandia National Laboratories. We constructed a porous medium of glass beads, consisting of a high conductivity matrix surrounding low conductivity cylindrical emplacements, and used high-resolution photography to image solute flow through it. The structure of the field (high conductivity matrix surrounding lower conductivity structures) provides us with a connected field, which our previous work suggests is an important component of mass transfer. At the same time as we image solute in the porous medium, we measured outflow concentration of the solute, allowing us to examine both small-scale variability and its upscaled effects. Although this is an artificial aquifer, it is a porous medium that consists of reasonable structural characteristics. The experiments performed on this porous medium provide concrete illustration of our results in chapter 3, and form the basis of our work in chapter 5. Our ability to control the conductivity structure and visualize the solute plume in fine detail marks a departure from field work, where even highly detailed field sites require a great deal of extrapolation from limited data points. Our ability to control the conditions of the experiment also allowed us to perform experiments under a relatively large range of scenarios, such as modifying head gradients and the conductivity contrasts. The design also allows us to check upscaled results for some experiments against known analytical solutions, and we find that in those cases, our results are fit very well by analytical models.

## 4.2 Methods

Our experiments involved a lengthy set of procedures that we have organized into four categories. First is the construction of the tanks used for the experiments, which involved several specialized procedures. The second section details the other equipment used, including the spectrophotometer, pumps, camera, and light box. The third describes the experimental procedure. The last section describes how the data was processed to create images and breakthrough curves.

### 4.2.1 Tank Construction

The design and construction of the tank is a complex procedure, with several novel components developed specifically for this experiment.

Our first goal was to design a system that could hold glass beads of significantly different sizes. To create the conductivity contrasts we desired using nearly uniform sized spherical grains required significant size differences, problematic because small beads easily move through a matrix of significantly larger beads. Table 1 lists the sizes used for the three tanks and the conductivity ratio (conductivity of the larger beads divided by the conductivity of the small beads) created (using the Carmen-Kozeny-Bear equation [*Bear,* 1972] and incorporating edge effects [*Somerton and Wood,* 1988]). In order to keep the two bead packs separated while still allowing fluid interaction between the two regions, we constructed what we refer to as "emplacements."

Emplacements act as a thin separating wall between the two regions of different beads. Construction began by sintering together three stainless-steel meshes – a fine mesh (holes 30μm square) between two courser meshes (0.3mm square holes). The fine mesh restricts the movement of small beads while the coarser meshes provide structural support. The emplacements for advective-dipsersive case, in which the small beads were 0.9mm diameter, did not include the fine mesh.

The sintered-mesh screen was wrapped and welded into a circular shape (i.e., the screen looked like a circular pipe) with a 1 inch (2.54cm) diameter, and was then cut into 5.5mm thick slices. To ensure that all emplacements were of identical height, they were softened with moderate heat and placed together in a long vice-like device, which was closed to the desired thickness. The heated metal deformed at the edges and then cooled with a consistent thickness, altering the screen structure only along the edges and leaving all emplacements approximately the same thickness. The end result is an object that looks like a thin slice of porous pipe. The screen itself was approximately 0.5mm thick, encompassing less than 4 percent of the total volume of each emplacement. We completed construction by gluing an o-ring (25mm diameter, 1mm cord diameter) to the top of each screen slice, giving the emplacement a flexible but solid contact with the top of the flow area in the tank. The superglue gel we used was chosen for it's chemical properties and its viscosity. The glue did not significantly sorb with FD&C Blue #1 dyed water, and had a high viscosity, preventing glue from wicking into the steel mesh of the emplacements. Low-viscosity glues had a much greater degree of capillary-induced suction, leading to blocking of significant numbers of mesh pores.

We desired a random placing of the emplacement cylinders to avoid effects driven solely by configuration, without emplacements placed too close to each other or the tank's edges. We used a computer create a random pattern of 53 emplacements while honoring proximity constraints – emplacements may not be closer to each other than 6mm and not closer to the edges of the tank than 4mm. Using this pattern as a template, we glued emplacements onto a sheet of 0.02 inch (0.5mm) clear plastic.

A second problem caused by using beads of significantly different sizes is that light transmission through the bead pack is approximately proportional to bead size. To equalize intensities we attached a neutral density filter (a plastic sheet that reduced light transmission at all wavelengths) to the back of the plastic sheet containing the emplacements. The filter strength for each tank is noted in Table 1. We then cut circular holes in the filter at the emplacement locations, so that the filter blocked light entering the large bead areas without reducing transmission through small bead areas. The holes were cut to 0.75inch diameter, instead of 1 inch, to compensate for any holes being cut slightly off-center, and to ensure that refraction did not cause any additional light to enter the large bead areas. Tests showed that although the filter was covering parts of the small bead areas, light intensity was reduced no more than 50%, due to numerous of refractions and reflections in the small bead pack. It should be noted that in the diffusive mass transfer tank, holes were cut at 0.938inch diameter, causing minor problems (discussed in section 4). Even reduced light intensity around emplacement edges was sufficient for detailed concentration measurements.

To assemble the tank, we first packed the emplacements with small beads, then built the rest of the tank around the plastic base and its packed emplacements. Each tank consisted of several quasi-2D pieces stacked together and held along the sides by a clamping mechanism, with the top and bottom attached to specially designed flow manifolds.

We placed the filter and plastic base on top of a piece of 40cm long by 25.4cm wide by 1.9cm thick glass (the plastic base and filter have identical length and width as the glass). We then placed anodized aluminum side rails (40cm long, 2.7cm wide, and 0.635cm thick, save at each end, where width increases to accommodate manifold screws, see figure 1c for illustration) along the two sides of the emplacement-filled area. We then placed another piece of glass on top, making sure the entire "sandwich" is aligned, i.e., all edges in the sandwich and the ends of the side rails should line up. This sandwich, when finished, is illustrated (in side view) in figure 1a. The rails and glass plates form the no-flow boundaries perpendicular to flow in the experiment.

The sandwich was held together by two steel bars located on top of the glass, running lengthwise directly above the side rails. A cross-section of the bar is L-shaped, with the upright portion along the side closer to the middle of the glass (see figure 1b). The bar is designed to even out the pressure applied by two large steel screw plates (see figure 1b for cross-sectional appearance). The screws were tightened down to a torque of 10 joules on the pressure bars – the pressure bars applied evened downward pressure on the top glass plate and the screw plate bottoms applied upward pressure on the bottom glass plate. This holds the sandwich together with sufficient force to create a watertight seal around the flow area.

The next step in constructing the tank is to attach the manifolds. The two manifolds are specially milled Lexan blocks designed for either inflow or outflow, and thus go in specific locations (inflow at the bottom, outflow at the top – see figure 1c).

The bottom (inflow) manifold has three entrance points on its front side – eighth inch valve fittings that are attached to the inflow tubes. The entrance points connect through drilled channels to an approximately 15ml reservoir (see figure 2a). This reservoir creates an approximate constant concentration boundary during the experiment by creating a significant volume of a particular concentration along the inflow boundary. A fine mesh screen was placed at the top of the reservoir to even out flow, with a coarse mesh screen on top of it to provide structural support.

The top (outflow) manifold was designed to minimize outflow mixing and to prevent any stagnation zones from forming near the outflow. A series of grooves along its width channeled flow into low-volume funnels that connect to the three outflow points (see figure 2b) located at the top of the manifold. The outflow points are designed to each drain an identical cross-section of the tank. The grooves extend along almost the entire width of the flow area. The existence of flow channels all along the cross-section minimized stagnation zones, and the entire outflow manifold was designed to have a minimal volume to ensure short outflow residence time. Outflow from the manifold was channeled into three narrow (0.63inch inner diameter) outflow tubes of equal length that joined together into a single tube of the same diameter. This ensures that all outflow from the tank has an equal travel time to the photometer.

The manifolds were attached to the tank using silicone caulk and rubber sheeting cut into gaskets. The gaskets, attached to the manifolds and tank with silicone caulk, give the tank more reliable sealing than simply gluing the manifolds onto the tank, and also ease manifold removal. Two gaskets were used at each end of the tank – one attached to the manifold, the other to the tank, with the inner hole in each gasket approximating the boundaries of the flow area in the tank. The manifolds were attached onto the ends of the tank using screws that thread into the side rails (see figure 1c and figure 2). With the bottom manifold attached, we filled the tank with the large beads that form the porous medium outside of the emplacements. We slowly poured large beads into the tank, shaking, tapping, and using a pipe cleaner as a makeshift ramrod to maximize packing. Water was flushed and drained from the tank as a final impetus of consolidation. Once the packing was satisfactory, the top manifold was put on, and the tank was complete.

In order to allow for repeat experiments, we constructed three tanks, one for each transport scenario, using the same procedure (with a different bead size inside emplacements).

### 4.2.2 Other Equipment

Water was pumped into the tank using a computer-controlled piston pump, which gives accurate and consistent flowrates down to 0.001 ml/min. During the experiments, we used two pumps, each flowing at half of the desired flowrate. This allowed one pump to remain running while the other was refilled, preventing flow from ever being completely turned off. Refilling both pumps took about five minutes, a short time relative to experiment length.

Outflow dye concentration was measured with a Varian ™ spectrophotometer. The device is computer-controlled and programmable. The photometer was set to target two particular wavelengths, the 630nm (primary) peak of FD&C Blue#1 and the 409nm (secondary) peak. These peaks were studied extensively using full-range wavelength scans with a set of standard concentrations spanning the expected concentration range of the solute. The 630nm peak was effective at measuring concentrations from 0.01mg/l to approximately 20mg/l. The 409nm peak was effective from 0.1mg/l to above our maximum concentration of 30mg/l.

Tank outflow was measured by the photometer in two ways. In the advective-dispersive experiments (for reasons explained in the results section), we collected outflow in small sample bottles, then poured the sample into a cuvette for photometer scanning. For the two mass transfer experiments, we hooked the outflow of the tank into an 80μl flow-through cell placed in the spectrophotometer, minimizing the lag time between the outflow and the time it is measured, allowing extremely high measurement frequency, and reducing any mixing or contamination that could potentially occur in manual outflow samples. The use of narrow tubing and the small volume of the outflow manifold serves to keep the outflow lag time to less than three minutes for our smallest flow rates, a negligible amount compared to experimental length.

A timed series of chamber images was captured with a computer-controlled 12-bit liquid-cooled CCD camera. A combination of filters was used on the camera lens to filter out wavelengths save those near the peak absorbance (630nm). Pixel intensities were recorded and converted to relative light absorbance using the computer program IPLab™. Each pixel resolved and area of the tank approximately 400μm square.

The chamber was mounted in front of a diffuse light source composed of a bank of high-frequency (60 MHz), high-output fluorescent lights controlled through feedback circuitry and fan cooling to maintain a constant temperature. We also placed a photographic step tablet (a series of progressively darkening gray filters) next to the tank along the light box. This stepped density wedge, which was imaged along with the tank, calibrated shifts in light box intensity and acted as a fixed point in space for calculating camera field drift (see the post-processing section).

The entire setup, diagramed from the perspective of the camera, is shown in Figure 3. The light box is directly behind the tank. The photometer and pumps are represented as boxes in the diagram, and not drawn to scale. We also connected a valve system to the bottom manifold – this is necessary for the reservoir flushing, as described in the following section.

### 4.2.3 Experimental Procedure

Once the tanks were completed we ran the following procedure for each experiment.
Step 1: Pump the tank dry. We pulled air through a desiccating chamber and then through the tank using a vacuum pump until the tank was dry (usually about 24 hours).
Step 2: Clean water fill. We saturated the tank with $CO_2$ and slowly pumped de-aired water into the tank. The use of $CO_2$ with de-aired water produced rapid tank saturation, with small bubbles dissolving within a few hours. We took pictures of the saturated tank with the camera to determine ideal exposure times, using the image with the desired exposure time as the baseline "clean" image (see post-processing section). We also measured the porosity of the tank by calculating the total amount of water required to fill (subtracting for the manifold and tubing volume). We then drained the tank, which emptied most of the water from the large bead areas while leaving the small bead areas still saturated. In this way we calculated the porosity of both bead packs. We calculated porosities to be between 0.4 to 0.45 for all tanks and in both the large and small bead areas.
Step 3: Drain and dry the tank. We drained the water and dried the tank again.

Step 4: Fill with dye. We saturated the tank with $CO_2$ and pumped de-aired FD&C Blue#1 with a concentration of 30mg/l instead of clean water. Once saturated, the tank sat until dye concentration was homogeneous, which we checked by taking hourly pictures.

Step 5: Run standard calibration curve. We ran a set of standards composed of 10 concentrations through the spectrophotometer flow cell before beginning the experiment.

Step 6: Flush manifold. We flushed the lower manifold's reservoir clean of dye using de-aired water. All outflow from the tank at the top manifold was clamped off and the valve system attached to the bottom manifold (see figure 3) was configured to force flow through the bottom manifold reservoir and out of the tank. Flushing took approximately 5 minutes, and left the inflow tubing and manifold reservoir clean of dye. We then shut off outflow from the valve system and reopened the outflow ports at the top of the tank.

Step 7: Begin experiment. We activated the pumps, the camera, and the spectrophotometer at their desired pumping/acquisition rates. Start times were effectively simultaneous.

Step 8: Adjust equipment and sample. We took hand samples if necessary and adjusted time intervals for measurement devices and refilled pumps as needed.

Step 9: Another standard curve. A final standard curve ensured that spectrophotometer readings had not drifted significantly.

We repeated these steps for all experiments discussed in this paper save that steps 1 and 2 are only necessary once per tank, provided that neither the tank nor the camera are moved between experiments. Steps 5 and 9 were not necessary if all concentration measurements were done by hand sample.

### 4.2.4 Post-Processing

The post-processing of the data was designed to use light absorbance as a proxy for concentration in both the outflow measurements and tank images.

Although we ran standard concentration curves both before and after each experiment, we never found significant drift in the photometer. All standard curves were fit using least-squares linear regression and this line was used to transform photometer absorbance measurements into concentrations. All standards had very strong correlation, with r-squared values in excess of 0.999. We performed calibration for both the 630nm absorbance peak and the 409nm peak.

Outflow concentrations were calculated from photometer absorption measurements at both wavelengths. We then picked a specific concentration value (usually near 10mg/l) around which both sets of measurements were in close agreement. Concentrations calculated using the 409nm calibration curve were used above the cutoff value, while the 630nm line was used below the cutoff value. This method did not introduce any discontinuities in the data because of the strong agreement between the two different estimates within this overlap range.

Breakthrough curve parameters were estimated using the computer program STAMMT-L [*Haggerty and Reeves,* 2000] with the program configured to solve multi-rate, one-dimensional mass transfer [*Haggerty and Gorelick,* 1995], using the same formulation as chapter 2, eq. 6:

$$\frac{\partial c_m}{\partial t} + \Gamma(x,t) = \frac{v_x}{R_m}\left(\alpha_L \frac{\partial^2 c_m}{\partial x^2} - \frac{\partial c_m}{\partial x}\right) \tag{1}$$

where $c_m$ is the mobile domain concentration, $v_x$ the velocity, and $\alpha_L$ the dispersivity, all mobile domain parameters. Because the solute does not sorb, we set $R_m$, the retardation factor, to 1. $\Gamma(x,t)$ is a transient source/sink term incorporating multiple rates and volumes of mass transfer:

$$\Gamma(x,t) = \sum_{j=1}^{N} \beta_j \frac{\partial (c_{im})_j}{\partial t} \tag{2}$$

where $c_{im}$ is the concentration in the immobile domain, and $\beta_j$ is the ratio of each immobile domain pore volume to mobile domain pore volume, such that:

$$\sum_{j=1}^{N} \beta_j = \beta_{tot} \tag{3}$$

with $\beta_{tot}$ the ratio of all immobile pore space to mobile pore space. Equation 2 is coupled with equation 1 using:

$$\frac{\partial (c_{im})_j}{\partial t} = \alpha_{m,j}\left[c_m - (c_{im})_j\right] \tag{4}$$

where $\alpha_{m,j}$ is the rate coefficient of mass transfer.

In our experiments, we use cylindrical emplacements of low conductivity. If the pore space inside the cylinder is truly advectively immobile, then solute movement is driven exclusively by diffusion, as detailed in *Crank* [1975]. Diffusion into a cylinder has also been described in detail in the form of multi-rate mass transfer and mass transfer memory functions [*Haggerty and Gorelick,* 1995; *Haggerty, et al.,* 2000]. If significant advection occurs in the cylinder, analtyical studies of advective flowpaths through elliptical inclusions have been performed, of which cylinders are a specific case [*Wheatcraft and Winterberg,* 1985; *Strack,* 1989; *Lessoff and Dagan,* 2001]. Although we will make use of solutions for advection through a cylinder, STAMMT-L does not incorporate advection-driven mass transfer in its solution method. Therefore, we use the program to estimate parameters for diffusion-driven mass transfer. Given the geometry of our experiment, we set STAMMT-L to use analytical solutions for cylindrical diffusion [*Haggerty and Gorelick,* 1995] to calculate the α's and β's:

$$\alpha_{m,j} = r_{0,j}^2 \frac{D_a}{a^2} \tag{5a}$$

$$\beta_j = \frac{4}{r_{0,j}^2} \beta_{tot} \tag{5b}$$

where $r_{0,j}$ is $j^{th}$ root of $J_0(x)$, the zero-order Bessel function of the first kind, a is the radius of the cylinders and $D_a$ is the diffusion coefficient. STAMMT-L was set to truncate this infinite series at 50 terms, but this introduces negligible error (see *Haggerty and Gorelick* [1995]). Data was fit with a log-weighted least-squares scheme in order to ensure good fits of breakthrough curve tails. Although this methodology can simulate cylindrical diffusion and situations with no mass transfer (by small values of $\beta_{tot}$), it cannot simulate slow advection through cylinders. We address this problem in the results section and Appendix B.

Processing the tank images required four discrete steps. In the first step, we adjusted light intensity measurements to compensate for shifts in the brightness of the light box. We used the wedge, which has several gray-level gradations on it, by measuring the average light intensity in each of these gradations for each picture. We compared these values to the wedge brightness levels of a baseline image and used the differences to recalibrate the light intensity values of all pixels in the picture (see, for example, *Detwiler, et al.*, [1999]).

In the next two steps we adjusted the picture to compensate for any drift in the camera field during the experiment. We selected a particularly distinct object on the baseline image and then systematically compared the other images to it (the feature of interest was a part of the wedge that possessed a dramatic light intensity shift in both the x and y directions). We first adjusted any images that differed by more than a full pixel, shifting them to be less than one pixel in difference. We then corrected the partial pixel drift using the method described in *Detweiler, et al.* [1999]. These three steps produced images that were that were normalized to the same bases of position and background light intensity.

Concentrations were calculated at each pixel by comparing that pixel's intensity in the water-saturated tank image (step 2 of the procedure) and the dye-saturated tank image (step 4) using the Beer-Lambert law:

$$\frac{C_i}{C_0} = \frac{\ln(I_i) - \ln(I_{i,w})}{\ln(I_{i,0}) - \ln(I_{i,w})} \tag{6}$$

where $C_i$ is the dye concentration at pixel i, $C_0$ is the concentration when the image is saturated with dye (30 mg/l), $I_i$ is the light intensity of pixel i, $I_{i,w}$ is the light intensity in the water-only image of that pixel, and $I_{i,0}$ is the light intensity in the dye saturated image of pixel i.

## 4.3 Experimental Validation

We ran several diagnostics to confirm that our experimental methods and assumptions were valid.

**Lightbox Stability:** The technique of compensation for shifts in light box intensity may fail if light box intensity varies by a large amount. To check this we set the camera to take a picture of the diffuser plate on the light box every hour for a period of approximately 200 hours. We gray-level adjusted the images and examined the difference in the average light intensity at each hour as compared to the intensity at the first hour. Prior to gray-level adjustment, it was low, approximately 3 percent at the largest. After adjustment, changes dropped to less than 1 percent, suggesting that lightbox variability is sufficiently low for our experiments, particularly after gray-level adjustment.

**Linearity of Light Transmission:** To test our assumption that the Beer-Lambert law accurately describes the relationship between absorbance and concentration we systematically flooded a completed tank with multiple known concentrations of dye and took an image at each concentration. Several small (10 pixel by 10 pixel) areas were selected and compared across all images. We calculated the average concentration in each area using equation 6 (and water-saturated and 30mg/l-saturated tank images). Figure 4a compares the calculated concentrations to the actual concentration flushed into the tank by plotting the mean of the concentration estimates from each image (circles) and the ideal prediction (solid black line). Our method seems to have consistently overestimated actual concentration by a small amount, though conforming to a linear relationship (in log-log space) that deviates slightly from the ideal. The data is more accurately fit by the relationship:

$$C_{est} = 1.33C_{act}^{0.92} \tag{7}$$

where $C_{act}$ is the true concentration, and $C_{est}$ is the estimated concentration using the perfect Beer-Lambert assumption (equation 6). This new function is shown in figure 4a as the dashed line, and was applied to calculated concentrations after using the Beer-Lambert law, although this function has minor overall impact.

High variability in mean concentration estimates can indicate that even relatively accurate mean estimates will show unacceptably large noise on a point-by-point basis. We looked at the coefficient of variation of the concentration estimates (the same ones used to calculate the mean in the figure 4a), and the results (figure 4b) show a significant increase in variability between concentrations of 0.2mg/l and 0.1mg/l, from a relatively low initial level. We concluded that concentration calculations down to approximately 0.2mg/l (about two orders of magnitude below our maximum concentration) are probably reliable, but lower values are questionable.

**Mass Balance:** Lastly, we compared the calculated mean concentration in entire tanks during the actual experiments to theoretical mean concentrations, which checks the reliability of concentration estimates through mass balance. We examined calculated concentrations for several images in all three tanks at identical flow rates (1.32ml/min). The errors in our calculated total mass as compared to the theoretical (using the dimensions of the tank and the estimated porosity) are plotted in figure 4c. Both the advective mass transfer tank and advective-dispersive tank are in exceptionally good agreement with the theoretical. The diffusive mass transfer tank, while in relatively good agreement, is not as accurate as the other two tanks. We theorize a reason for this inconsistency in the following section of this work. Agreement with the theoretical mean concentration tends to worsen as time goes on. This is due to increasingly large areas with very low dye concentration, where the reliability of our estimates tends to break down.

From our series of experimental validations, we conclude that our method is does a good job of estimating concentrations throughout the tank, with the caveat that at concentration measurements below approximately $0.01C_0$ are probably of limited reliability.

## 4.4 Results

We divide this section into two pieces, each focusing on a particular aspect of the experiments. The first deals with the imaging results from the experiments as a convenient means of describing the fundamentally different solute transport behaviors, the second with analysis and comparison of the breakthrough curves.

### 4.4.1 Tank Images

Our method obtained images of the tanks as flow occurred that were accurate over about two orders of magnitude in concentration (relative to initial concentration) and could be taken with very high frequency. Space constrains our ability to show complete data sets, but we have a website with downloadable movies of each of the three processes (http://web.mit.edu/harvey-lab/www/Regimes_Page/movs.html). We show in figure 5 a few images from each tank, spaced through time to illustrate the three observed behaviors. The figure shows results from each tank at the same flow rate (1.32 ml/min), with the same color scale (indicated by the color bar in the lower right). Each tank image represents an area approximately 40cm long and 20cm wide. Although flow in the actual tank was vertical, we have rotated the images by 90 degrees clockwise for easier organization. Thus, flow is from left to right in these images, with initial dye saturation everywhere, followed by constant flow flushing with clean water.

The first column shows results from the advective-dispersive tank. The images resemble classic dispersion scenarios, with a front propagating through the entire tank and velocity variation leading to spreading. The effects of the emplacements can be clearly seen – flow in these areas is slower. It appears from the images that emplacement flow is fast enough that solute movement does not tail significantly behind the main front. The emplacements appear to only introduce spreading to the plume, not tailing.

The next two columns are images from the diffusive mass transfer tank (twice as many images are shown). The first difference between this tank and the advective-dispersive tank appears at early times – flow through emplacements in this tank is unobservably small at early times. Flow diverts around the emplacements completely, leaving them saturated with dye despite the fact that the main body of the plume has passed by. As time passes (second column), solute slowly diffuses out of the emplacements. After a day, there is still significant solute left in the emplacements, while the advective-dispersive tank was basically clean after four hours.

The diffusive mass transfer tank's images display problems caused by beads settling in the emplacements. Because beads were packed in a different orientation than the final tank position, they sometimes settled enough that small gaps formed at the top of the emplacements. Although the open spaces had no discernable effects on the flow field, they caused imaging difficulties because the holes that were cut in the neutral density light filter did not completely cover them. This left an unfiltered path for light to pass through the tank, resulting in unacceptably high light intensity in these areas. To fix this problem, we were forced to cut small slivers of filter and tape them over the areas where excess light penetrated the tank, which caused a reduction in resolution in areas outside the emplacement that were filtered twice. The tape also caused problems because it scatters a great deal of light. These problems are visible in the images of the diffusive mass transfer tanks (see figure 5). The total area disrupted by these measures was deemed small enough that visualization was still accurate, but the area behind these filters and tape did introduce significant error into particular areas. We believe these errors are largely responsible for the mass balance discrepancies in this particular tank (see previous section).

The next column (first column on the second page of the figure) shows a close-up of an individual emplacement, added because it is difficult to make out fine details in the full tank pictures. The white box in the full tank picture denotes the particular emplacement. Images of the emplacement show classic behavior for diffusion out of a cylinder – circularly symmetric solute concentrations with highest values in the middle of the emplacement. This ring-like pattern agrees with analytical solutions [e.g., *Crank,* 1975]. One interesting characteristic is that the ring is not perfectly symmetric, but appears to be shifted slightly in the direction of flow. This suggests that advection through the emplacement is extremely slow, but is large enough to cause a small amount of solute displacement.

The final three columns show results from the advective mass transfer tank (again, two columns of tank images, third column focusing on one emplacement). At early times, the behavior in this tank is indistinguishable from the diffusive mass transfer tank – the main advective front flows around emplacements, enabling significant tailing. Late-time behaviors, however, diverge significantly – instead of diffusing out of the emplacements, solute primarily advects across them slowly. We can see this particularly in the images focusing on a single emplacement (in both cases the same emplacement was focused on). Where the diffusive mass transfer case shows a radial release of solute, the advective mass transfer case is more akin to plug flow (with some dispersion) through the emplacement – clean water is transported in at the upstream end and dyed solute flows out at the downstream end. This advection process, although slow, occurs faster than diffusion, as overall concentration in the advective mass transfer tank at 1035 minutes is already lower than in the diffusive mass transfer tank at 1710 minutes.

### 4.4.2 Breakthrough Curve Parameter Estimates

We fit the breakthrough curves for the experiments with the cylindrical diffusion mass transfer model (see post-processing section). Parameter estimates are given in table 2. Because the diffusion model did not fit the advective mass transfer case very well we used an alternate model with alternate parameters to fit the breakthrough curve (detailed in Appendix B).

The advective-dispersive case is the simplest scenario to fit, as ideally there should only be two parameters (velocity and dispersivity), a reasonable assumption given that the tank did not visually appear to display mass transfer. However, we fit the breakthrough curves with the cylindrical diffusion model to confirm this.

The breakthrough curves from the two experiments run in the advective-dispersive tank are shown in figure 6. We were forced to take hand samples for these breakthrough curves, which degrades both the quality and quantity of data. Use of hand samples was necessitated by a pinhole leak that occurred in the top right corner of the tank. This leak caused the air to entrain in one of the ourflow hoses. The flow cell cannot be used when air bubbles are present in the outflow because the bubbles become stuck in the cell, invalidating absorption measurements. The data points are shown as black circles on the graph, with the best fit using STAMMT-L shown as the dotted line. Breakthrough curves are plotted in log-log format to allow for better illustration of the tails.

Both experiments are fit well by the model. The data is noisy due to the use of hand samples, but the curves qualitatively look like advective-dispersive scenarios – in log-log space, the curve starts flat and then turns sharply in a downward linear fashion that continues unabated.

Parameter estimates (see table 2) confirm no significant mass transfer occurring in either experiment (low estimated values of $\beta_{tot}$).

For the diffusive mass transfer experiments (figure 7) the appearance of the breakthrough curves differs significantly from the advective-dispersive curves, with a significant tail apparent in the curve. Outflow concentration in the tail falls steadily, but less rapidly than the dropoff during advective breakthrough, and at late times resumes a sharper descent. This qualitatively matches what we would expect the tail to look like (see *Haggerty, et al.*, [2000]). Use of the flow cell for these experiments allowed nearly continuous data (the lines in the graphs are composed over 1000 data points each).

Fits of the breakthrough curves using the cylindrical diffusion model are difficult to see in the figures. This is because the estimates fit the data almost perfectly, creating two curves plotted on top of one another. We illustrate a few of the actual data points with black circles.

Parameter estimates (table 2) for these two experiments agree well with the known physical parameters of this system. Given the volume of the emplacements (approximately 1/3 of the tank), we would estimate a $\beta_{tot}$ of 0.5, slightly higher than the actual estimates. Estimated diffusion coefficients also possess reasonable values. STAMMT-L estimates a value of $3.5*10^{-10}m^2/s$ for both experiments. We measured the diffusion coefficient of the dye in open water to be $5.6*10^{-10}m^2/s$, suggesting a bead pack tortuosity of 0.6, a reasonable value for packed spheres [*Bear,* 1972]. Estimates for the diffusion coefficients in the two experiments differ by less than 2 percent. This reinforces the conclusion that the tailing in this tank is caused by diffusive processes, which have time scales that are independent of head gradients.

The advective mass transfer tank shows breakthrough curve behavior that does not qualitatively resemble either advective-dispersive or diffusive mass transfer (figure 8). There is clearly tailing in both experiments, but the tails display different characteristics than in the diffusive mass transfer case. Figures 8a and 8b plot the advective mass transfer experimental data along with the diffusive mass transfer data at the same flow rate. The early part of the tail is much flatter in the advective mass transfer scenario, i.e., outflow concentration is higher. In the later parts of the tail, the advective case takes a much sharper downturn than the diffusive scenario, and quickly drops below the diffusive scenarios' outflow concentration. The differences between the advective and diffusive curves at the faster flow rate (1.32ml/min) are greater than at the slower rate.

A good fit to the advective mass transfer curves with the cylindrical diffusion model is not possible. Figure 8c shows that the best fit for the faster (1.32ml/min) experiment fails to adequately describe the breakthrough curve (and also estimates unrealistic values, like a $\beta_{tot}$ of 0.78). We were forced to develop our own model to fit the breakthrough curve.

Appendix B describes the model in detail. We solved analytically for the advective flux out of a cylinder and discretized the outflow into streamtubes, then incorporated longitudinal dispersion/diffusion by applying the analytic one-dimensional solution for advection and diffusion to each tube. The fit from this model, shown in figure 8c, fits the breakthrough much better than the diffusion model. The weakness of the fit is at early times in the tail, suggesting that the one thing our model does not incorporate, lateral dispersion/diffusion, is actually significant at early times. The overall fit, however, is satisfactory for our purposes, particularly in demonstrating that it is slow advection that is driving much of the tailing.

Some interesting characteristics are evident in the advective mass transfer parameter estimates (table 2). The estimate of $v_{in}$, the velocity inside the emplacements is about two orders of magnitude less than outside in both cases. This supports our estimate that the conductivity difference between the two regions is about a factor of 300. The faster experiment shows a velocity difference slightly greater than a factor of 100, while the slower experiment shows a difference of slightly less than a factor of 100. This is due to our model becoming less accurate as diffusion becomes more important, with our model estimating a faster velocity to account for faster movement of solute produced by relatively larger diffusion.

Dispersivity estimates in the mobile domain were much closer to dispersivity estimates in the emplacements than the velocity differences. Dispersivity inside the emplacements is much larger than the average bead diameter in the emplacements, suggesting that diffusion must also play a role inside the emplacements.

Differences between the advective and diffusive mass transfer experiments are substantially greater for the faster flow rate experiment than the slower. In fact the advective mass transfer curve for the 0.66ml/min experiment has a shape somewhere between the faster advective mass transfer curve and a classic diffusive mass transfer scenario, which suggests that neither advective nor diffusive mass transfer processes completely dominate the experiment.

## 4.5 Discussion

The experiments show clear behavioral differences in the three tanks, both at the small-scale level (tank imaging) and at the upscaled level (breakthrough curves). This points to different fundamental behaviors in connected conductivity fields – traditional advection and dispersion, mass transfer dominated by diffusive processes, and mass transfer dominated by advective processes.

One might argue that the advective and diffusive mass transfer tanks are not actually different – increasing the head gradient in the diffusive tank or decreasing it in the advective tank by sufficient amounts would create similar scenarios. This is true, and suggests that mass transfer is a fundamentally competitive process in these systems. In our experiments, conductivity contrast serves as a controlling component of advective velocity through the low conductivity areas, dictating the ratio of the advective time scale to the diffusive time scale in these regions. The faster process will dominate the mass transfer. This is in contrast to the advective-dispersive tank, where the conductivity contrast is so low that mass transfer does not occur, at any flow rate, i.e., there is no immobile domain.

We can see the lack of an immobile domain by comparing the velocity estimates for the three experiments with the same flow rate (1.32ml/min). Velocity estimates in the two mass transfer tanks are close to each other (within 10 percent), both approximately 1.5 times the estimate for the advective-dispersive tank. This is because the emplacements take up 1/3 of the total volume of the tank, and if emplacements are not part of the mobile domain, flow is restricted to 2/3 of the tank. Thus flow must move 1.5 times as fast in order to maintain the same volumetric flow rate. The velocity difference points to an immobile zone (or, more accurately, a low mobility zone) that is present in the mass transfer tanks but absent in the advective-dispersive tank.

Dispersivities in the three tanks are relatively close to one another, with values ranging from 0.46cm to 0.7cm, a length scale of about half of the emplacement radius. The one outlying experiment is the advective-dispersive tank with a flow rate of 4.1ml/min, which has a dispersivity estimate that is twice as high as any other experiment. We attribute this to the fact that air entrapment in the right-hand outflow tubing was severe enough in this experiment to frequently block flow. This led to larger apparent spreading as flow was forced to move laterally across the tank to exit through the other two outflow tubes. Given how much higher this dispersivity estimate is than all of the others, and given that this was the only tank that suffered serious outflow problems from trapped air bubbles, it seems reasonable to attribute this discrepancy to bubble entrainment error. One additional observation is that dispersivity estimates increase as the conductivity contrast in the tanks increases (this is particularly visible by looking at the results for the three experiments with flow rates of 1.32ml/min). This is consistent with general stochastic theory regarding dispersivity as a function of field variance, and consistent with our numerical simulations later in this thesis.

It is clear that fundamentally different processes are driving the mass transfer in the advective and diffusive mass transfer tanks. The shape of the breakthrough curves suggests that advection-driven mass transfer occurred sooner than that caused by diffusion in the advective mass transfer experiments. This is the result of the characteristic time of diffusion in emplacments significantly exceeding the characteristic time for advection, thus causing advection to dominate. We see further qualitative evidence of this in the breakthrough curves. The advective mass transfer experiment with the lower flow rate more closely resembles its corresponding diffusive mass transfer experiment than does the faster experiment. This points to advective processes being significant to the mass transfer process – as flow rate (velocity) decreases, the rate at which advective mass transfer occurs decreases toward the time scale of diffusive mass transfer. In a diffusion-controlled mass transfer process, the tail should not be affected by the head gradient, as was the case in the diffusive mass transfer experiments.

This all points to both diffusion and advection acting as a coupled process in driving mass transfer in connected fields. Although it is possible for one process to dominate the other, there is no reason to believe that situations with more closely equal time scales do not exist in the real world, which could have important implications for parameter estimation and remediation decisions.

## 4.6 Conclusions

The flow experiments discussed in this chapter visualized small-scale flow while simultaneously measuring outflow concentration from an artificially constructed porous medium. The system was designed to allow high resolution in concentration measurements so that low concentrations at late times could be observed. The system was also unique in creating a connected conductivity field with conductivity differences of greater than three orders of magnitude, much larger than any previous visualization experiments using constructed media. These large conductivity differences create conditions that drive three fundamentally different upscaled behaviors – advection with dispersion, advective mass transfer, and diffusive mass transfer. These different behaviors can be observed both inside the experimental apparatus and in the tank outflow, demonstrating that fundamentally different small-scale behaviors drive fundamentally different upscaled behaviors.

Parameter estimates performed on the breakthrough curves give estimates of diffusion coefficients, capacity coefficients, and dispersivities that are reasonable given the physical configuration of the tanks and the dye used. These estimates confirm our qualitative observations of solute transport behavior in the three different tanks. Parameter estimates confirm, for example, that no significant mass transfer occurs in the advective-dispersive tank. Diffusion coefficient estimates also confirm that the mass transfer process in the diffusive mass transfer tank is almost entirely diffusion-driven. For the advective mass transfer tank, we were forced to develop our own simplistic model to describe the flow (see Appendix B). Although the model does not fit perfectly, it demonstrates that our characterization of the mass transfer as primarily advective in nature seems to be reasonable. Furthermore, as we reduced the flow rate (and thus the hydraulic gradient) in the advective mass transfer tank, breakthrough began to look more like the breakthrough in the diffusive mass transfer case. This points to a mass transfer in this system being at least partially competitive, in the sense that either diffusion or advection or a combination of both can dominate the mass transfer, depending on various conditions of the flow field.

| Tank | Large Bead Size | Small Bead Size | K Contrast | Filter |
|---|---|---|---|---|
| Advective-Dispersive | 2.1 mm | 900 μm | 6 | 50% |
| Advective Mass Transfer | 2.1 mm | 135 μm | 300 | 12.50% |
| Diffusive Mass Transfer | 2.1 mm | 57 μm | 1800 | 6.25% |

**Table 4-1:** Comparison of the bead sizes and light filters used in the three tanks. The large bead size indicates the mean bead diameter of the beads outside of the emplacements, the small bead size represents the mean diameter inside. The approximate conductivity ratio between these two regions is calculated, with edge effects incorporated. The filter column represent the percent of light was allowed to enter the large bead area (100% was allowed to enter inside the emplacements).

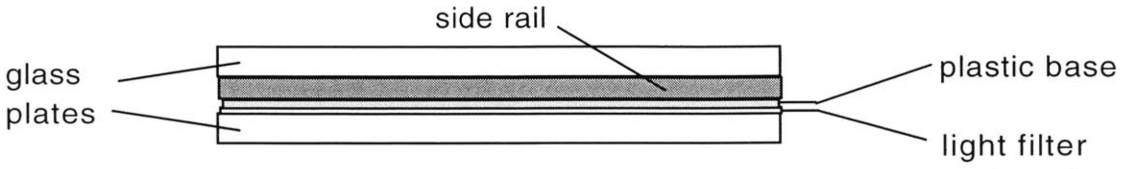

**1A -- side view** (prior to addition of screw plates and end manifolds)

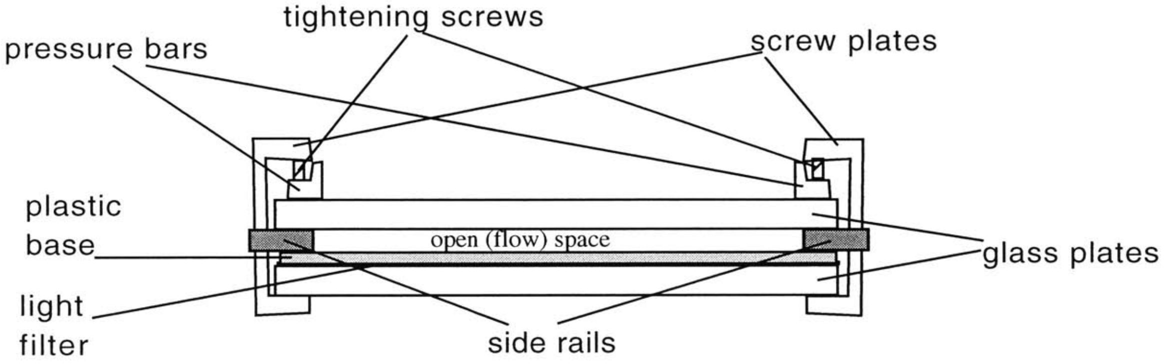

**1B --top view** (prior to addition of top manifold and gasket)

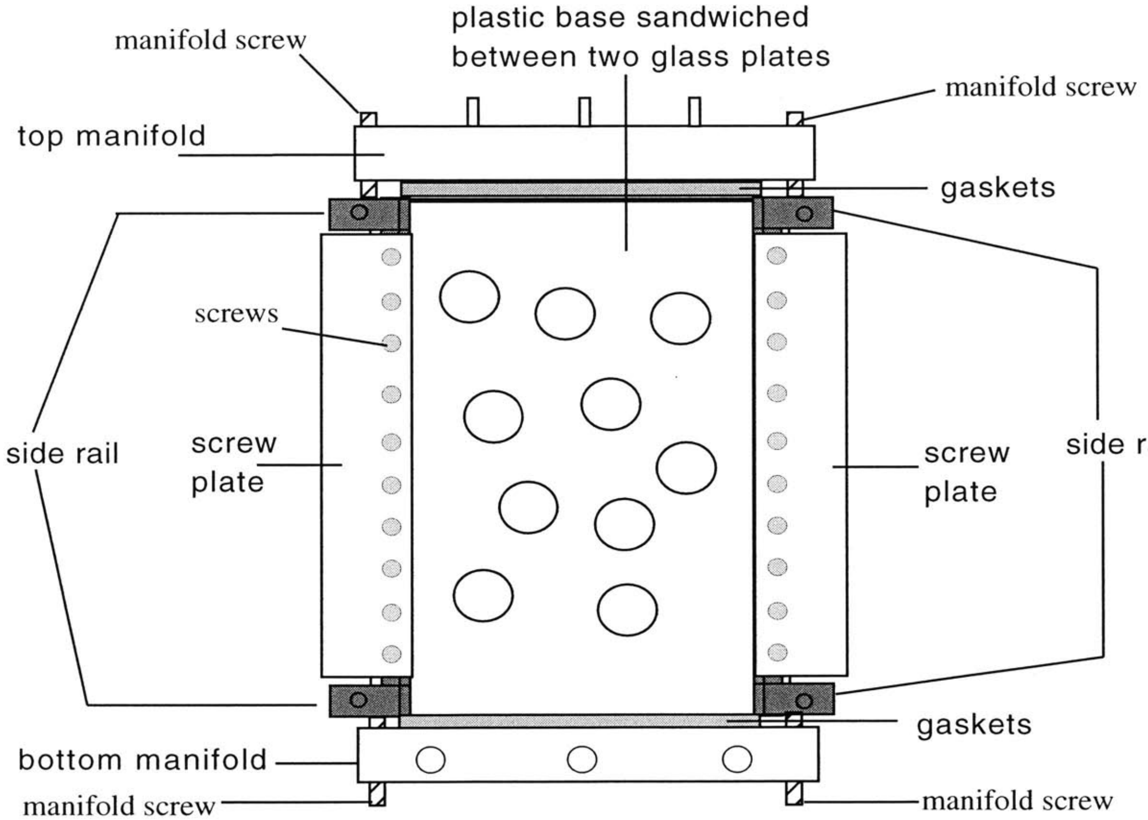

**1C --front view** (completed tank)

**Figure 4-1:** View of experimental tank at various stages of construction from various angles. 1A shows a side view before tightening with screw plate. 1B shows a top view after it has been secured with pressure bars and the screw plate. The flow area for the experiment is the open space between the two side rails. 1C shows a front view of the tank with the manifolds added, i.e., the completed tank.

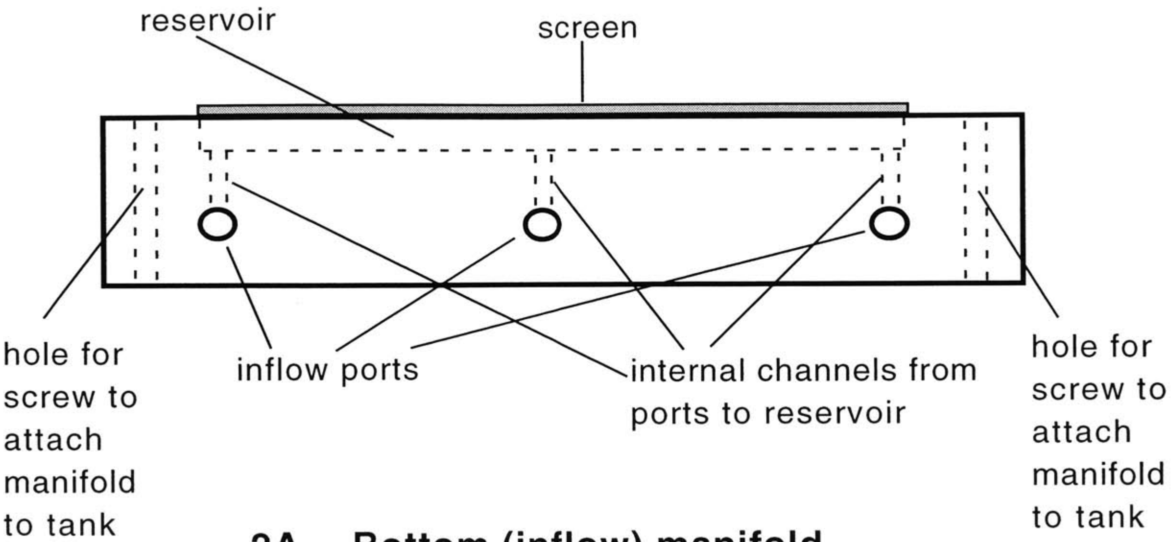

**2A -- Bottom (inflow) manifold**

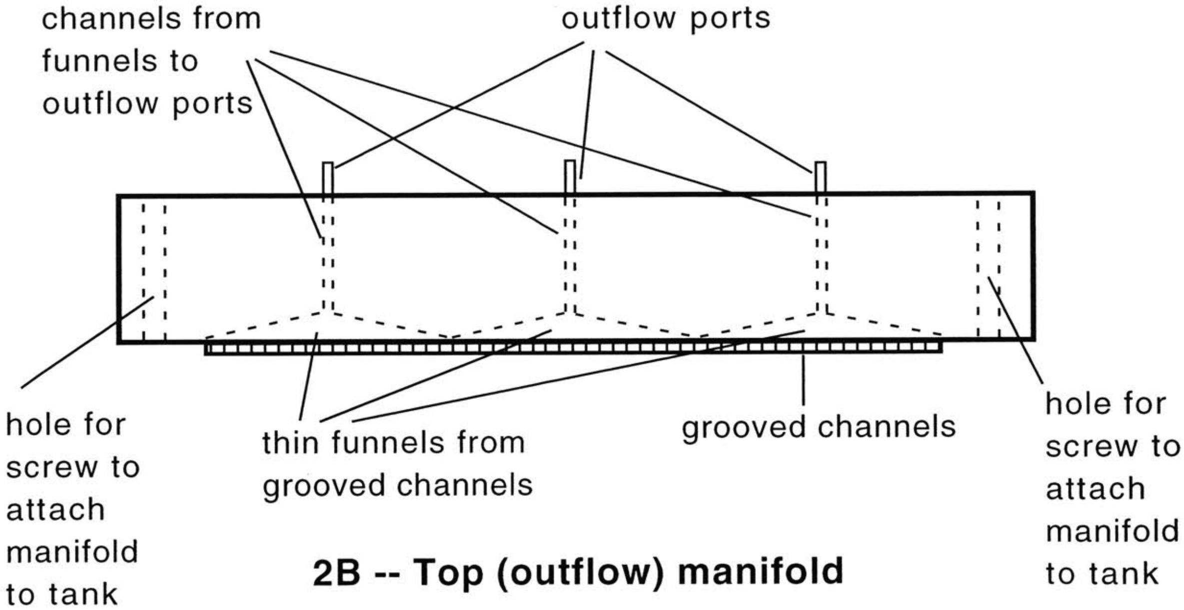

**2B -- Top (outflow) manifold**

**Figure 4-2:** A detailed side view of the two manifolds, both specially designed for this experiment. The top manifold is designed to minimize mixing volume of the outflow and to prevent stagnation zones or heterogeneities along the outflow boundary. The bottom manifold has a reservoir that can be flushed without significantly affecting the interior of the tank, establishing a much more reliable boundary condition.

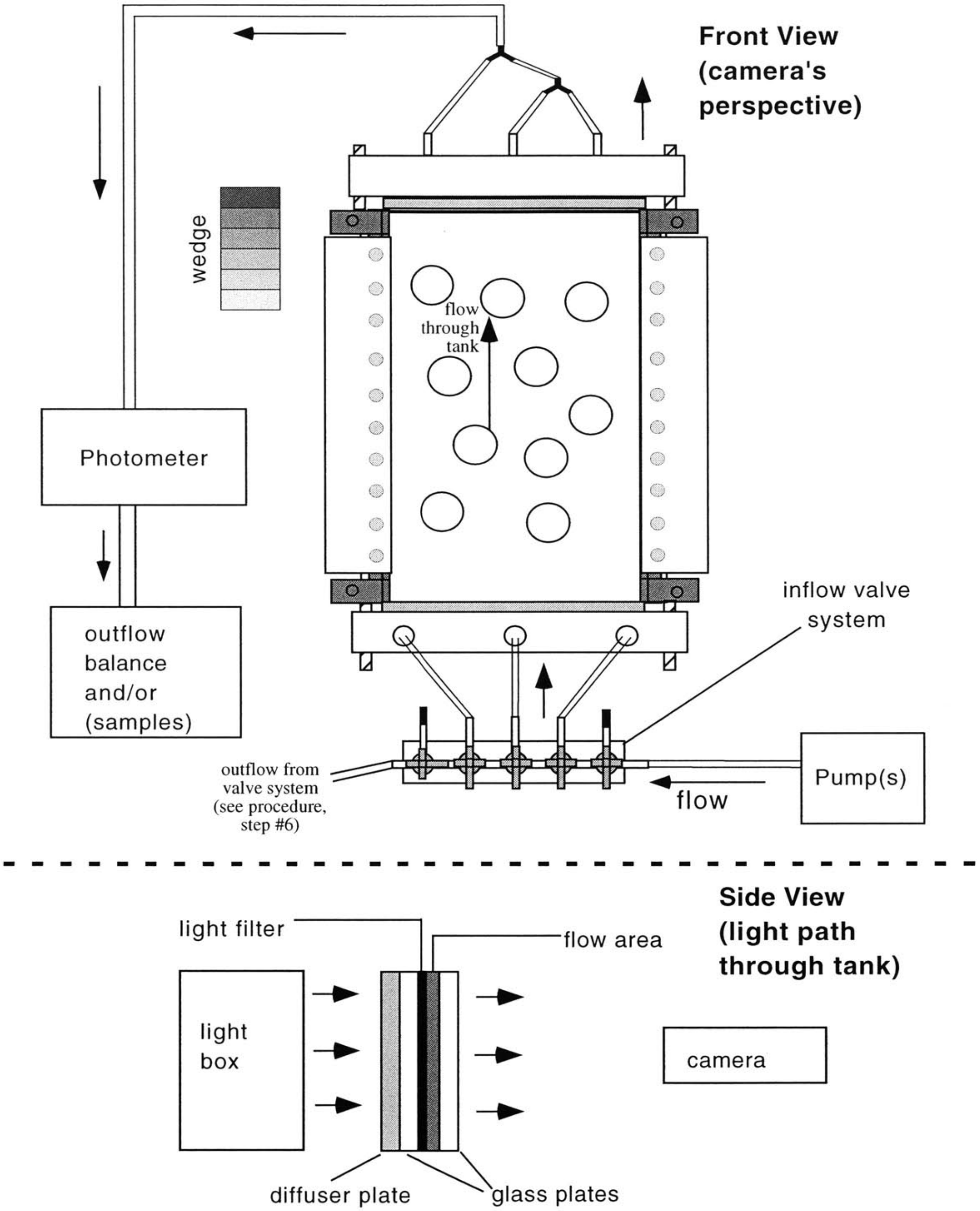

**Figure 4-3:** The completed experimental setup from two different perspectives. Shown at the top is the view, as seen by the camera, of the system, with the lightbox behind the tank. The valve system is used to flush the reservoir in the inflow manifold clean of dye prior to the experiment (see step #6 in the procedure). Clean water is then flushed through the dye-saturated tank, with tank outflow sent to the photometer. The bottom figure shows a side view of the path that light follows from the light box to the camera.

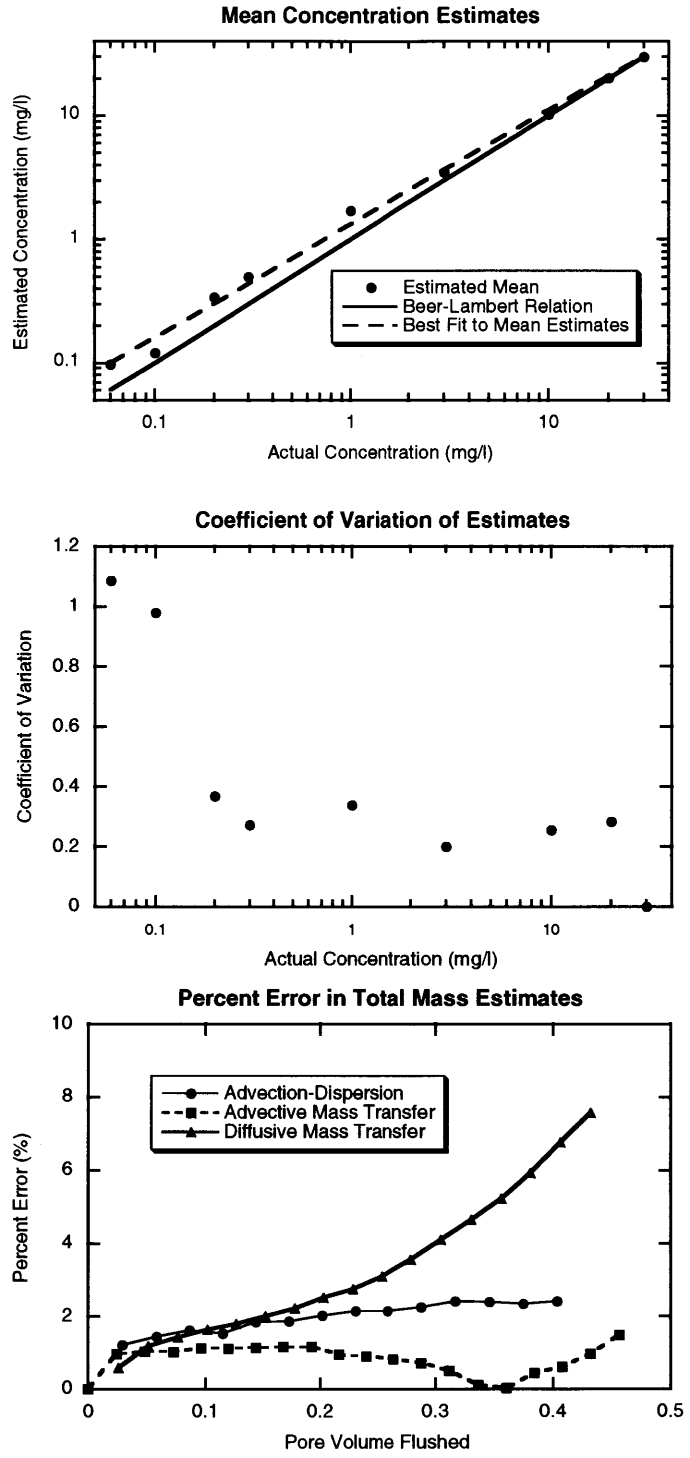

Mean Concentration Estimates

Coefficient of Variation of Estimates

Percent Error in Total Mass Estimates

**Figure 4-4:** Experimental methodology checks. The first graph shows mean estimated concentrations using the Beer-Lambert assumption in one of our tanks, versus the known actual concentration, along with a linear best fit that varies slightly from the ideal. The second figure shows the coefficient of variation of the concentration estimates, which remains low until a sharp increase at a concentration of 0.1mg/l. The third graph shows the percent error in total dye mass as measured by camera images compared to the actual dye mass. Overall agreement is good, despite some deterioration with time.

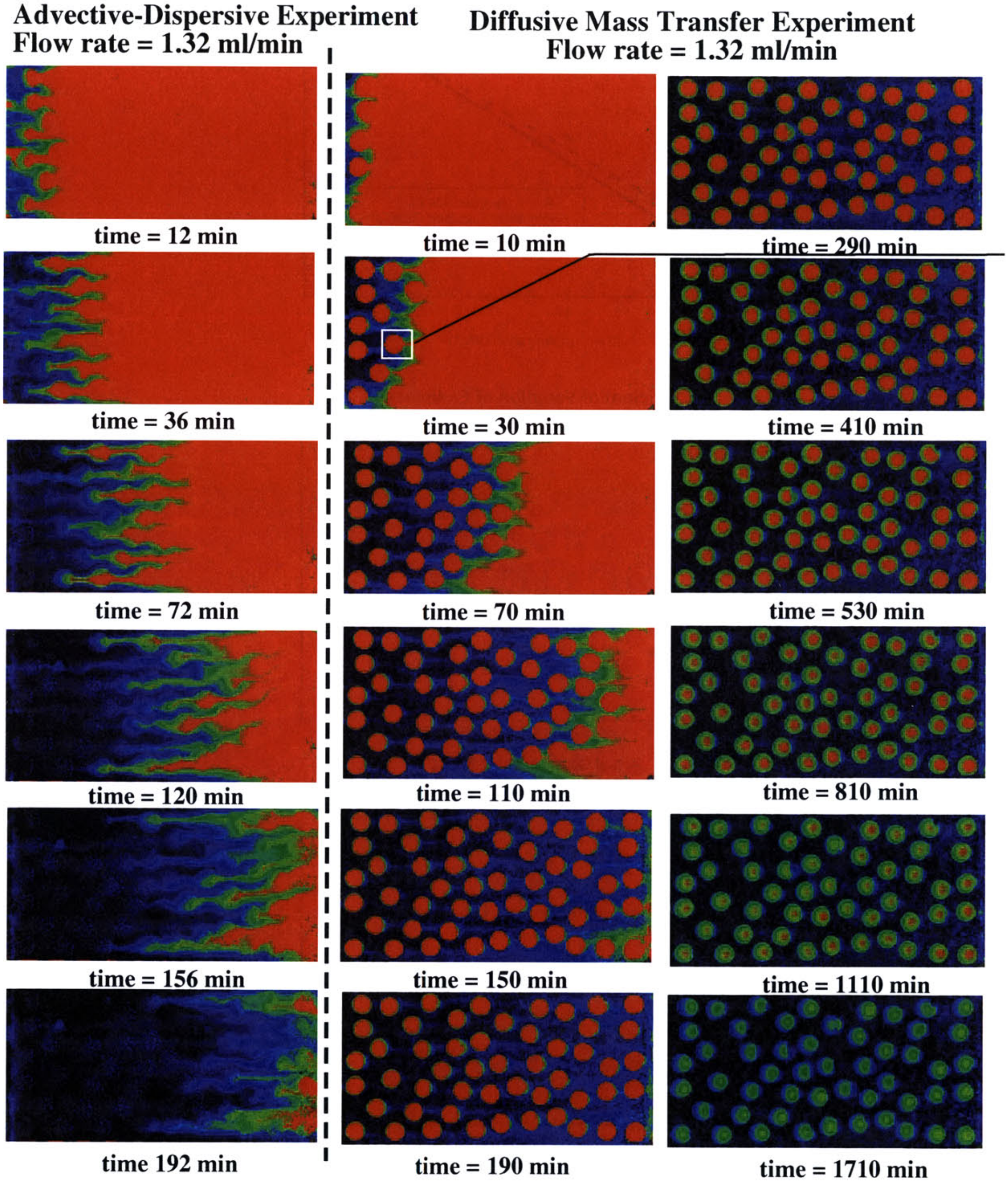

**Advective-Dispersive Experiment**
**Flow rate = 1.32 ml/min**

**Diffusive Mass Transfer Experiment**
**Flow rate = 1.32 ml/min**

**time = 12 min**
**time = 10 min**
**time = 290 min**

**time = 36 min**
**time = 30 min**
**time = 410 min**

**time = 72 min**
**time = 70 min**
**time = 530 min**

**time = 120 min**
**time = 110 min**
**time = 810 min**

**time = 156 min**
**time = 150 min**
**time = 1110 min**

**time 192 min**
**time = 190 min**
**time = 1710 min**

**Figure 4-5:** Series of color images representing solute concentration as a function of time for each of the three tanks, all run with the same flowrate. Concentration is represented as fraction of initial, as noted on colorbar to the right. Close up of a single emplacement is shown for the two mass transfer cases, illustrating fundamentally different behavior, with one dominated by diffusion and the other by advection.

**Advective Mass Transfer Experiment**
**Flow rate = 1.32 ml/min**

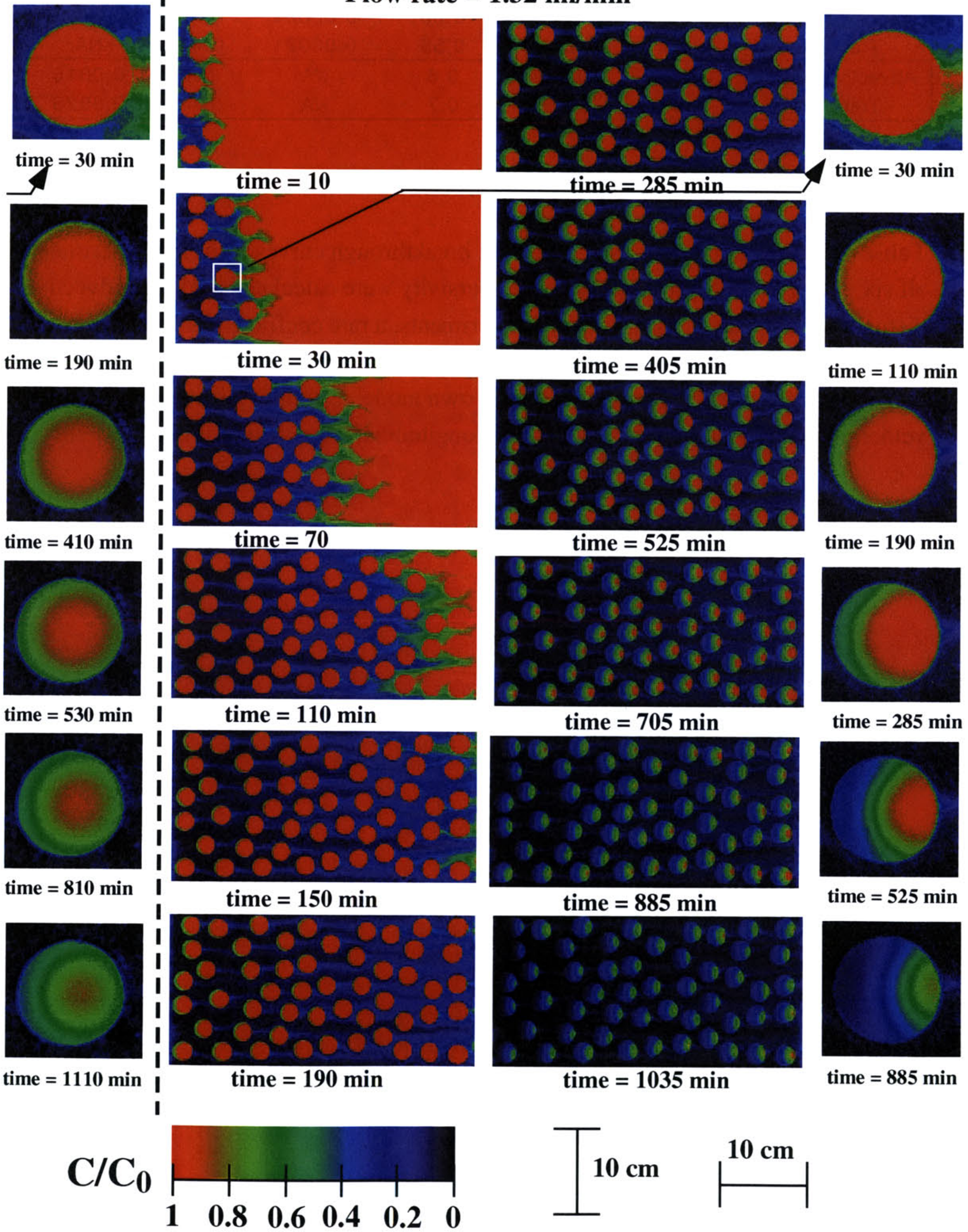

| Tank | Flow Rate (ml/min) | Velocity (cm/min) | Dispersivity (cm) | Diff. Coeff. ($cm^2$/min) | $\beta$ | $V_{in}$ (cm/min) | $Disp_{in}$ (cm) |
|---|---|---|---|---|---|---|---|
| Advective- | 1.32 | 0.195 | 0.46 | 0.0058 | 0.04 | NA | NA |
| Dispersive | 4.1 | 0.57 | 1.22 | 0.004 | 0.01 | NA | NA |
| Diffusive Mass | 0.66 | 0.149 | 0.68 | 0.00021 | 0.48 | NA | NA |
| Transfer | 1.32 | 0.297 | 0.55 | 0.00021 | 0.46 | NA | NA |
| Advective Mass | 0.66 | 0.13 | 0.6 | NA | NA | 0.0016 | 0.19 |
| Transfer | 1.32 | 0.275 | 0.7 | NA | NA | 0.0025 | 0.28 |

**Table 4-2:** Parameter estimates for the six breakthrough curves from the experiment. For all six, a mobile domain velocity and dispersivity were calculated. For the advective diffusive and diffusive mass transfer experiments, a rate coefficient and partition coefficient were also calculated, with an assumed model of cylindrical diffusion. For the advective mass transfer case, we used our own model, estimating instead the (slow) velocity inside the emplacement, and the longitudinal dispersivity of this slow advection.

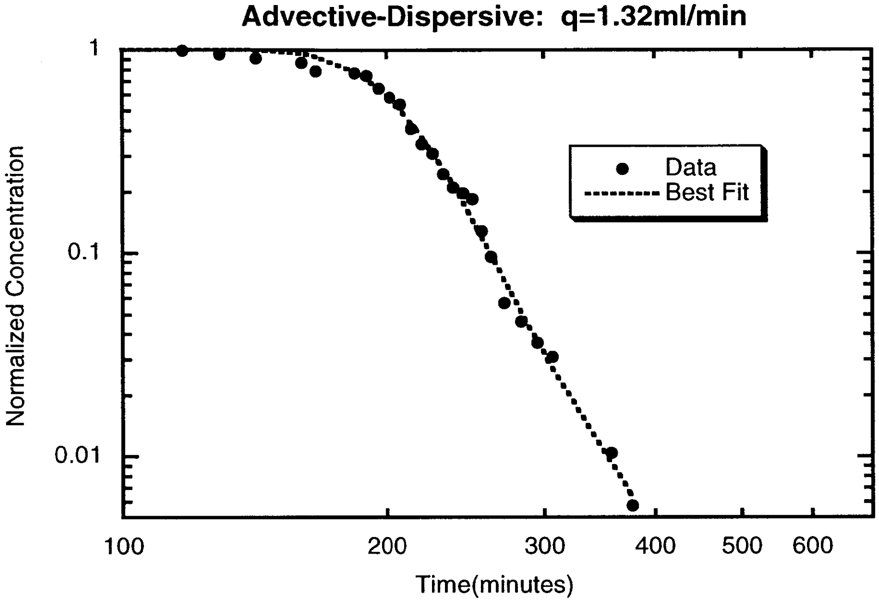

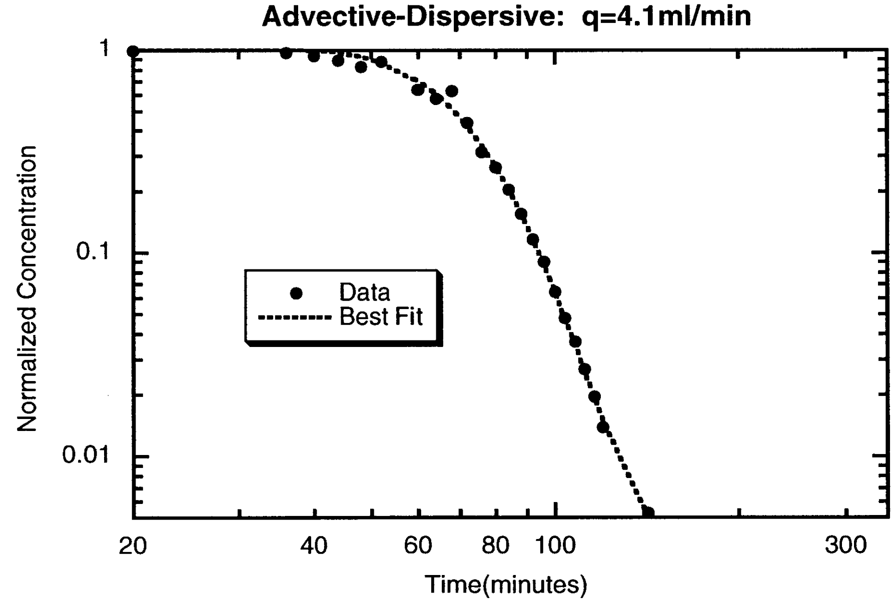

**Figure 4-6:** Advective-dispersive experiment breakthrough curve data and best fits. The shape of the curves (and parameter estimates) indicates little mass transfer (tailing) is occurring. Sporadic data and noisy data caused by air in outflow, necessitating use of hand samples instead of continuous flow cell reading in photometer.

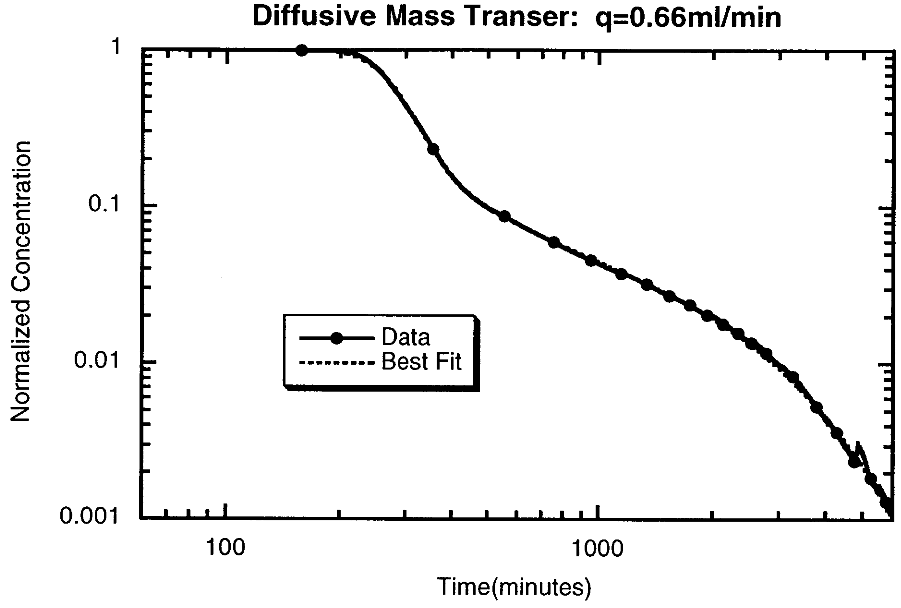

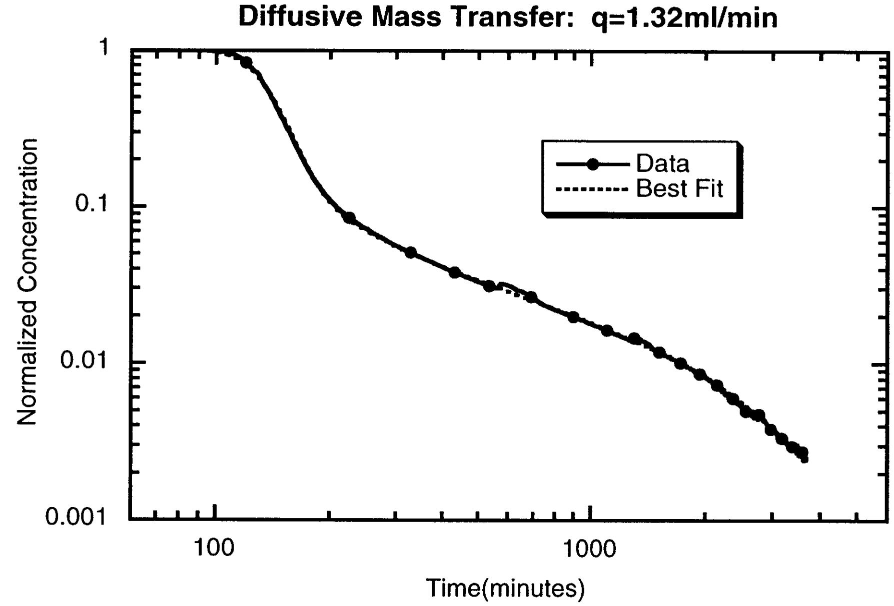

**Figure 4-7:** Diffusive mass transfer experiment breakthrough curve data and best fits. Data set includes more than 1000 points. The model fits both curves with great accuracy. Identical diffusion coefficient estimates indicate that diffusion is the controlling process driving tailing, and β estimates are consistent with expected magnitude.

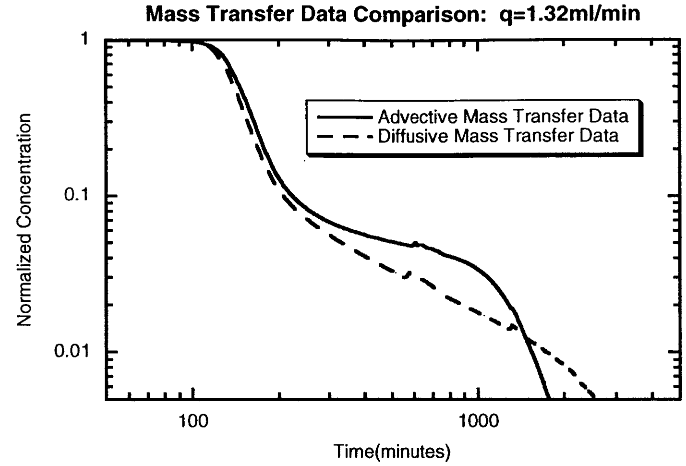

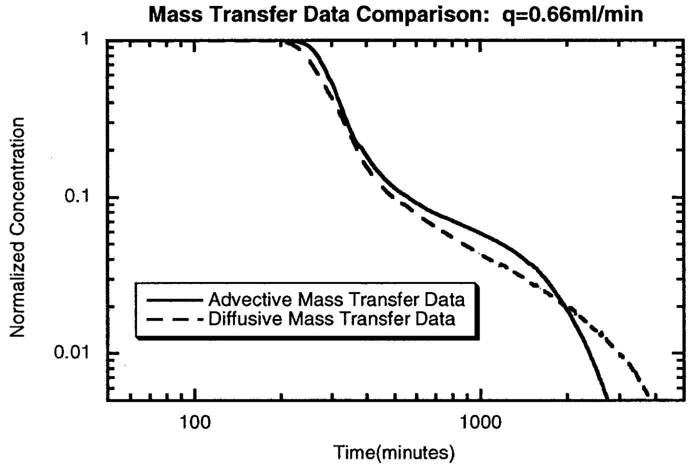

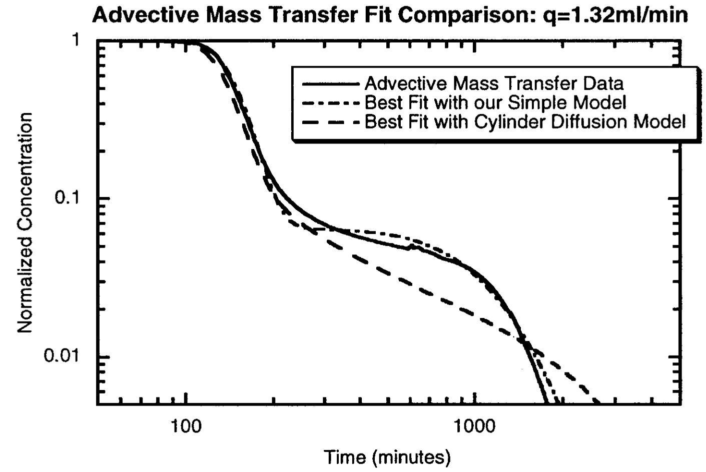

**Figure 4-8:** Advective mass transfer breakthrough curves. The first two figures show the advective mass transfer breakthrough curve as compared to the diffusive mass transfer curve with identical flow rate. In the higher flow rate experiment (q=1.32ml/min), the advective mass transfer case displays significantly different breakthrough characteristics. At the slower flow rate, the advective case tends to look more like the diffusive case (q=0.66ml/min). The third figure shows a comparison of the breakthrough curve for the 1.32ml/min experiment with a fit using our simple model that incorporates advection through cylinders and longitudinal dispersion.

# Chapter 5

# Delineating Different Regimes of Solute Transport

## 5.1 Introduction

The previous chapter demonstrated that a connected field with significant conductivity contrast does show mass transfer behavior, confirming our work from chapter 3. We also were able to demonstrate mass transfer driven by both advection and diffusion, and more importantly, that these two different small-scale processes have a meaningful impact on upscaled behavior. It is also clear from the previous chapter that mass transfer driven by advection and mass transfer driven by diffusion are not necessarily separable processes. It is plausible to have one of the two processes playing a dominant role, but it is also completely plausible for both to simultaneously affect solute transport in a significant way.

In this chapter, we attempt to take the observations and questions raised in the previous chapter, and develop a somewhat more general framework into which the results of our experiments fit. Specifically, we would like to know what conditions cause one or the other mass transfer process to dominate. What effect does the conductivity variability or contrast have? What effect does the hydraulic gradient have? What conductivity contrasts are too small to drive any mass transfer? Do our general answers to these questions seem to fit with our results from the previous chapter? Are our generalizations corroborated by any field data?

We attempt to answer this question by simulating flow and transport through two-dimensional, isotropic random fields, again using a particle tracking approach. This time, we make the field binary, i.e., it only has two conductivity values. These fields are more complex than the cylindrical emplacement fields used in our experiments, which is advantageous to behaviors are possible – diffusive mass transfer, advective mass transfer, or equilibrium mass transfer (which can simply be modeled with Fickian spreading).

Lastly, we compare our results in this chapter with the results from our experiments in the previous chapter, and with results from extensive simulations studying the Livermore aquifer. We find our results to be in good agreement with those results, though, as noted earlier in this work, we often can only compare results in the most general of senses, i.e., is mass transfer occurring, and what process tends to dominate it.

## 5.2 Methods

As with the numerical simulation in chapter 3, we performed particle tracking on a series of random conductivity fields. The fields were created by first generating a lognormal multigaussian conductivity field using the method of sequential gaussian simulation in GSLIB [*Deutch and Journel,* 1997], as in chapter 3. The field was isotropic, two-dimensional, and 800 points horizontally by 500 points vertically.

In creating the binary field from these multigaussian fields, we again exploited the characteristic of multigaussian fields that values closer to the mean are more connected. We took the 50 percent of the multigaussian field with values closest to the mean and assigned a single value to them. The other 50 percent were assigned another value.

The transformed field is shown in figure 1, with black representing one of the conductivity values (the values closest to the mean in the original multigaussian field), white representing the other. The black conductivity values are clearly more connected, forming field-spanning channels, while the white conductivity values form isolated blobs of various geometries. Because of this, we refer to the conductivity of the black area as $K_{channel}$ and of the white area as $K_{blob}$.

We now have an isotropic binary conductivity field with one conductivity more connected than the other, possessing an approximate correlation length ($\lambda$) of 15 blocks. We created multiple conductivity fields by varying the ratio of $K_{channel}$ to $K_{blob}$. Because we are interested in studying relatively high contrasts between the two conductivities, we use a parameter we called $Y_{con}$, which expresses this ratio logarithmically:

$$Y_{con} = \ln\left(\frac{K_{channel}}{K_{blob}}\right) \tag{1}$$

crafting more general conclusions. One could argue, however, that such fields are less complex than those simulated in chapter 3, and that this is perhaps a disadvantage of this approach.

We would argue, though, that overall, a binary field is actually a more realistic description of some aquifers than is the smooth, continuous fields of chapter 3. While those fields are useful in motivating the exceptional importance of connected extreme conductivity structures, it is also worth noting that many aquifers tend not to look so smooth. As noted in the background section of this work (specifically, section 2.1.3), there is ample evidence to suggest that many aquifers are not particularly continuous in nature. The MADE site, for example, appears to consist of basically two conductivities (*Harvey and Gorelick*, 2000). The Livermore site (*LaBolle and Fogg*, 2001) possesses four fundamental facies, but three of these facies are very similar and have conductivities substantially larger than the fourth. The Wilcox aquifer (*Fogg*, 1986) also seems to have a somewhat bimodal distribution of conductivities, driven by two fundamentally different facies. This is not to say that this is true of all aquifers, as there are studies that support the more traditional lognormal distribution of conductivity values (e.g., *Hoeksema and Kitanidis*, 1985). Ultimately, the validity of such assumptions is a function of both the specific aquifer and the scale of interest. However, we think that a binary representation is an accurate approximation for many real scenarios of interest.

Furthermore, the binary nature of the field adds to the power of conclusions, because we can specifically look at what differences in conductivity tend to be conducive to which forms of mass transfer (or even no mass transfer at all). This is something that we simply could not do with a continuous field.

Ultimately, we find that the results in this chapter cannot be summarized simply by words, requiring a figure to fully characterize the results. However, we shall try to briefly summarize the results here. We find that the existence of mass transfer is driven exclusively by conductivity contrast, not by other characteristics like gradient or diffusion coefficient. Once we enter conductivity contrasts where mass transfer begins to occur, things become more complicated. There exist three fundamental time scales that need to be accounted for, as all three are important to describing the solute behavior. The first is the time scale of advection in the mobile domain, i.e., the time to advect through the high conductivity part of the aquifer. The second is the time to advect through low conductivity regions. The third is the time to diffuse into and out of low conductivity regions. Depending on the ratios of these time scales, three

We study a variety of different field values of $Y_{con}$, including cases where its value is negative (i.e., cases where $K_{blob}$ is higher than $K_{channel}$). In all cases, the geometric mean conductivity (i.e., the arithmetic mean of log-conductivity) was kept the same.

Velocities within the field were again calculated using the finite-difference method to the two-dimensional groundwater flow equation, assuming constant head boundaries on the left and right of the field, no-flow boundaries on the top and bottom. The porosity of the field was set to 0.3 everywhere, with a hydraulic gradient of 0.02 and flow moving from left to right, although we eventually non-dimensionalize all of the key parameters, rendering these assumptions unimportant (save the assumption that porosity is constant throughout the field).

Initial particle placement simulated equilibrium saturation. This was done by placing 15,000 evenly spaced particles in a subset of the field, an area of 600 blocks by 400 blocks near the center of the field, in order to eliminate edge effects near the boundaries. Particle breakthrough was recorded along a vertical line that composed the right-hand boundary of the initial saturated area. A saturated initial condition mimics our experimental starting conditions in chapter 4, and allows solute to interact with all areas of the domain, giving us a more complete picture of the subsurface.

Particle simulation incorporated both an advective and diffusive component, using the same method as discussed in chapter 3. Movement was composed of discrete time steps in which advection was explicitly computed through the velocity field, and diffusion was added as a gaussian random step in both the x and y-directions. This method allows curved instead of linear advective steps for the particles, which is essential in allowing particles to flow around sharp block interfaces with large conductivity contrasts while still allowing discrete time steps to incorporate diffusion. For fields such as ours, the capability is obviously essential – traditional interpolation methods with linear advective displacement were found to be incapable of preventing advection into low conductivity areas.

Breakthrough curve parameters were calculated using the one-dimensional, first-order mass transfer model. This model is simple to perform estimation with and does not make assumptions about the process that controls mass transfer (unlike, e.g., cylindrical diffusion). The model (as noted in chapter 3), is expressed as:

$$\frac{\partial c_m}{\partial t} + \beta \frac{\partial c_{im}}{\partial t} = \frac{D}{R_m} \frac{\partial^2 c_m}{\partial x^2} - \frac{v_x}{R_m} \frac{\partial c_m}{\partial x} \tag{2a}$$

$$\frac{\partial c_{im}}{\partial t} = \alpha(c_m - c_{im}) \tag{2b}$$

with the initial condition of:

$$c_m(t = 0) = c_{im}(t = 0) = C_0 \tag{3}$$

i.e., the aquifer is initially saturated at concentration $C_0$. We assume no retardation, i.e., $R_m$ is equal to 1. This leaves four unknown parameters, $v_x$, D, $\alpha$, and $\beta$, to estimate.

We non-dimensionalized our estimates to ease comparison between different fields:

$$v' = \frac{v_x}{v_{mean}} \tag{4a}$$

$$Pe = \frac{D}{v_x \lambda} \tag{4b}$$

$$\alpha' = \frac{\alpha L}{v_{mean}} \tag{4c}$$

With v', Pe (the Peclet number), and $\alpha'$ the normalized velocity, dispersivity, and rate coefficient, respectively, and $v_{mean}$ and L the arithmetic mean velocity and length of the field. $\beta$ is inherently non-dimensional and is the ratio of immobile domain volume to mobile domain volume.

In addition to varying $Y_{con}$ in our simulations, we also varied the parameter we refer to as the normalized diffusion coefficient, defined in similar fashion to the parameter of the same name in chapter 3:

$$d' = \frac{L}{\lambda^2 v_{mean}} d \tag{5}$$

where d is the diffusion coefficient. This non-dimensionalization expresses the average time to advect across the field divided by the average time to diffuse into and out of average-sized $K_{blob}$ regions. For example, a d' value of 1 would indicate that particles tend diffuse in and out of the $K_{blob}$ regions at about the same rate that they advect across the field.

Parameters were estimated using breakthrough curves expressed in the form of total mass fraction remaining in the system using STAMMT-L. Mass fraction curves were chosen because they are much smoother (and thus more reliably fit) than breakthrough curves converted to concentration form. We illustrate the accuracy of fit in figure 2, with curves from simulations in a field with $Y_{con}$ of 6 and d' of 0.01 and 3. These curves and their fits are typical of our results. The d' =0.01 curve shows significant mass transfer, as seen by the tail in the curve, and is fit relatively well with the single-rate model. The d'=3 curve shows no mass transfer, and our model also fits it accurately.

## 5.3 Results

### 5.3.1 Flow Characteristics

Normalization of parameter estimates is essential because flow characteristics change as a function of $Y_{con}$, particularly mean velocity. We illustrate this in figure 3, which shows the effective conductivity of the field as a function of $Y_{con}$, expressed in terms of a value of p. This p value is derived from the formulation for the effective mean of two values (in our case, two conductivities):

$$K_{eff} = \left(\frac{1}{2}\left(K_{channel}^{p} + K_{blob}^{p}\right)\right)^{1/p} \tag{13}$$

where $K_{eff}$ was calculated for each field using Darcy's Law and the volumetric flux and hydraulic gradient. A p value of $-1$ defines the harmonic mean, 0 the geometric mean, and 1 the arithmetic mean.

The general assumption is that an ensemble of conductivities not aligned in layers has an effective conductivity equal to the geometric mean of the ensemble, as discussed earlier. However, figure 3 indicates that $Y_{con} > 0$ creates fields with $p > 0$, i.e., the effective conductivity of the field moves toward the arithmetic mean, and $Y_{con} < 0$ yields an effective conductivity trends toward the harmonic mean. This is consistent with behavior in continuous connected fields seen in chapter 3 of this work – connected high conductivity enhances flow and connected low conductivity channels act as barriers to flow.

As noted earlier, the mean conductivity of all fields was the same, thus mean velocity of a field must increase or decrease as $Y_{con}$ changes. For example, the field with $Y_{con}$ of 8 has a mean velocity of 7.7cm/day, while the field with $Y_{con}$ of 6 has a $v_{mean}$ of 3.1cm/day (assuming mean conductivity of 15.9cm/day, hydraulic gradient of 0.02 and porosity of 0.3). This is one reason estimated parameters were normalized – to increase the ease of comparing results between different fields. It also allows us to express the magnitude of various parameters in comparison to the magnitude of other important field characteristics.

### 5.3.2 Parameter Estimates

Estimation of normalized parameters was performed on the breakthrough curves produced by particle tracking over a range of $Y_{con}$ and d′ values. Simulations were performed on fields with $Y_{con}$ values of 0, ±3, ±4, ±5, ±6, ±7, and ±8. For each field, simulations were run with d′ values of 0.01, 0.03, 0.1, 0.3, 1 and 3.

We found no significant mass transfer when $Y_{con} < 0$. This means values of β were small (none exceeded 0.05), and values of α' are irrelevant. Further, all velocity estimates were found to be within 10% of $v_{mean}$. Only Pe (the normalized dispersivity) showed significant variability when $Y_{con}$ was negative, as shown in figure 4, which maps the Pe estimate as a function of the $Y_{con}$ value of the field and the d' value of the simulation. Dispersivity increases as the contrast in conductivities increases and decreases with increasing diffusion (d'). That dispersivity would increase in more variable conductivity fields agrees with general theory regarding transport in heterogeneous aquifers, but the behavior as a function of d' does not. Most conventional theory treats diffusion as a Fickian process that is added to dispersion. This is not the case in our simulations, although we can be certain that a sufficiently large d' would dominate all spreading in a Fickian manner and thus increase the dispersivity. We discuss this further later, but it should be noted that this behavior bears similarity to results from *Dagan and Fiori* [1997], who worked with pore-scale dispersion modeled in a fashion similar to our diffusion.

When $Y_{con}$ is positive there is significant variation in all four estimated parameters, as shown in figure 5. Both velocity (v') and partition coefficient (β) show similar trends – estimated values are higher at larger values of $Y_{con}$ and lower values of d'. The division of our aquifer into a high (mobile) conductivity half and low (immobile) conductivity half, suggests that in ideal cases (i.e., a situation in which the low conductivity regions are truly immobile) β should be 1 and v' should be 2. In such a situation, we would also predict a strong correlation between the trends of β and v', with 1+β being close to v'. Our results show this behavior, as values of β reach a maximum of about 1, and values of v′ reach about 2, suggesting a situation in which half of the domain is mobile and half is of much lower mobility (provided $Y_{con}$ is high (> 7) and d' is low (< 0.1)).

We can use the β plot to determine where significant rate-limited mass transfer occurs. The cutoff for significance is somewhat arbitrary, but we suggest a β of approximately 0.2, indicating less than 20 percent of the aquifer is contributing to mass transfer behavior, i.e., the tail is relatively small. In fields that display high values of $\beta$ at some values of d' and low values at others, $\beta$ values indicate that the amount of the immobile domain contributing to tailing behavior is decreasing as d′ increases.

Normalized rate coefficients ($\alpha'$) increase with decreasing $Y_{con}$ and increasing d′. Estimates of $\alpha'$ relate mean mass transfer time to mean travel time, so increasing d' increases the speed of movement in these regions, thus increasing $\alpha'$. Decreasing $Y_{con}$ creates higher relative velocities in the low velocity regions, allowing solute to move through immobile regions more quickly and increasing $\alpha'$.

Dispersivity shows the most complex behavior of all parameters. The first, most general observation is that dispersivity tends to increase as $Y_{con}$ increases, consistent with stochasitic theory and qualitatively consistent with dispersivity estimates in our flow visualization experiments. Below $Y_{con}$ of about 4.5, the behavior of the dispersivity is similar to negative $Y_{con}$ cases, but with a much stronger reduction as a function of d'. Above $Y_{con}$ of 4.5 behavior is more complex – dispersivity initially increases, then decreases, and increases again at high d'. This behavior is illustrated in figure 6, which shows Pe estimates for the field with $Y_{con}$=6, carried out to larger d' than shown in figure 5. The behavior past d' of 45 is speculative, indicated by the dashed line with the question mark. Dispersivity estimates increase up to a d' value of about 10, then sharply decrease out to d' of 30, and then begin increasing again. This complicated dispersivity behavior, as with the negative $Y_{con}$ cases, is contrary to general theory on coupling of dispersion and diffusion. We speculate on what drives this behavior in the following section.

Lastly, we compared the relative influence of diffusive and advective processes in the mass transfer behavior observed by comparing parameter estimates, using a technique similar to the one we used in chapter 3. We reran simulations with the hydraulic gradient (and thus velocity) reduced to half of its original value. Using the same diffusion coefficients as the original case, we reran the particle tracking simulations and estimated breakthrough curve parameters, with particular attention to the new estimates for $\alpha'$, which we call $\alpha'_2$. We show in figure 7 the ratio of $\alpha'$ to $\alpha'_2$ as a function of $Y_{con}$ and the mean d'. The mean normalized diffusion coefficient is used because changing the hydraulic gradient by a factor of 2 also scales the normalization factor (see equation 5).

If advection was the only process driving mass transfer, then values of the ratio of $\alpha'$ should be 2, since mass transfer will occur twice as fast when the velocity is twice as high. If diffusion exclusively drove mass transfer, the estimate of $\alpha'$ should be identical in both cases, i.e., the $\alpha'$ ratio should be 1. Figure 7 shows an $\alpha'$ ratio closest to 2 at $Y_{con}$ between 5 and 7 and relatively low d' values, while higher values of $Y_{con}$ and d' drive the ratio in the direction of diffusive mass transfer. We hypothesize why this occurs in the discussion section that follows. The separation between primarily diffusive mass transfer and primarily advective mass transfer is somewhat arbitrary. Wherever the line is drawn, it is clear that there is a significant area in which neither process completely dominates the tailing behavior, and therefore both processes play a significant role.

## 5.4 Discussion

In a broad sense, our simulations identified two fundamentally different types of binary conductivity fields – ones with solute transport described by mass transfer models, and ones without. However, we can break these into qualitatively described behavioral subcategories, summarizing the complete results in figure 8, which shows a qualitative description of the behaviors as a function of $Y_{con}$ and normalized diffusion coefficient. The figure also notes where our experiments in chapter 4 would occur with this system of demarcation – $Y_{con}$ computed by the estimated conductivity difference inside and outside the emplacements, d' by the characteristic time to diffuse out of an emplacment (given the radius and estimated diffusion coefficient) compared with the mean velocity of the field (estimated velocity of the mobile domain divided by $1+\beta$).

When $Y_{con}$ is less than 0, channels of low conductivity impede flow, leading to a lower effective conductivity for the field. These low K areas are rarely isolated from flow, which prevents conditions that lead to tailing. Heterogeneity in the flow field leads to dispersion that increases as the conductivity contrast increases, but the addition of diffusion averages out velocity variability experienced by the solute, decreasing dispersivity.

When $Y_{con}$ is between 0 and approximately 4.5, channels of high conductivity promote flow around low K areas, but the conductivity contrast is not sufficient to create immobile regions. Heterogeneity promotes some degree of tortuous flow around low K areas, so dispersivity is higher than in the negative $Y_{con}$ fields of equal variance. Additional diffusion reduces dispersion, for similar reasons to negative $Y_{con}$ case, but reduces it by a larger amount.

When $Y_{con}$ exceeds 4.5, fields have a conductivity contrast high enough to create isolated low velocity zones with much slower flow than the high conductivity channels. Tailing can occur by two processes – slow advection through the low velocity regions, or diffusion into and out of them. The time scale of both processes is affected by the geometry of the low K regions, but the two processes differ in other controlling factors. In addition to geometry, diffusion-driven mass transfer is controlled by the diffusion coefficient, while advection-driven mass transfer is controlled by the hydraulic gradient and the conductivity of the region (or more accurately, the conductivity ratio between the high and low areas). The process that occurs most quickly dominates the tailing, though it is possible for both processes to occur at similar rates. This explains the observation that increasing $Y_{con}$ and d' increases dominance by diffusive mass transfer – increasing d' speeds up diffusion while increasing $Y_{con}$ reduces the relative conductivity of isolated areas, thus decreasing the advective velocity in these regions.

Also, $\beta$ tends to decrease from it's maximum possible value (in our case, 1) as $Y_{con}$ decreases and d' increases. This is a result of the varying geometry of the low conductivity regions. The time scale to diffuse or advect into and out of some regions is shorter than others. When $Y_{con}$ decreases, the relative time to advect through these regions decreases. Increasing d' decreases the time to diffuse. Low conductivity areas with short time scales of advection or diffusion will not contribute to significant tailing, as solute is not slowed down sufficiently in these regions. Eventually almost all of the advective and diffusive time scales are too fast to drive tailing, and thus we leave the regime of solute transport that is best described by the mass transfer model. In fact, during transport in these scenarios, most solute spends approximately equal amounts of time in mobile and immobile regions, behavior described by classic equilibrium mass transfer with retardation factor equal to $1+\beta$. However, from a model standpoint, this behavior can be described completely with Fickian spreading, and thus we do not require the use of a mass transfer model.

Dispersivity behavior in fields with significant mass transfer is quite complex. Initially, dispersivity increases with d', then begins to decrease once d' reaches about 3, then begins increasing again once d' reaches 30. This runs counter to the usual method of incorporating diffusion into upscaled models of solute transport, in which diffusion and dispersion coefficients are added to each other to get the effective Fickian spread. We think that the dispersivity behavior in our fields results from solute that quickly moves in and out of immobile regions becoming incorporated into the dispersivity estimate, i.e., quick mass transfer introduces additional spreading that looks like dispersion. As d' increases, the amount of solute that falls into this category increases, until we reach a point where only equilibrium mass transfer occurs. At this point, we see behavior similar to that observed in the lower $Y_{con}$ fields – added diffusion reduces dispersion by evening out velocity variability. Finally, once d' becomes very large, diffusion acts as a Fickian spread (equilibrium mass transfer conditions are maintained) but is so large that it dominates spreading and exceeds spreading driven by velocity variability. Presumably, this increase continues indefinitely in an approximately linear fashion. How realistic scenarios with such large d' are in the real world is probably questionable.

This points to a key feature of our simulation results – use of non-dimensional parameters. It is possible to extend our results to a variety of different aquifer scenarios, provided that the aquifer is approximately binary in its conductivity distribution and one of the conductivities is significantly more connected than the other. For example, we can compare our results to those from the Livermore site simulations, as detailed in *Labolle and Fogg* [2001]. Although the site has four facies, three have relatively similar hydraulic conductivities, much higher than the fourth. The highest conductivity is the most connected, the lowest (which takes up about 56% of the volume) is the least, with values that lead to a $Y_{con}$ of approximately 10.5. Using the geometry of the low K regions, the regional head gradient, porosity, the diffusion coefficient of the contaminants, and the simulated travel distance, we estimate a d' value of 0.2. Labolle and Fogg find extensive tailing driven by diffusion, as well as the fraction of mass entering low K regions showing a strong dependence on the diffusion coefficient value. This behavior is precisely what our simulations would predict, despite the fact that this field site is not perfectly analogous to our simulations. Although our model can predict general behavior, it does not predict the precise appearance of breakthrough curves, which are dependent on the specifics of the site in question.

The caveat with non-dimensionalization is that it does not require that the transport scenario be realistic. High values of d' (i.e., greater than 1) require very small immobile regions, very slow advective flow rates, or very large travel distances. Also, if the aquifer possesses a structure such that $K_{channels} > K_{blobs}$, but with strong anisotropy perpendicular to the direction of flow, the field may not be described by our model (see *Guswa and Freyberg* [2002] for examples of such fields).

Our parameter estimates are partially dependent on initial conditions, but we would not see fundamentally different behavior with different solute starting conditions. For example, consider our field with $Y_{con}$ of 8, but with particles all starting in the mobile domain (such as a flux-proportional line injection). At low d' values, few particles would enter low conductivity regions, so we would observe breakthrough curve tails that were small in overall volume but lengthy due to the slow rate. Moderate diffusion values would cause faster diffusion into low K areas, resulting in faster rate coefficients and larger tails. Finally, large d' values would result in equilibrium mass transfer, just as occurred with our initial conditions. This does not reflect fundamentally different behavior driven by the two initial conditions, but they clearly could alter the overall spatial and temporal profiles of the plume.

Figure 8 demonstrates that our visualization experiments in chapter 4 agree well with our numerical results. The advective-dispersive tank has a conductivity contrast that our simulation results predict will lead to advective-dispersive behavior, although it is difficult to conclude that dispersivity is reduced at higher diffusion coefficient, because we question the accuracy of one of the dispersivity measurements. The diffusive mass transfer tank also falls in a conductivity contrast and diffusion coefficient values that predict mass transfer dominated by diffusion. The advective mass transfer tank is a bit more complicated – our results in chapter 4 suggested that the faster flow experiment was advection-dominated mass transfer, but the slower of the two experiments might be somewhere between the advection-dominated and diffusion-dominated cases. However, figure 8 agrees reasonably well with this result – the location of the slower experiment puts it somewhere near the boundary between diffusive and advective mass transfer.

Lastly, we have included, for the sake of completeness, a final regime of solute transport that occurs when the normalized diffusion coefficient is very large. Although we did not explicitly simulate any such scenarios, it is reasonable to assume that once the normalized diffusion coefficient becomes extremely large, diffusion dominates solute transport. This means that almost all spreading will be due to diffusion (a Fickian spread). The realism of such scenarios is questionable, though, as noted earlier in this section, requiring extremely low flow rates, which are unlikely to occur in most real-world aquifers. Some exceptions might be flow through low conductivity barriers (such as in a waste containment lining) or in fracture networks where the fractures are not sufficiently connected to allow for significant advection.

## 5.5 Conclusions

In this chapter, we extended the results of the experiments detailed in chapter 4 into a more general framework using particle tracking simulations in a random connected binary conductivity field. Results from these simulations were in strong agreement with our experimental results. Two main behaviors were observed – traditional advection-dispersion, mass transfer behavior (i.e., tailing) driven by varying degrees of advection and diffusion. Within the advective-dispersive regime, there is a further subdivision – in fields with $Y_{con} > 0$, dispersion is strongly reduced by increasing diffusion, while in negative $Y_{con}$ fields, dispersion is more moderately reduced by increased diffusion. In both cases, this goes against the conventional method of treating diffusion and dispersion coefficients as additive.

The division between advective and diffusive mass transfer is not a hard boundary, rather a continuum which moves from dominance of mass transfer by one process to dominance by the other. The particular details of the transition and importance of the two mass transfer processes is determined by the time scale of advection through low conductivity regions and the time scale of diffusion through these regions. Both time scales are dependent on the geometry of the low conductivity regions, but diffusive rates will depend on the diffusion coefficient while advective rates will depend on the hydraulic gradient and conductivity.

This means that tailing in these aquifers depend on certain aquifer characteristics that are generally not accounted for, and that changes in these characteristics can significantly affect the behavior of solute transport and mass transfer. Also, some of the parameters, such as the hydraulic gradient, are to some degree controllable, thus making the competition between mass transfer processes an important consideration in remediation decisions. It is this competition that we consider in the final section of the work.

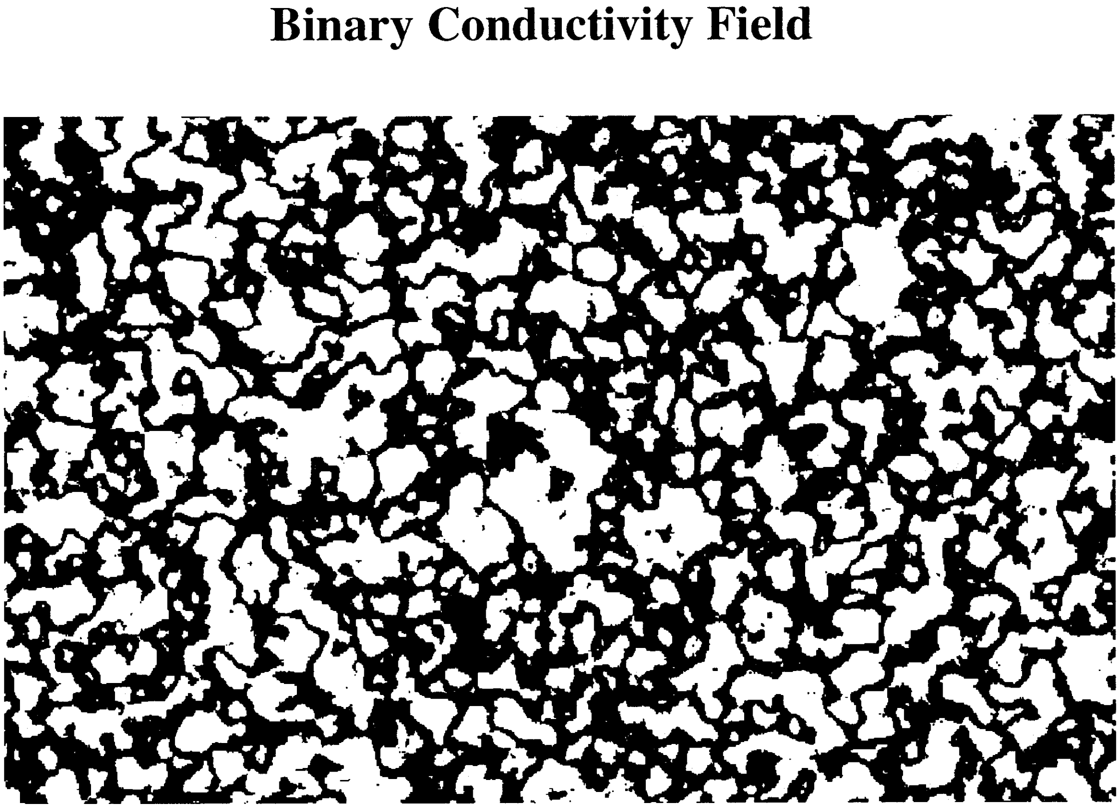

**Figure 5-1:** Illustration of binary conductivity field. All black locations have one value, all white locations have one (different) value. Black areas are the most connected, forming thin channels that span the conductivity field. White areas tend to form isolated blobs.

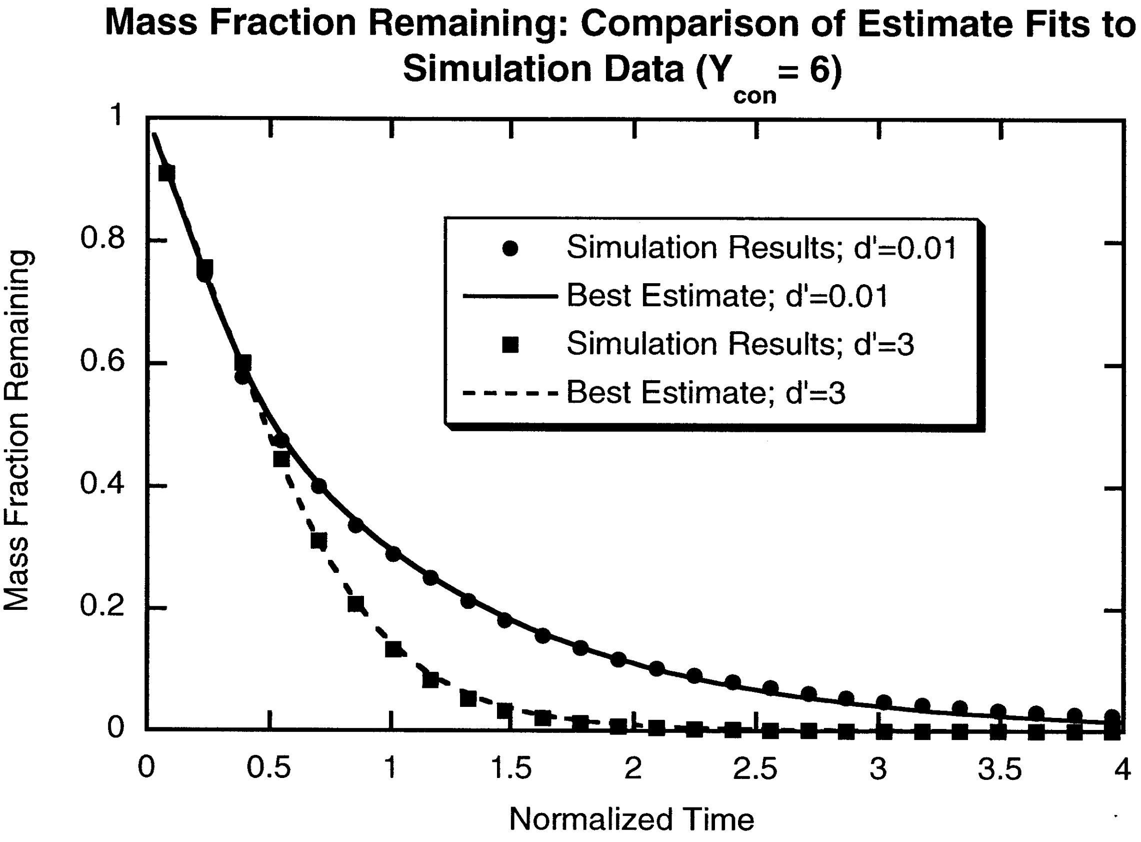

**Figure 5-2:** Sample breakthrough curves shown in form of mass fraction remaining, plotted with best estimates using single-rate mass transfer model. The model provides good fits both in a case with mass transfer (d'=0.01) and a case without mass transfer (d'=3).

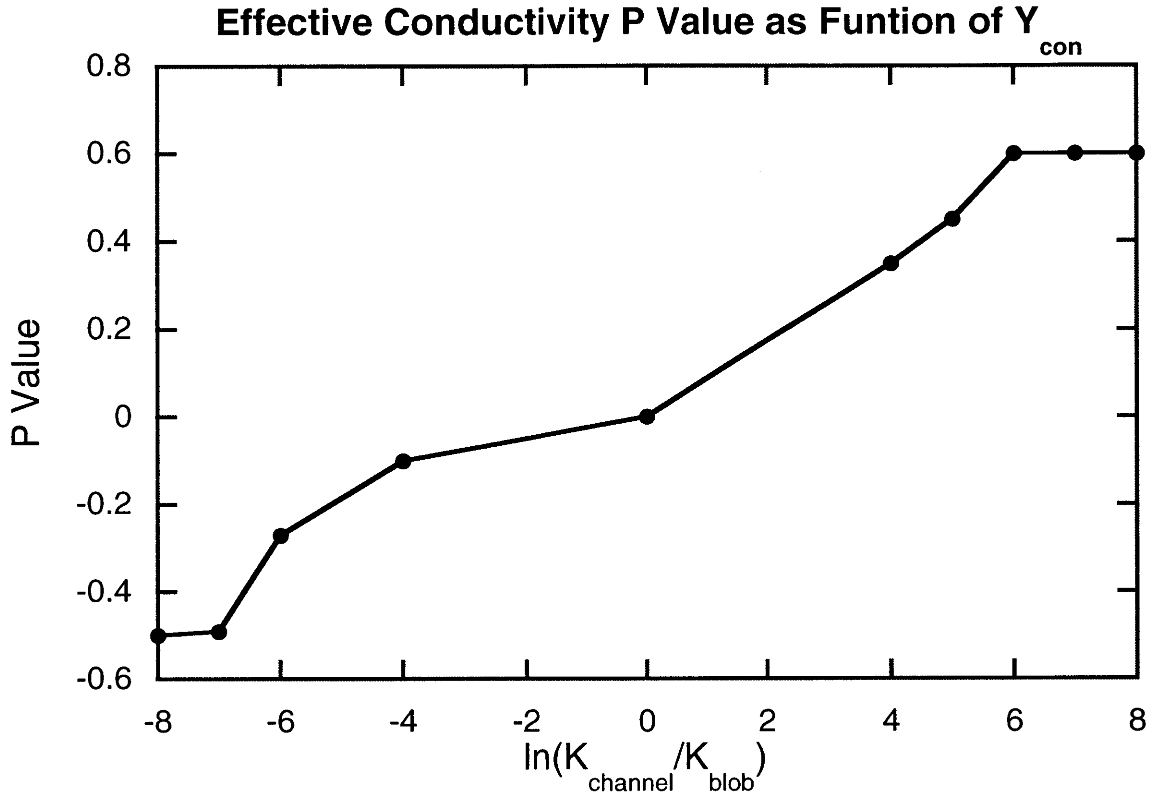

**Figure 5-3:** Effective conductivity of field expressed in form of p-value. Positive p-value indicates bias in effective conductivity toward the arithmetic mean, negative indicates bias toward the harmonic mean. Non-layered fields are usually assumed to have an effective conductivity equal to the geometric mean (p-value of 0).

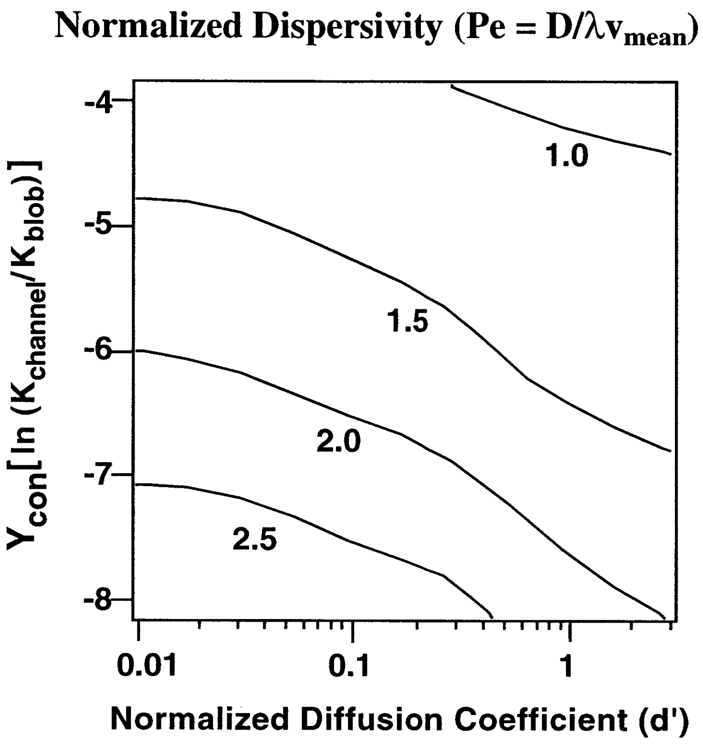

**Figure 5-4:** Estimated normalized dispersivities for fields with negative $Y_{con}$. Dispersivity tends to increase with increasing contrast between channel and blob conductivity, and also increases as normalized diffusion coefficient increases, counter to conventional methods of incorporating diffusion

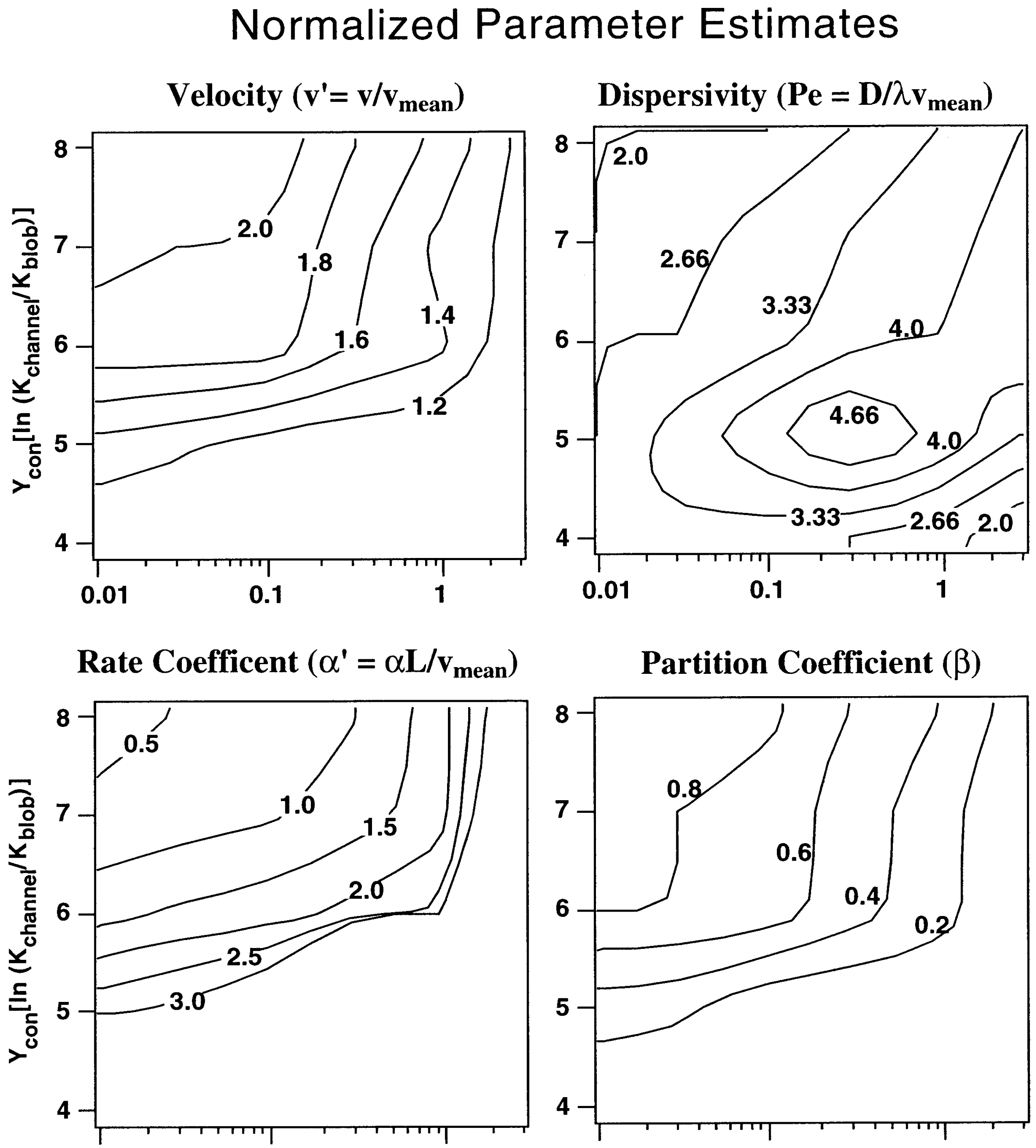

**Figure 5-5:** Normalized estimated parameters for fields with positive $Y_{con}$. Dispersivity shows complex behavior similar to negative $Y_{con}$ case. Rate coefficients (α') increase as diffusion increases and conductivity contrast decreases. Large estimates of β indicate significant regions of mass transfer, supported by estimates of v' that approach 2. Low β estimates and v' estimates of 1 for high $Y_{con}$, high d' cases suggest equilibrium mass transfer.

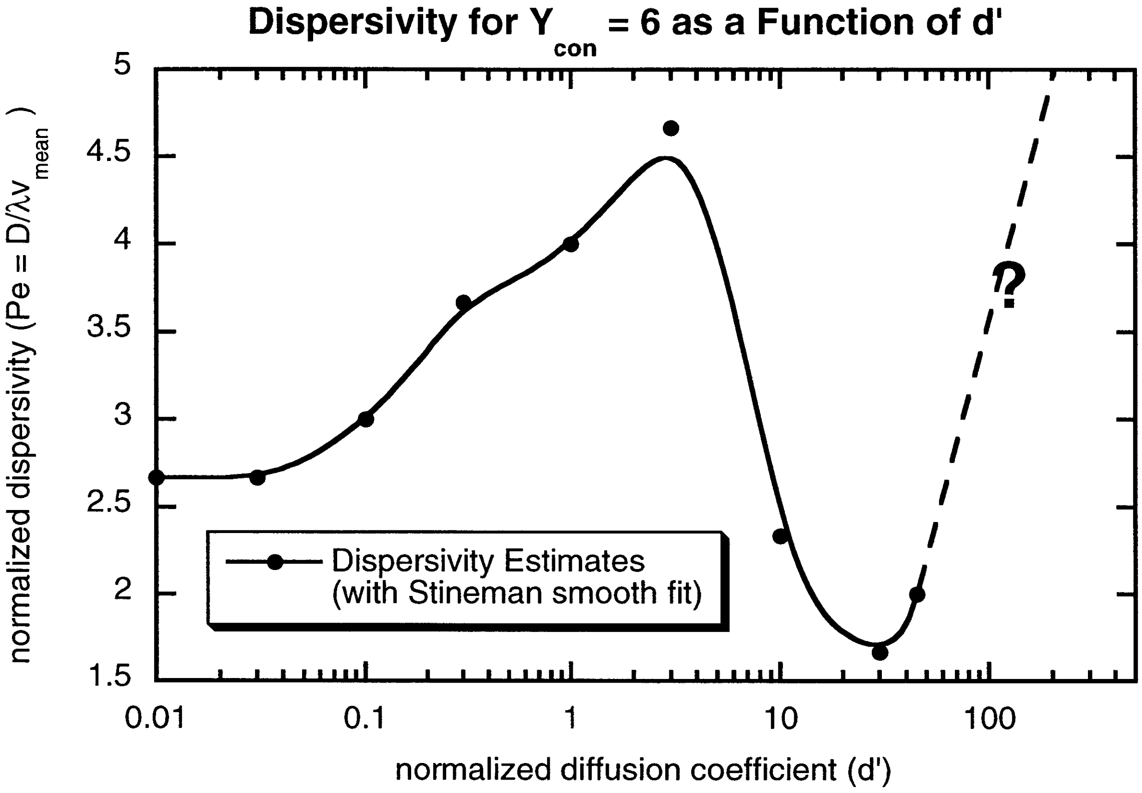

**Figure 5-6:** Dispersivity as a function of normalized diffusion coefficient for field with $Y_{con}$ of 6. Dispersivity shows a complex behavior of rising, falling, and then rising again. The dashed line with question mark is speculative, and the curve is a smoothed fit to the data (shown as black dots).

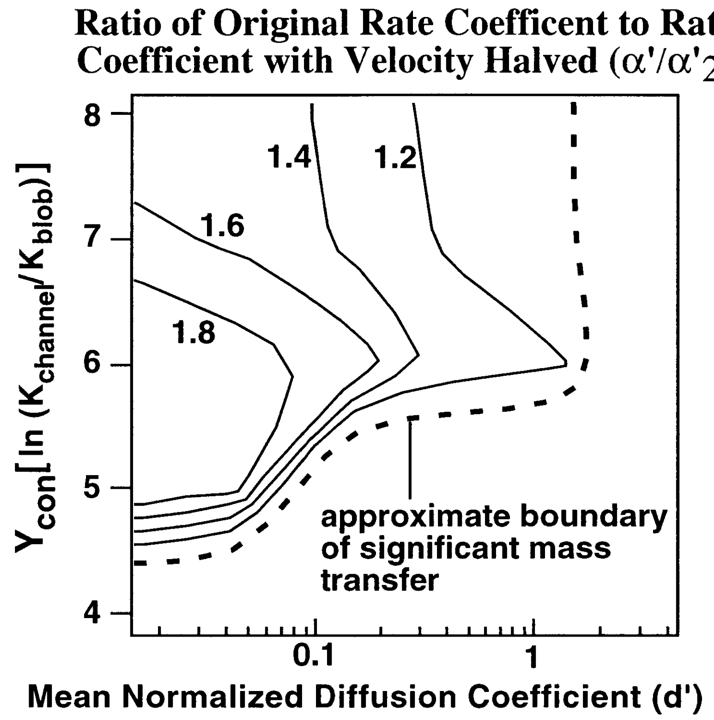

**Figure 5-7:** Comparison of α' estimates in original case divided by α' estimates in case where velocity has been reduced by a factor of 2 but diffusion coefficient stays the same. A ratio close to 2 indicates that advection is the dominant mass transfer process, a ratio close to one indicates that diffusion is dominant. The x-axis is shown as the mean d' value of the two runs, since keeping diffusion coefficient constant but varying velocity changes d'.

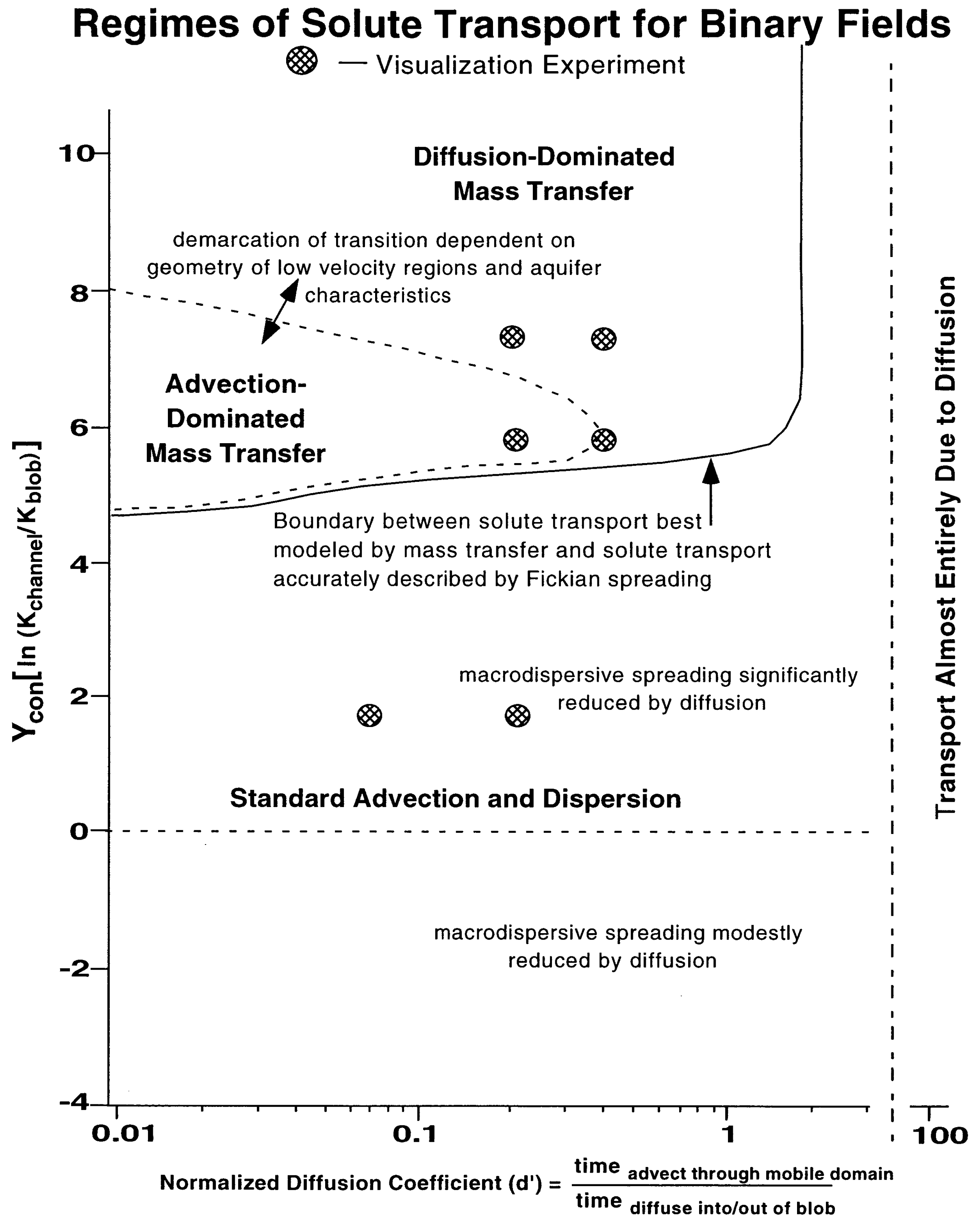

**Figure 8:** Figure mapping out regimes of transport and conditions under which they occur. Location of experiments relative to our scales of $Y_{con}$ and d' are marked as well. The transition between advective and diffusive mass transfer is dependent on several aquifer and solute parameters, and thus is not a concrete line – the one shown is appropriate for our particular case. Although not explicitly modeled in our simulations, at high values of d' transport is dominated by diffusion.

# Chapter 6

# Implications of Multiple Mass Transfer Processes and an Application

## 6.1 Introduction

Most of our work thus far, particularly in the previous chapter, focused on trying to determine conditions under which either advective or diffusive processes dominated mass transfer. In this sense, we have tended to treat the two processes separately, but in this chapter we try to examine the behavior of solute tails when both mass transfer processes operate jointly, in particular the effect on rates of mass transfer. We also change the perspective from which we look at the plume tails – our earlier work has frequently described behaviors in terms of a normalized diffusion coefficient, with the diffusion coefficient assumed to have changed and the gradient assumed to have stayed constant. Now we examine these tails from the perspective of a changing head gradient and constant diffusion coefficient, on the assumption that head gradients tend to be a more controllable parameter in the real world.

We also try to steer ourselves away from the dependence on effective parameters that we have displayed in the earlier sections of this work. Although such parameters can be useful for simple characterization, we try to take an approach in this section of "looking at the tail", instead of fitting models to it, though we do resort to that methodology in a few instances. This approach allows us to study the memory function, g(t), of the solute transport (see section 2.3.2). We examine what effect the presence of advective mass transfer means for g(t), since it is generally assumed to be a fixed parameter of the aquifer. We also study whether assumptions about the memory function model, particularly equation 13 in chapter 2, remains valid in the presence of advective mass transfer.

Finally, we bring the work back to an application that gets at the original motivation of the research – the effect of mass transfer on remediation. As noted in the introduction, tailing is a potentially huge problem in remediation, and our work has focused on identifying conditions that promote nonequilibrium behavior. However, with the presence of advective mass transfer, we are faced with a mass transfer process that we have some degree of control of, by controlling head gradients through pumping rates. We are also potentially faced with a process over which we have no control, diffusive mass transfer. Is increasing pumping rates a desirable alternative in the presence of advective mass transfer? We suggest that it is a somewhat complicated tradeoff of costs, but there are potentially optimal decisions between extremely fast or extremely slow pumping rates.

## 6.2 Methods

Our analysis in this chapter mainly makes use of results from previous sections, with examination of these results from a different perspective. However, we did augment these results with some additional particle tracking simulations.

Although our goal is to study joint advective and diffusive mass transfer, we must, for comparison's sake, also determine solute behavior in the presence of only one of the two processes. To study the case of advection-only mass transfer, we ran simulations on the binary fields with $Y_{con}$ of 6 and 8. We chose these two particular fields because both show significant mass transfer, but the field with $Y_{con}$ of 6 tended to be far more conducive to advective mass transfer. For these new simulations, we simply deactivated diffusion, i.e., we only simulated advection. All other characteristics – head gradient, initial conditions, etc., were kept the same. In order to study the case of diffusion-only mass transfer, we generated a binary field with a $Y_{con}$ of 15. Such a field has extremely low velocities in the low conductivity areas, such that any significant value of diffusion coefficient will ensure that mass transfer is entirely diffusion-driven. We ran simulations in this field for the same range of diffusion coefficients as run in the binary fields in chapter 5.

Because we wish to express our results in terms of solute transport components that can be externally influenced, we express our most of our results in this section as a function of normalized hydraulic gradient. The gradient is defined as being equal to one when it drives a characteristic time of diffusion that is equal to the characteristic time of advection in the mobile domain, i.e., the gradient at which the normalized diffusion coefficient is one. Higher normalized gradients are analogous to reducing the normalized diffusion coefficient by an equal ratio.

Lastly, we also want to study different initial conditions in this chapter. To do this, we introduced approximately 2000 particles in a flux-proportional line into the $Y_{con}$ 6 and 8 binary fields, similar to what was done in the continuous connected fields in chapter 3. Breakthrough was recorded at a line 40 correlation lengths from the initial injection line (i.e., transport occurred through the same total area as in the equilibrium scenarios in chapter 5), with all other characteristics of the field and the simulations the same as their corresponding equilibrium simulations. We also performed these flux-proportional simulations for advection-only scenarios in the $Y_{con}$ 6 and 8 fields and ran simulations in the field with $Y_{con}$ of 15 to study diffusion-only mass transfer.

## 6.3 Results

### 6.3.1 The Memory Function – g(t) and g*(t)

As noted in the background section, the late-time concentration of a solute plume can be expressed in relation to the memory function through:

$$C \cong t_{ad}\left(C_0 g - m_0 \frac{\partial g}{\partial t}\right), \qquad t >> t_{ad} \tag{1}$$

with $C_0$ as the initial concentration of solute in the immobile domain and $m_0$ the mass of solute injected at time 0. This leaves us with a relatively simple method of determining g(t) for the binary fields. In the simulations that were run in chapter 5, we began with the entire aquifer initially saturated, and then flushed the aquifer with clean water, meaning $m_0$ is zero, and we can rewrite equation 1 to calculate g(t):

$$g(t) = \frac{C}{C_0 t_{ad}} \tag{2}$$

i.e., g(t) is basically just the late-time concentration of the initially saturated initial conditions (give or take a couple of constants).

In figure 1 we show the memory function of the two binary fields ($Y_{con}$ of 6 and 8), each for three different normalized gradient values, as a function of normalized time. Time is normalized by a different amount for each gradient, because changes in gradient change the mean velocity of the field. The main observation we can make from these graphs is that the total "area" under the curves, i.e., the amount of mass transfer, is clearly gradient dependent. This seems to be especially true in the field with $Y_{con}$ of 6, where substantially less mass transfer occurs at lower gradients (i.e., smaller velocities). This reduction of mass transfer at lower gradients is also present in the $Y_{con}$ of 8 field but to a lesser extent.

In order to examine the rates of mass transfer, we show in figure 2 these same memory functions, but divided by $\beta_{tot}$ (or, since we have used single-rate mass transfer fits, just $\beta$). This formulation, which we refer to as $g^*(t)$, allows us to look at the rates of mass transfer without getting caught up in differences that might just be a product of smaller immobile domain volume. If g(t) is a purely diffusive process, and therefore unaffected by changes in the advective characteristics of the field, then the rate of mass transfer, i.e., the late-time slope of g(t), should also remain constant. This requires that in normalized time, it should scale in an inverse linear fashion with the gradient. Although there is some inverse scaling, it is clearly not as large as the changes in hydraulic gradient (i.e., a factor of 100). This result and the fact that the amount of mass transfer depends on hydraulic gradient both suggest that part of the mass transfer in these fields is being driven by advection. These are unsurprising results given our earlier work, but with important implications, as we discuss in the next section. In particular, these run counter to the conventional assumption that g(t) is simply an aquifer parameter unaffected by external forcing.

### 6.3.2 Joint Mass Transfer Processes Compared to Individual Processes

Our work thus far has generally focused on transport scenarios in which both advective and diffusive mass transfer occur, but it is interesting to ask what the product of the two processes looks like as compared to each process individually. We motivate this in figure 3, a plot of the memory function (g(t)) for the binary field with $Y_{con}$ equal to 6 and a normalized gradient of 3. This is compared to g(t) for the cases of diffusion-only mass transfer and advection-only mass transfer (calculated as detailed in section 6.2). Although the advection-only and diffusion-only cases appear to have similar slopes, this is not something that is generally true, it just coincidentally happens to be the case in this particular field with this particular combination of parameters. The slope of the joint (i.e., advective and diffusive mass transfer) case is clearly significantly steeper than either individual case. This behavior is consistent throughout our results in the fields with $Y_{con}$ of 6 and 8 – the presence of both advection and diffusion increases the speed of mass transfer as compared to either process operating alone.

Although figure 3 provides a good specific illustration, can generalize the results by looking at the slopes of g(t) for the three cases (diffusion-only, advection-only, and both diffusive and advective mass transfer) over a range of gradients. Using the slope is a reasonable method of characterizing g(t) provided that the memory function is approximately (logarithmically) linear, which it was for our simulations. Figure 4 shows these g(t) slopes for both binary fields. The x-axis on each graph shows the normalized hydraulic gradient, the y-axis indicates the (absolute value of the) slope.

The solid line in each graph shows the slope of g(t) (normalized in time, i.e., $\Delta g$ divided by $\Delta$(normalized)time) as a function of hydraulic gradient for simulations in which both advective and diffusive mass transfer occurs. One dotted line shows the slopes in the case of diffusion-only mass transfer. The other dotted line shows the sum of the slopes of the diffusion-only and advection-only cases. Note that the slope of the advection-only case is the same regardless of hydraulic gradient, since the slope calculation uses normalized time, which scales as a function of the gradient.

As we saw in figure 3, the slopes of the joint cases are consistently larger than in either case alone. In fact, the joint slope generally tends to be at least equal to the sum of both processes individually. This suggests that, at least for our binary fields, that the two processes, advective and diffusive mass transfer, tend to be approximately additive processes. Furthermore, at high hydraulic gradient, the slope of the joint case is actually greater than the sum of the two cases individually, suggesting that the two mass transfer processes are actually enhancing each other. We speculate on why this occurs in the discussion section.

### 6.3.3 Validity of g(t) Formulation in Presence of Advective Mass Transfer

Going back to equation 1, we see that knowing g(t) allows us to predict late-time concentrations relatively easily for two simple scenarios. The first case is one in which the immobile domain begins with equilibrium saturation of solute and is flushed with clean water (and thus $m_0$ is zero). The second is one in which the immobile domain begins clean (thus $C_0$ is zero) and we add a dirac-input of solute to the aquifer. We have used the first case to calculate g(t), as seen in figure 1. With g(t), we should be able to predict the late-time concentration of a dirac-input, i.e., the late-time breakthrough curve of our simulations in which we introduced a flux-proportional line source into a clean aquifer. Using equation 1, the prediction is:

$$C_{late} = -m_0 \frac{\partial g}{\partial t} t_{ad} \tag{3}$$

Where g(t) is already known, from figure 1. Thus knowing g(t) for a particular hydraulic gradient, we should be able to predict the late-time concentration of our flux-proportional case using equation 3. Figure 5 shows just such a prediction, for the binary field with $Y_{con}$ equal to 6 and a normalized gradient of 3. In this case, the memory function method seems to be a relatively good prediction of late-time concentration. This effectiveness of the prediction method tends to be consistent for both fields over a range of hydraulic gradients, with results similar to the first graph in figure 5. To check to see if this prediction method was effective even in the total absence of diffusive mass transfer, we compared our simulation of dirac-input into the field with $Y_{con}$ of 6 and no diffusion to a prediction using equation 3. Again, agreement between the prediction and actual late-time breakthrough is quite good.

## 6.4 Discussion

Perhaps the most important result from the this section is that g(t) is a clearly a process with some functional dependence on the hydraulic gradient. This is in contrast to the usual assumption that g(t) is a inherent (and fixed) property of the aquifer. This is not to say that g(t) is purely dependent on external forces – clearly aquifer properties matter, as can be seen in figure 1, in which the two fields with different $Y_{con}$ show somewhat different behaviors. That g(t) has a component dependent on the hydraulic gradient is not particularly surprising given our earlier work that demonstrates the potential for an advective component of mass transfer. But it is worth emphasizing again that this dependence of an aquifer's mass transfer properties on external forces has important implications, as we demonstrate in the following section.

Another interesting observation is that the $Y_{con}$ of 6 field shows less change as a function of hydraulic gradient than does the field with $Y_{con}$ of 8, as seen in figures 1 and 2. Since we use normalized time, a mass transfer process that is entirely advection-driven should look identical regardless of pumping rate (as a function of normalized time). Figures 1 and 2 confirm our results from chapter 5 that the $Y_{con}$ of 6 field is more conducive to advection-dominated mass transfer, as demonstrated by its smaller variation as a function of hydraulic gradient. This confirms the results of chapter 5 in a general sense, without requiring reliance on effective parameters.

Perhaps the most surprising result is the effectiveness of the memory function method in predicting solute concentrations when initial conditions are changed, at least in the case of our binary fields. This effectiveness seems to hold even for cases when mass transfer is purely advective despite the fact that, as mentioned, g(t) is not explicitly formulated to account for this behavior. This implies that only a minor modification of the memory function model may be necessary to account for advective mass transfer processes.

The additive nature of the slopes of g(t) (figure 4) suggests that in our binary fields, advective and diffusive mass transfer processes tend to both enhance the rate of mass transfer, leading to a faster overall process (i.e., a sharper slope). This additive nature makes for convenient formulation of mass transfer in these fields, where the effective rate of mass transfer is in many cases a simple linear combination of the two processes individually, and in certainly is generally bounded by the sum of rates of the two processes.

As noted, the most interesting behavior of the late-time slopes (figure 4) is seen in the field with $Y_{con}$ of 8 with relatively large hydraulic gradient. In this case, the rate of mass transfer is actually significantly larger than the sum of the two processes individually. We hypothesize that this occurs because the low-velocity domain contains a range of advective paths with varying residence times. If we imagine that the low-velocity regions begin saturated with solute, advection can mobilize that solute quickly from the fastest paths, effectively "cleaning out" these areas. Solute from adjacent slower paths can then diffuse into these clean faster paths. In this way, overall mass transfer is sped up by solute preferentially diffusing into faster paths. We think this is what is responsible for this accelerated behavior, and we can see some evidence of it in figure 4. If our explanation is correct, then presumably if diffusion becomes extremely small relative to advection, the process described above will cease to function, because solute does not have time to diffuse into the faster advective paths. In figure 4, we see that this behavior (in the $Y_{con}$ of 8 field) peaks at a normalized gradient of 30 and then begins to decrease. This is consistent with the idea that once the gradient becomes extremely large, the speed of diffusion begins to become too slow to drive the accelerated mass transfer behavior.

It is important to note that although the rate of mass transfer in the binary fields tends to be additive, the same is not true regarding the "size" of the mass transfer (i.e., the total mass contained in the solute tail). While advective and diffusive mass transfer processes are fundamentally different, both operate on the same "area", those regions in which velocities are significantly lower than the mobile domain. Depending on various inherent properties of the aquifer and certain external conditions, some areas may be more amenable to mass transfer by diffusion or by advection. However, the total size of the areas possessing fundamentally slow velocities relative to the mobile domain will not change.

One last caveat is that our conclusions, particularly regarding late-time slopes of breaktrough curves, while applicable to our binary fields, are not necessarily applicable to all mass transfer scenarios. As an example, consider the case of our experiments in chapter 4 on the advective mass transfer tank. We show g(t) for these cases in figure 6 (without normalized time). The diffusion-only case we know from analytic models (and from our results in the diffusive mass transfer tank), and the advection-only case is just generated by applying the model in Appendix B with longitudinal dispersion/diffusion set to zero. In this case, where the tail is more complex than the approximately linear tails of the binary fields, the behavior with both advection and diffusion present is clearly not some simple linear combination of the two processes. This is probably due to the fact that in the cylindrical emplacements, the areas of fastest diffusive mass transfer and the areas of fastest advective mass transfer are not necessarily the same. For example, diffusive mass transfer is fastest along the edges of the cylinder, but some of those upstream edges are the longest advective mass transfer pathways. This points to the fact that our results are not necessarily appropriate for all mass transfer scenarios, especially given the complexity of the behaviors that can occur. That said, figure 6 does again point to the fact that g(t) can be dependent on the hydraulic gradient, contrary to the usual assumptions.

## 6.5 Applying Dual Mass Transfer Processes to Remediation

It is reasonable to ask, after viewing all of the research detailed thus far, why the topics we have studied in this research are actually important. We have noted in the introduction that tailing is an important factor in determining the cost of remediation at a site, both due to increasing the time it takes to remediate the site, and due to the greater marginal cost of treating water with low solute concentration present in tails. We would like to close our work with an example that will hopefully motivate the importance of accounting for both diffusive and advective mass transfer in a remediation strategy.

### 6.5.1 The Problem

We assume we have a contaminated aquifer, and that we are tasked with remediating the aquifer using a pump-and-treat system. We assume the use of a single well for remediation, and that all of the available pumping choices in this work:

a.) are feasible from an engineering standpoint, i.e., we have pumps that can remove the necessary volume of water.

b.) do not dewater the aquifer or drive significant vertical flow

c.) successfully capture all solute, that is to say that all pumping choices will successfully prevent any migration of contaminant off site

d.) we use assumption b to further assume that the hydraulic gradient is proportional to the pumping rate, Q, as per the Theim Equation. We are thus ignoring any local gradient, assuming only the pumping drives the gradient.

Our final assumption is that the contaminant breakthrough at the remediation well is described by our breakthrough curves for the binary fields as a function of hydraulic gradient, i.e., the breakthrough curves discussed earlier in this chapter. We will examine pumping choice decisions for both the binary field with $Y_{con}$ of 6 and the field with $Y_{con}$ of 8, to see if there are any substantive differences.

### 6.5.2 The Cost Function

Our goal in this decision analysis is to minimize the total remediative cost associated with cleaning the aquifer. We set as our requirement that 95% of the total mass of contaminant in the aquifer must be removed, and this standard is used for all calculations. Once this standard has been met, we assume costs end (i.e., we do not assume that there are additional future monitoring or capital costs). Some further assumptions that we make regarding cost:

a.) Up-front capital costs for all scenarios are identical, and therefore we ignore these costs.

b.) There is no time discounting.

c.) Cost is not incurred from the energy used to pump the water. The validity of this assumption is scenario-dependent. In relatively shallow aquifers, it is probably a good assumption. In deeper aquifers, it might be questionable, depending on other factors such as the cost of energy.

d.) Cost is incurred from actually removing the contaminant from the water, and this cost is assumed to be a function of the concentration of contaminant in the water and the volume of water treated. We discuss the structure of this cost further down.

e.) Cost is incurred from maintenance on the infrastructure, i.e., maintaining pumps, treatment apparatus, etc., incurs cost. This is treated as a constant, $A_m$, units of dollars per unit time.

f.) Pumping is performed at a constant rate, Q, throughout the remediation.

Given the costs we have chosen to incorporate and those we have chosen not to, our cost function is:

$$\mathrm{Cost}_{\mathrm{total}} = A_m T + A_t Q \int_0^T f(C(t))dt \tag{4}$$

where T is the total amount of time required for cleanup, and Q is necessary to incorporate the volume of water (although it is simply another constant that can disappear into $A_t$). The constant coefficients $A_m$ and $A_t$ both have units of dollars per time. For the treatment cost function, we use the form suggested by *Yu* [2003]:

$$f(C(t)) = \ln\left(\frac{C(t)}{C_{MCL}}\right) \tag{5}$$

where $C_{MCL}$ in the concentration of minimum contaminant level. Note that $C_{MCL}$ can actually be any number we choose, as long as it is smaller than the smallest concentrations extracted from the well, so as to keep the values of the function positive. Any differences in our choice of $C_{MCL}$ can simply be absorbed into the constant coefficients.

The choice of this functional form for cost should not be taken as the absolutely true descriptor of cost as a function of concentration in all remediation scenarios. One might argue that a natural-logarithmic form would be preferable for thermodynamical reasons, particularly the exponential nature of Boltzman energy distributions and Arrhenius' description of energy activation. However, our primary reason for this form is because it reflects the fact that water with low concentrations of solute is more difficult to clean, on a marginal basis, than is water with high concentrations. Further, this formulation treats costs due to concentration differences in a consistent fashion (i.e., the cost difference between a particular concentration and one-tenth of that concentration will be the same, regardless of the actual concentration). While that might not be entirely realistic in real remediation scenarios, it is at least an unbiased assumption (unbiased in the mathematical sense, as any "choice" of model constitutes some form of bias).

Given this model, and using our binary field breakthrough curves, as noted earlier, we can now calculate costs for remediation on both binary fields. We can also perform this calculation for two different initial conditions – initial saturation of the domain, and flux-proportional line injection. These two different conditions lead to some interesting, and perhaps counterintuitive, results. We also examine how the decision changes as the relative values of $A_m$ and $A_t$ change. Costs were calculated for the entire breakthrough curve, not just the tail.

### 6.5.3 Cost Calculation Results

Cost calculations are dependent on two fundamental components, the total cost of maintenance, and the total cost of water treatment. For a scenario in which the aquifer begins saturated with solute, we would anticipate that maintenance costs (i.e., total time to remediate) will decrease as the pumping rate increases. If mass transfer was driven only diffusion, this would not be the case, as the nature of mass transfer would be unaffected by our pumping choice, but with advective processes relevant to tailing, this becomes a relevant consideration. In addition to maintenance cost changes as a function of pumping rate, we anticipate the total cost for treating the solute will decrease as the pumping rate decreases. This occurs because as the gradient decreases, the relative amount of tailing tends to decrease, and the relative mass transfer rate tends to increase (as we saw in figures 1 and 2). This creates plumes that are less costly to treat, because the average concentration of solute in the water is higher and the volume of water treated is smaller, leading to lower marginal costs for treating the water.

We illustrate this tradeoff between maintenance and treatment costs in figure 7, which shows the total maintenance cost, total treatment cost, and total cost (the sum of the two) as a function of pumping rate. The costs (y-axis) were calculated using the breakthrough curves for the binary field with $Y_{con}$ equal to 8, with the initial condition of equilibrium throughout the domain. The treatment cost constant, $A_t$, was assumed to be equal to 1 (thus "normalized" cost), and $A_m$ was assumed to be equal to $A_t$. The x-axis shows the normalized pumping rate, which is simply the pumping rate relative to the rate necessary to drive a normalized hydraulic gradient of 1 (so a normalized pumping rate of 10 drives a normalized hydraulic gradient of 10, etc.).

Both the maintenance and treatments costs demonstrate the expected behaviors, with maintenance costs decreasing as the pumping rate increases, and treatment costs increasing. Neither behavior, however, is strictly linear, due to the fact that changing the pumping rate alters the hydraulic gradient, which in turn changes the behavior of the tail. The dependence of the tail on advective properties of the aquifer is what drives the complexity of the decision. The optimal choice of pumping rate actually falls between the two extremes, which runs counter to conventional assumptions about pumping rate choices. We will discuss this further in the next section.

We can extend the results of figure 7 into a more general framework by looking at what happens when we vary the relative values of $A_m$ and $A_t$. To do this, we held $A_t$ constant, equal to 1 (as was done in figure 7). We then varied $A_m$ through a range of values, and compared the total costs. Figure 8 shows the results of these calculations, for the binary fields with $Y_{con}$ values of 6 and 8, with the costs plotted as base-10 logarithms. The y-axis of each figure shows the relative value of $A_m$ (i.e., $A_m/A_t$). The x-axis, as in figure 7, shows the normalized pumping rate choice. Therefore, looking at a cross-section of the contour plot for $Y_{con}$ equal to 8, with $A_m/A_t$ equal to 1, gives figure 7. The optimal choices, which can be somewhat difficult to discern in some cases, are indicated explicitly by the heavy dashed line. Optimal decisions tend to favor low pumping rates when $A_m/A_t$ is low, and faster rates as the ratio increases. This is true for both fields, though the exact details differ.

We performed a similar set of calculations for our simulations in which solute was injected in a flux-proportional line into a clean aquifer. The results are shown in figure 9. This scenario shows similar general behavior to the costs in figure 8 – optimal pumping rates tend to increase as $A_m/A_t$ increases. Again, the specifics vary, and in some cases contradict normal assumptions about the optimal pumping rate, as we discuss in the next section.

### 6.5.4 Optimal Pumping Rate Discussion

The existence of an advective component to mass transfer, in addition to the diffusive component, drives the interesting behavior we see in figures 8 and 9. Advective mass transfer is controlled by the hydraulic gradient, which is controlled by our pumping choice. Therefore, our pumping choice affects the mass transfer characteristics of the solute, affecting both the total time to remediate and the tail of the plume.

This behavior runs counter to normal assumptions about mass transfer, which ascribe a rate and amount of mass transfer that is unaffected by the advective processes. Consider the scenario in which the aquifer begins with equilibrium solute concentration throughout both the mobile and immobile domain. Conventional formulations of mass transfer would suggest that the most cost-effective strategy is to pump as slowly as possible (within the limit that pumping must successfully capture the entire contaminant plume). This decision is driven by the assumption that the speed of mass transfer will be the same regardless of choice, and thus pumping harder forces one to treat larger volumes of water (with lower concentrations), without any improvement in the duration of remediation. Once we incorporate an advective component of mass transfer, we can speed up the total time to remediate. Whether that is favorable or not from a cost standpoint depends on how large maintenance costs are relative to treatments costs.

Figure 8 reflects this idea that the existence of an advective component to mass transfer does not necessarily mean that faster pumping rates are preferable. At relatively low values of $A_m/A_t$, relatively low pumping rates are still optimal. This is because the maintenance cost becomes a relatively minor part of the total cost at such low values of $A_m/A_t$, so decreasing the total remediation time does not compensate for the higher treatment costs at high pumping rates (which drive greater tailing). We can also see the effect of having a field in which diffusive mass transfer tends to be the dominant process (field with $Y_{con}=8$) as compared to a field in which advective mass transfer is dominant (field with $Y_{con}=6$). In the field with $Y_{con}$ equal to 6, it is much easier to mobilize solute through gradient changes, and thus easier to speed up the overall process of cleaning the aquifer. This is reflected in the fact that optimal pumping choices for the field with $Y_{con}$ equal to 6 generally have higher pumping rates for most values of $A_m/A_t$ – a field in which advective mass transfer is more important is more impacted by the positive effects of increased advective mobilization of solute from low velocity regions.

The initial conditions in which we introduced a flux-proportional line of solute into a clean aquifer seem to yield less interesting results (figure 9), but the actual competition of various processes is actually more complex. Generally, when one considers remediation of an "instantaneous" contamination, there are two possible choices in the presence of diffusive mass transfer. One is to pump as quickly as possible, in order to prevent solute from having sufficient time to diffuse into the immobile domain. If this is impractical, i.e., the aquifer cannot be pumped fast enough to prevent significant mass transfer, the usual choice is to pump as slowly as possible (see *Yu* [2003] for a detailed explanation of why this is the case). As with the other initial conditions, our results suggest that the decision is not so simple.

The assumption of mass transfer only being controlled by diffusion leads to the desire to pump quickly in the case of an instantaneous injection – if most of the solute can be removed before it has time to enter the immobile domain, large costs from lengthy remediation might be avoided. But with the presence of advective mass transfer, there exists a mass transfer that is "unavoidable", in a sense – no matter how fast the well is pumped, some significant portion of the solute will move into low velocity areas. This would tend to bias decisions against fast pumping rates. On the other hand, pumping slowly can still potentially drive a great deal of mass transfer, as diffusive processes begin to contribute to tailing as well, and pumping slowly carries with it added costs in maintenance. It appears, in the end, that faster pumping, despite still driving tailing, is generally preferable to slower pumping in our binary fields. The preference for faster pumping seems more pronounced in the field in which diffusive mass transfer dominates (field with $Y_{con}$ equal to 8). This stands to reason given our suggestion that diffusion-driven mass transfer would tend to bias our decision in favor of faster pumping, as mentioned. In the field with $Y_{con}$ equal to 8, advective mass transfer is less of a problem, and thus higher pumping rates do a better job of preventing mass transfer, with the added bonus of decreasing the total elapsed time of remediation.

## 6.6 Conclusions

The memory function model of mass transfer is typically formulated in a way that assumes g(t) (the memory function) is a fixed parameter of the aquifer, the product of the geometries of effectively immobile regions. However, our work through chapters 3 through 5 suggests, and our work in this chapter confirms, that this assumption about the nature of g(t) is not always true. As with the case of our comparing macrodispersive and mass transfer models, this is not to say that the conventional description is never correct, only that there might be situations that do not fit into that formulation. We show that the memory function can include an advective component, by demonstrating that g(t) changes as the effective gradient to the aquifer changes. This means that it might be possible for a parameter that can be controlled externally, the hydraulic gradient, can affect the nature of mass transfer.

Despite the fact that the memory function model does not incorporate an advective component, it seems to be capable of predicting late-time breakthroughs from altered initial conditions, as we were able to test with dirac-input of solute mass. This effectiveness holds true even when mass transfer is controlled completely by advection. Although this result seems accurate for our binary fields, it may not be generally true for all fields, but it does suggest that the memory function model is probably a useful formulation of mass transfer, assuming it is altered to account for advection-driven mass transfer.

The effects of simultaneous advective and diffusive processes driving mass transfer tend to be additive in our binary fields. Generally, the rate of mass transfer in the joint case (i.e., simulations in which both processes occur) was found to be at least equal to the sum of the rates of both cases individually. In some cases, it was found that the rate in the joint case actually exceeded the sum of the two cases individually, which we suggest is due to diffusion from slower low velocity paths into faster low velocity paths, paths which clean out more quickly. Again, our conclusions seem accurate for our binary fields, but general applicability may be limited, as demonstrated by the results from our advective mass transfer experiments using cylindrical emplacements (although these experiments do confirm a g(t) dependence on hydraulic gradient).

Lastly, we apply what we have studied, both in this chapter and previous chapters, to a simple pump-and-treat remediation scenario. We conclude that the existence of advective mass transfer in addition to the diffusive mass transfer changes the conventional choices of pumping rate. By pumping faster when the domain begins at an equilibrium initial concentration of solute, we are able to mobilize a larger percentage of the total solute mass more quickly, which can impact our decision if maintenance costs are a significant factor in our costs. However, the existence of advective mass transfer causes problems when we attempt to remediate an aquifer immediately following an “instantaneous” injection. In this case we cannot avoid mass transfer by simply pumping solute out of the aquifer quickly, and thus are left with an optimal decision that might not be as simple as the conventional “pump fast” approach.

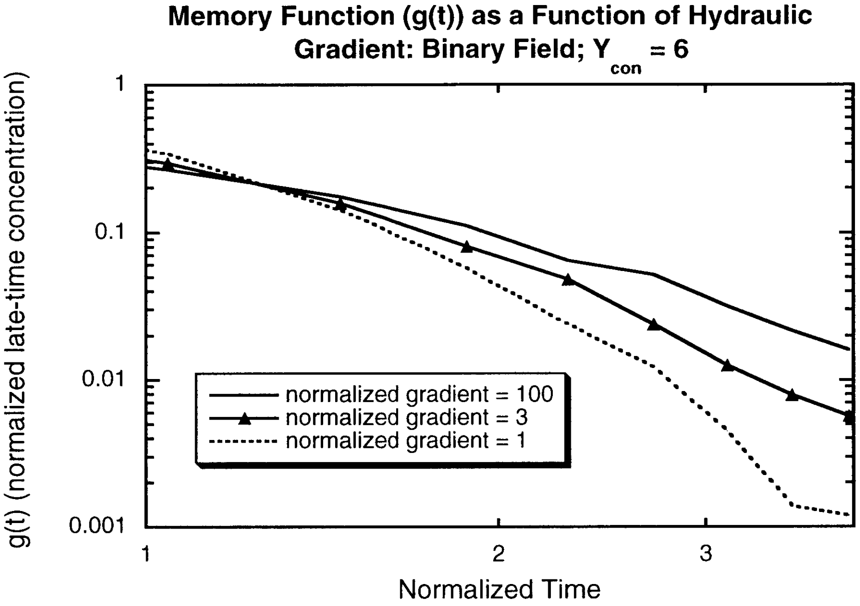

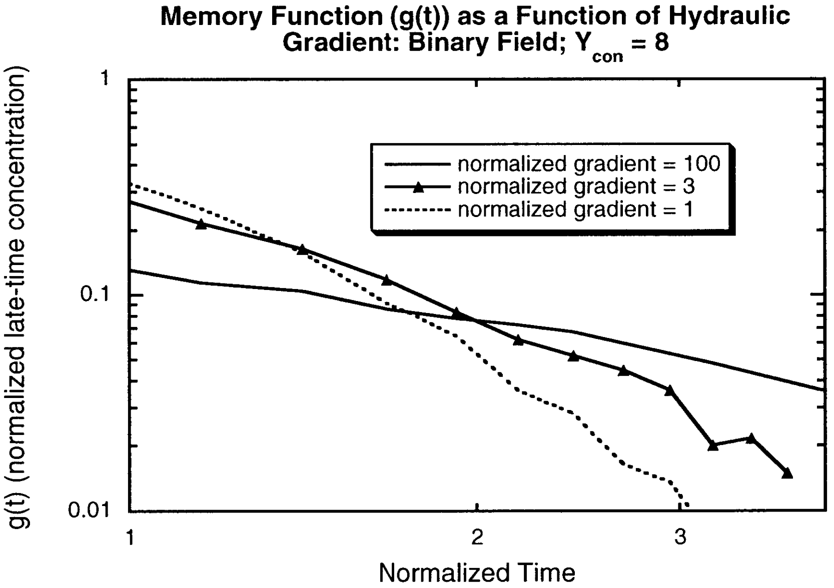

**Figure 6-1:** Memory function, g(t), as a function of hydraulic gradient, shown for the binary fields with $Y_{con}$ = 6 and $Y_{con}$ = 8. The memory function is equal to the normalized late-time breakthrough concentration when the domain has equilibrium initial conditions. Both the magnitude and "slope" of g(t) are clearly gradient-dependent, contrary to the usual.assumption of g(t) as a fixed aquifer parameter

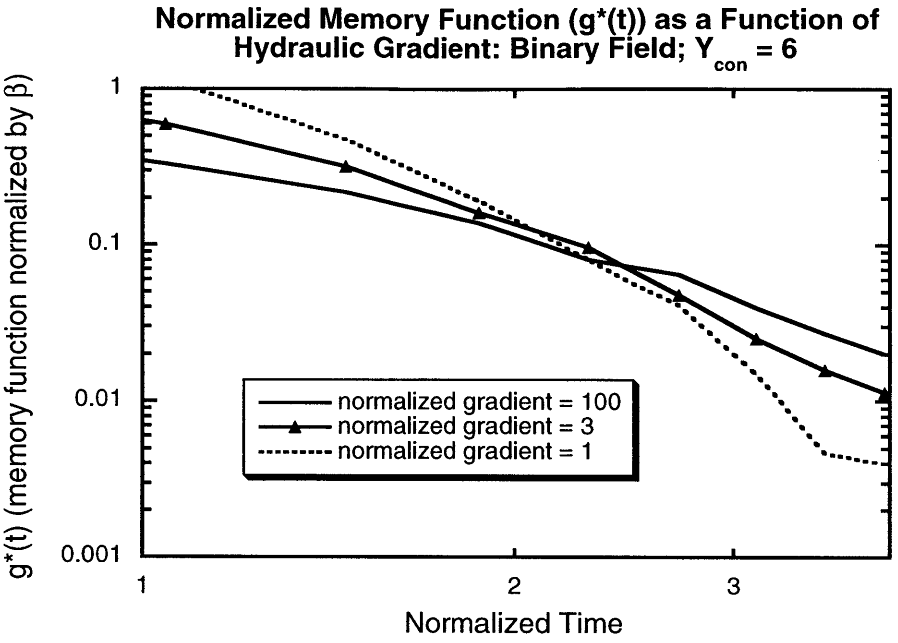

Normalized Memory Function (g*(t)) as a Function of Hydraulic Gradient: Binary Field; $Y_{con}$ = 6

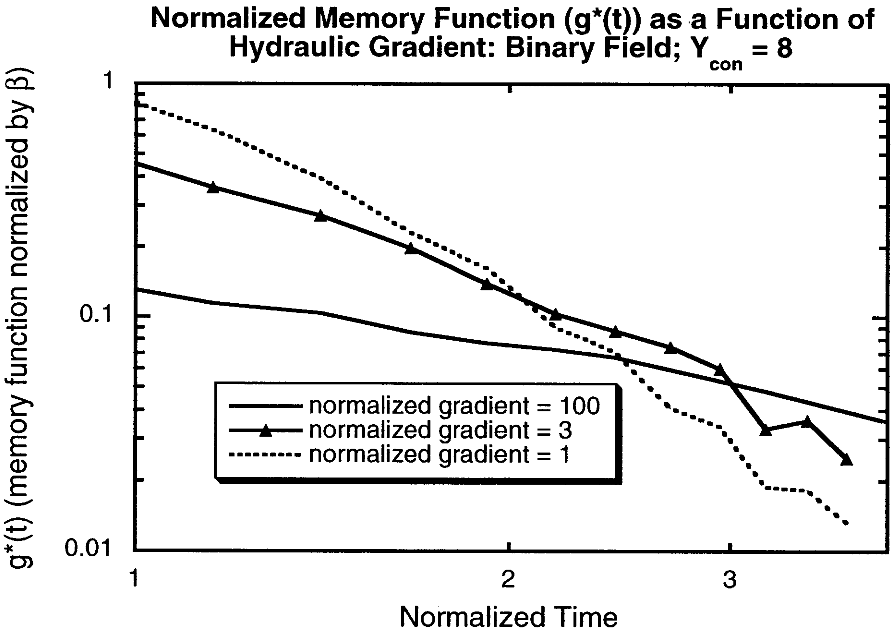

Normalized Memory Function (g*(t)) as a Function of Hydraulic Gradient: Binary Field; $Y_{con}$ = 8

**Figure 6-2:** Normalized memory function, g*(t), as a function of hydraulic gradient, for same gradients and fields as figure 1. The function g*(t) is equal to g(t) divided by β, allowing for a comparison between mass transfer scenarios where the total size of the immobile domain, as indicated by β, differs. Normally, g*(t) is not considered to have significant dependence on advective properties of the domain.

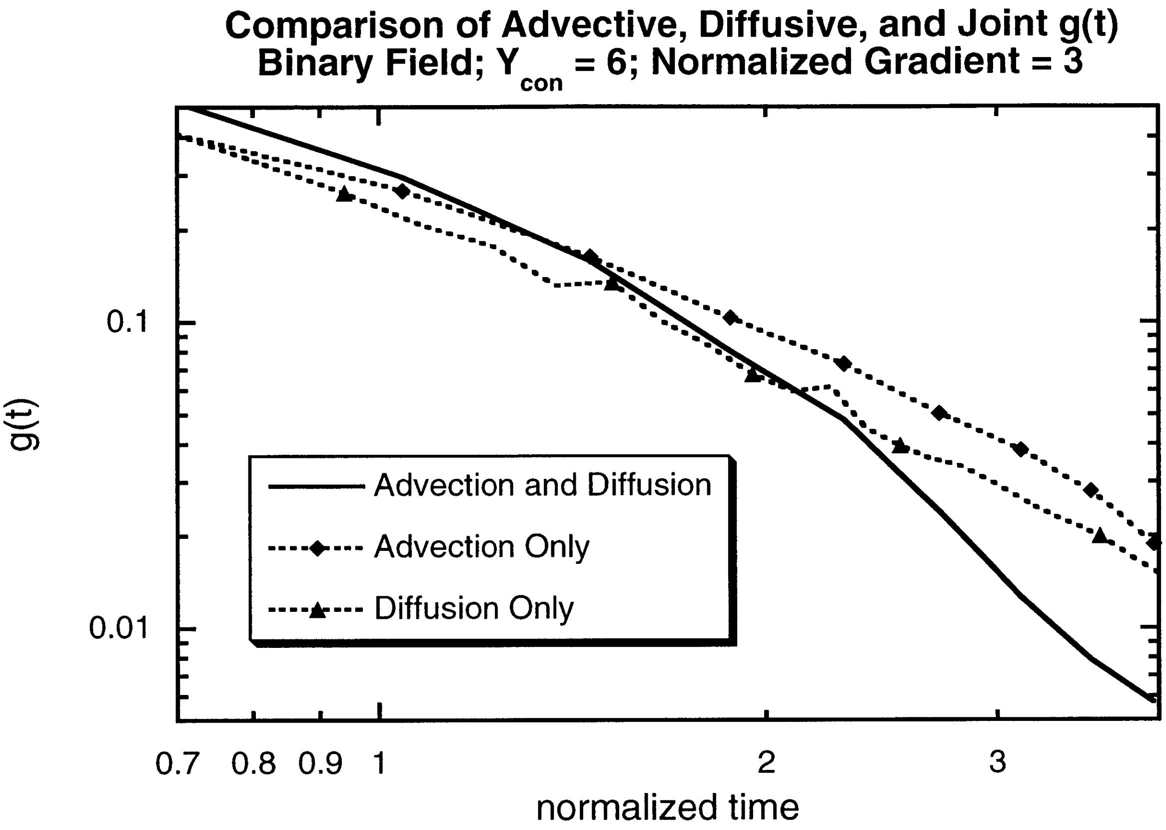

**Figure 6-3:** Memory function (g(t)) for a simulation with both advective and diffusive mass transfer, compared with simulations with only one of the two processes (advective case calculated by simulation with no diffusion, diffusive case by simulation of in field with $Y_{con}$ of 15, insuring almost no slow advection). The slope of the combined case is substantially sharper than either process individually, suggesting that the two processes tend to be reinforcing.

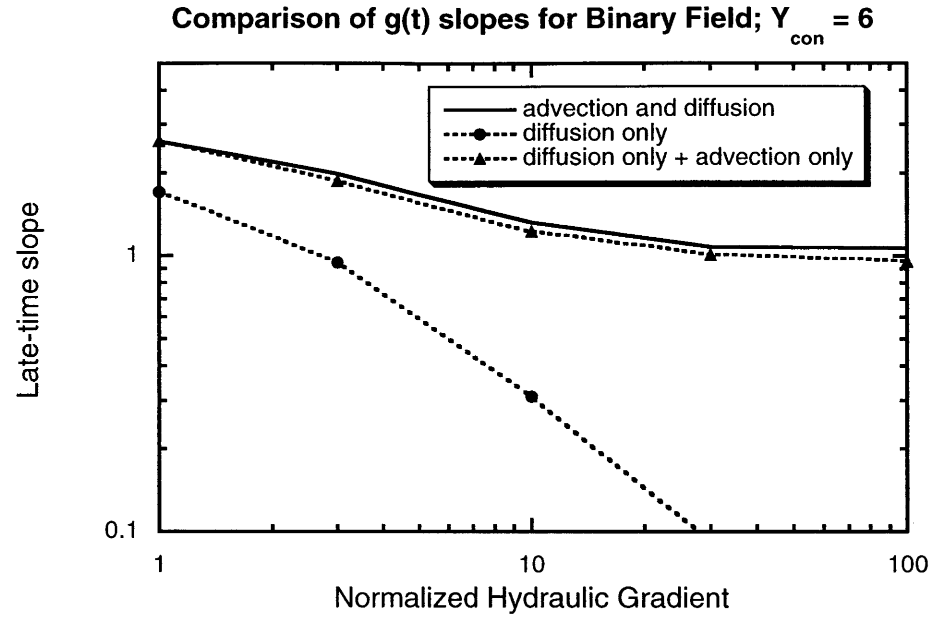

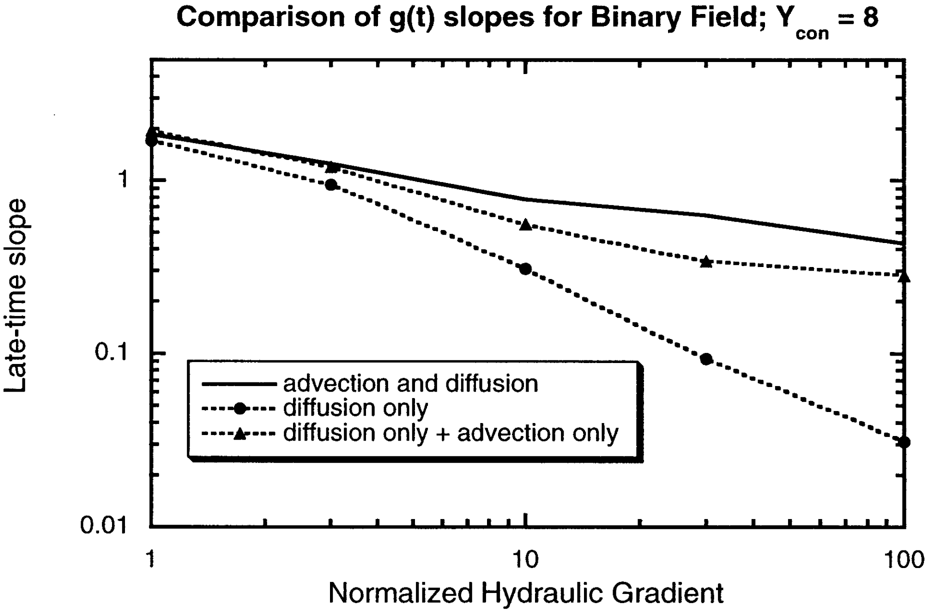

**Figure 6-4:** Slope of g(t) as a function of normalized hydraulic gradient for the binary fields with $Y_{con}$ equal to 6 and 8. One line represents the (absolute value) slope of g(t) for the case with advective and diffusive mass transfer, one represents the case where only diffusive mass transfer occurs, and one indicates the sum of the slopes of the advection only and diffusion-only cases. The results suggest that the two processes tend to be reinforcing, in some situations reinforcing to a degree that they drive overall mass transfer that is faster than sum of its components.

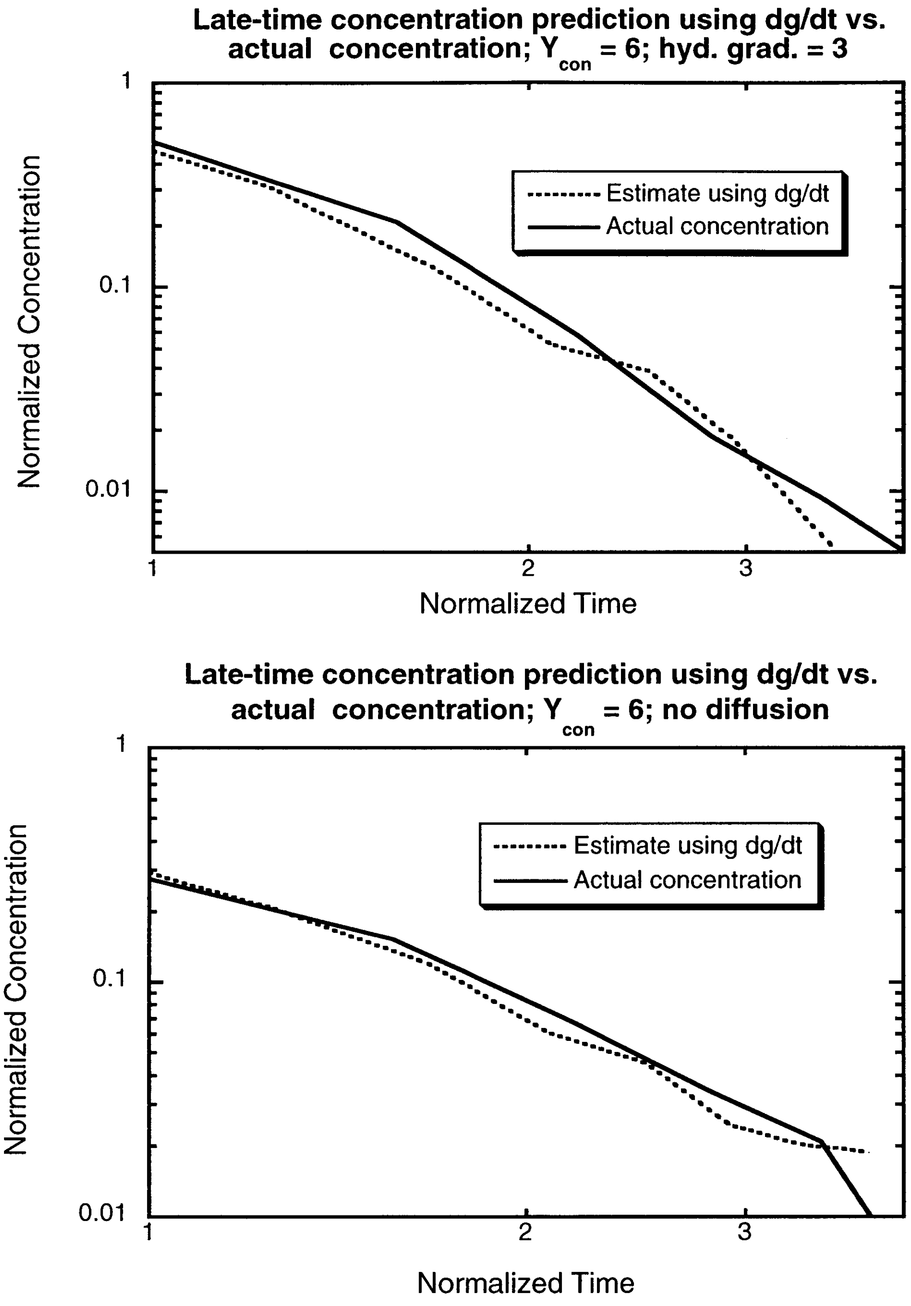

**Figure 6-5:** Prediction of late time concentration using memory function method compared to actual concentration. Prediction utilized g(t) (see figure 1) to predict the late-time concentration when a dirac-impulse is introduced into the system, using the time derivative of g(t). Actual late-time concentration is from particle-tracking simulations done with a flux-proportional line of particles introduced into the field. The memory function appears to, overall, provide a very good prediction of the breakthrough curve of the dirac-input at late time.

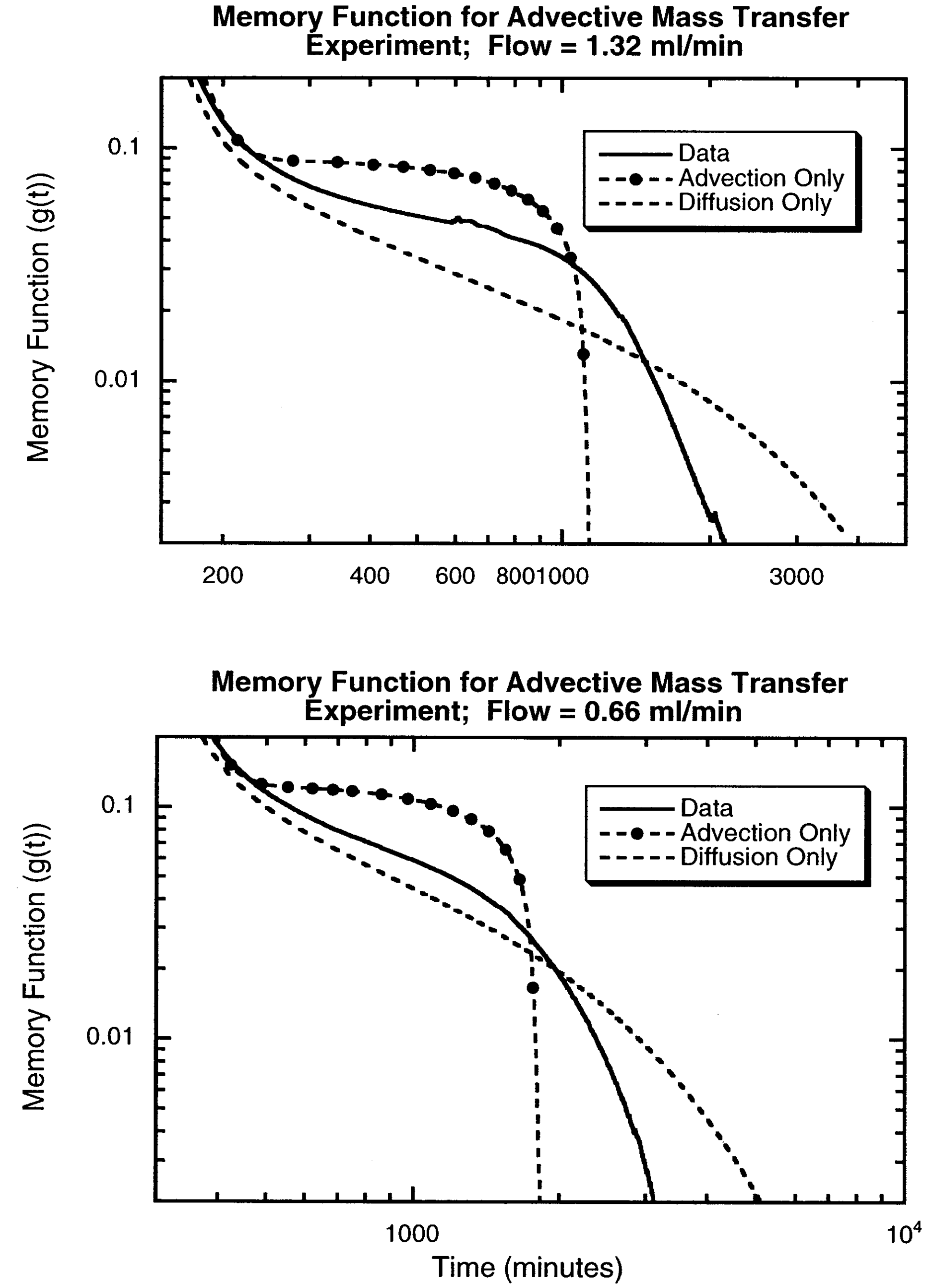

**Figure 6-6:** Memory function (g(t)) for our earlier experiments with slow advection and diffusion through cylinders. Also plotted are g(t) for diffusion-only mass transfer in the cylinder and g(t) for advection-only mass transfer (no longitudinal dispersion/diffusion). Unlike the case of the binary fields, g(t) does not appear to be easily predicted by a simple linear combination of the two processes. This suggests that our conclusions from the binary field simulations are not necessarily applicable to more complex mass transfer scenarios. It does, however, display a behavior found in our binary fields – g(t) is partially dependent on the hydraulic gradient.

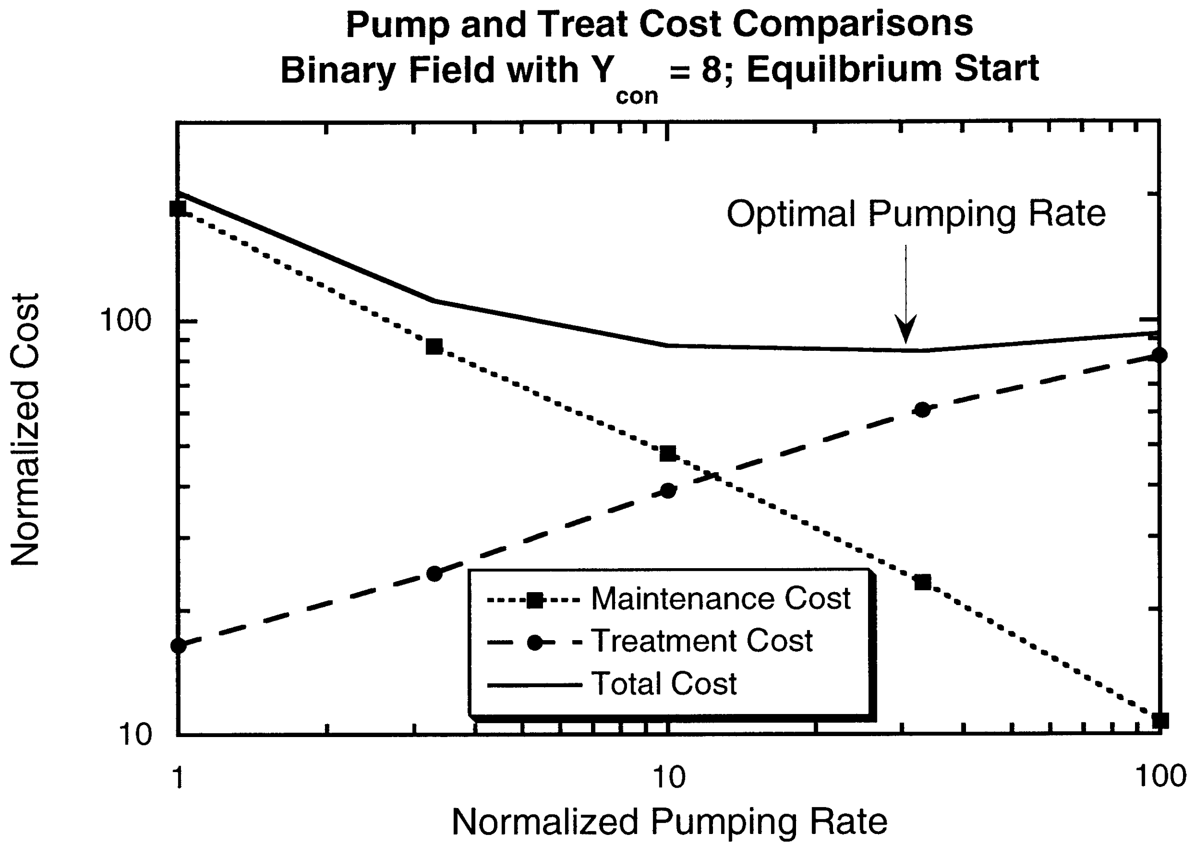

**Figure 6-7:** Costs incurred from a hypothetical pump-and-treat system. The aquifer (binary field with $Y_{con}$ = 8) is initially equilibrium-saturated with contaminant, and the remediation requirement is that 95% of the total mass must be removed. Maintenance costs decrease as pumping rate increases because total time to remediate decreases. Treatment costs increase with the pumping rate, because more of the solute is in the tail of the plume. The optimal pumping rate falls between the maximum and minimum pumping rates, whereas standard theory would dictate pumping as slowly as feasible.

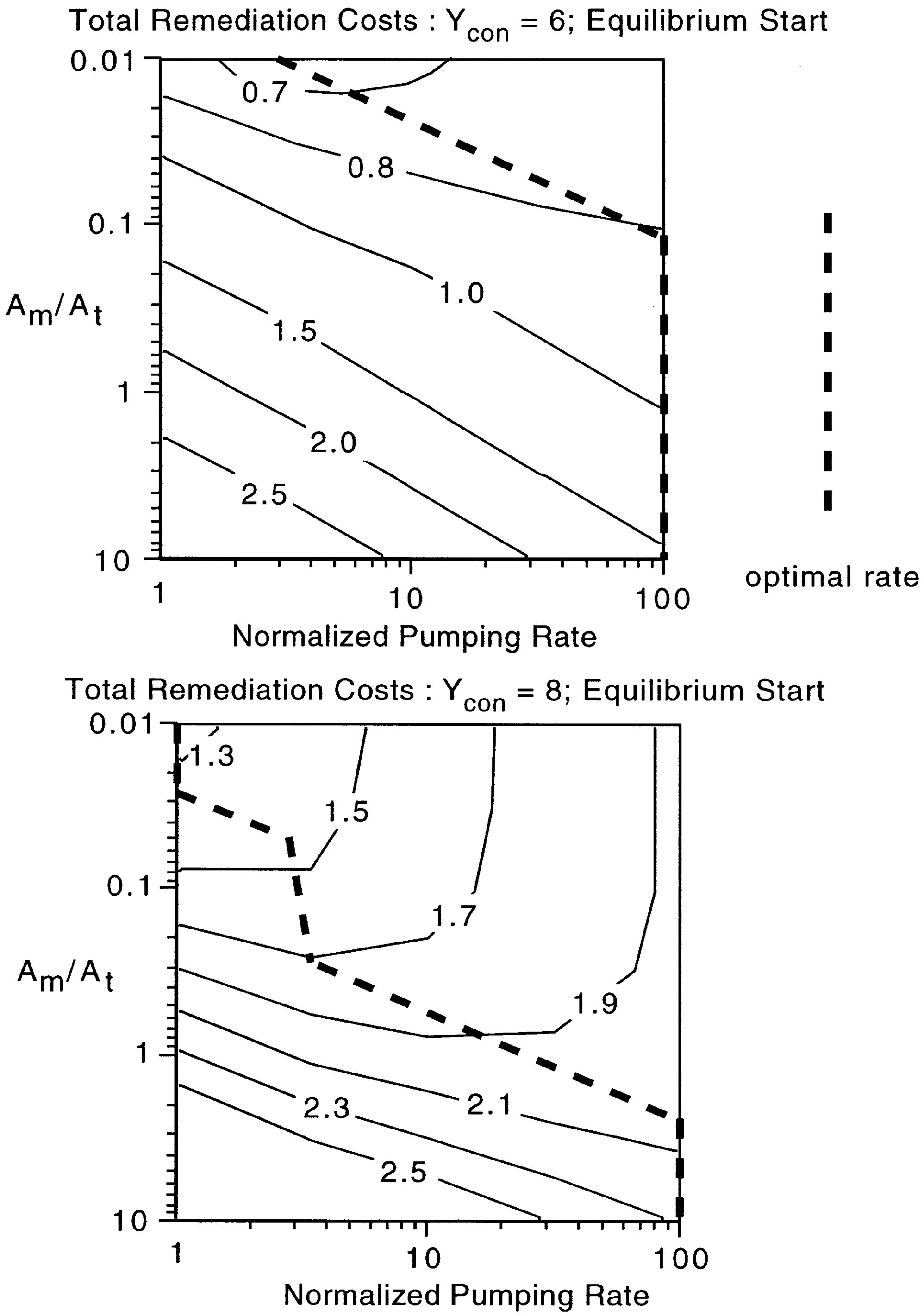

**Figure 6-8:** Total remediation costs for two binary fields ($Y_{con}$ = 6 and 8) as a function of pumping rate. Aquifers begin equilibrium-saturated, and goal is to clean up 95% of total contaminant mass. Optimal rates are indicated by the dashed line. The x-axis indicates pumping rate, while the y-axis shows the ratio of the maintenance cost coefficient ($A_m$) to the treatment cost coefficient ($A_t$) (units of money divided by time). The existence of mass transfer that can be driven by changes in head gradient creates a more complex decision than usually considered.

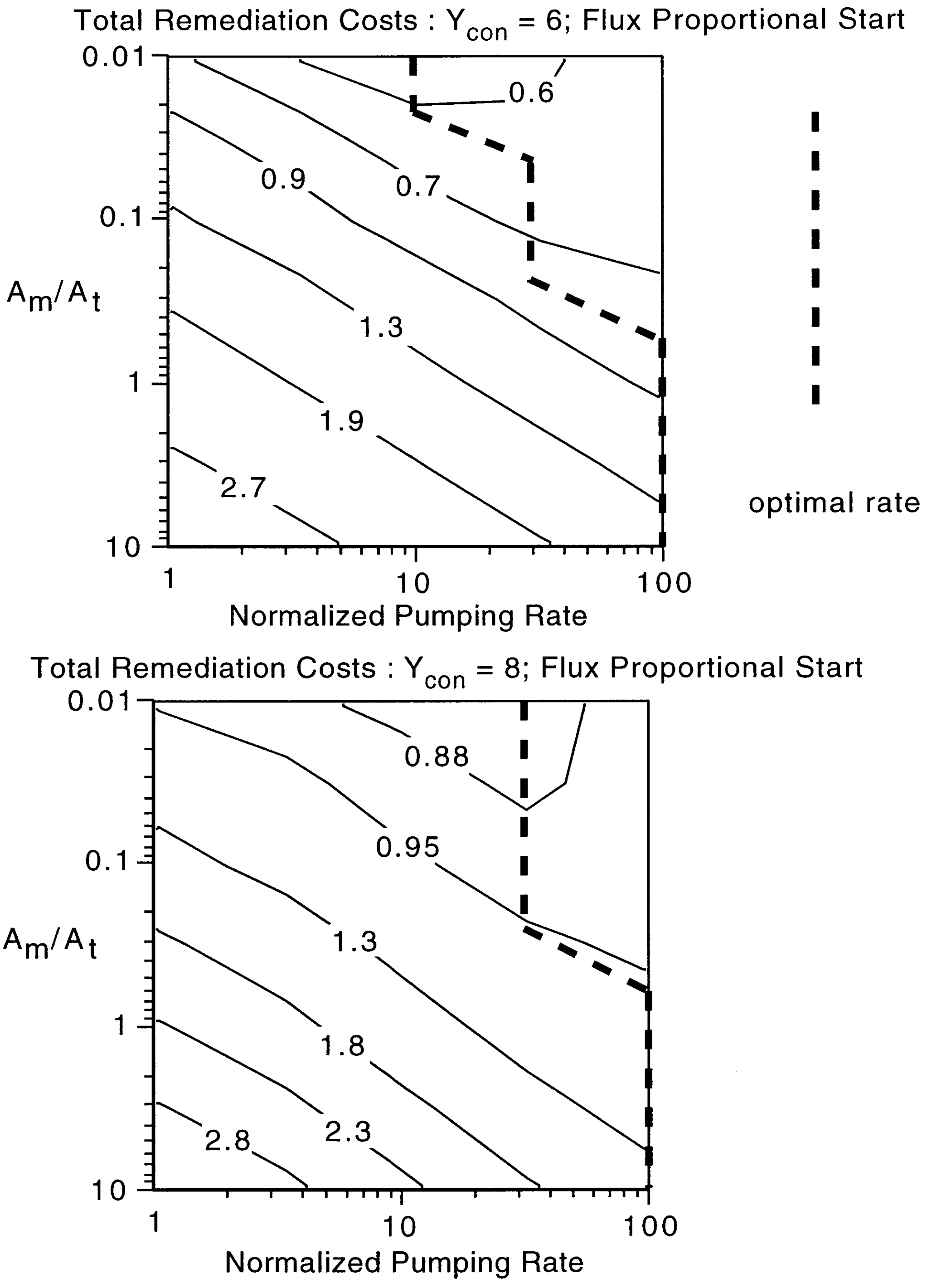

**Figure 6-9:** Total remediation costs for two binary fields ($Y_{con}$ = 6 and 8) as a function of pumping rate. Aquifers begin with an instantaneous injection of solute, and goal is to clean up 95% of total contaminant mass. Optimal rates are indicated by the dashed line. The x-axis indicates pumping rate, while the y-axis shows the ratio of the maintenance cost coefficient ($A_m$) to the treatment cost coefficient ($A_t$). Conventional theory suggests either pumping very quickly or very slowly, but we see some pumping choices that fall between the extremes.

# Chapter 7

# Conclusions and Future Work

The research in this thesis consists of a general examination of the structural characteristics of hydraulic conductivity and the effect that these characteristics have on fluid flow and solute transport. Of particular focus were connected structures of either high or low conductivity, which go against the underlying assumptions of the stochastic equations from which macrodispersive theory is developed. Our primary interest in solute transport was in discovering conditions that lead to tailing for conservative solutes, a situation that requires use of a mass transfer model to describe solute transport behavior instead of a macrodispersive model.

Although connected structures of low conductivity were found to create barriers to flow, resulting in mean fluid velocities lower than predicted by the multigaussian model, overall transport in these fields was well described by a dispersion model of solute transport. This was true in both continuous and binary fields.

It was in fields with connected structures of high conductivity that we were able to find mass transfer behavior. These fields display mean fluid velocities higher than predicted by the multigaussian model. At relatively high variances, both continuous and binary fields with this property possessed breakthrough curves that required a mass transfer model to properly explain. These results suggest that in addition to calculating the mean and variance of hydraulic conductivity, the connectedness of an aquifer may be a vital component of its characterization.

In our studies of mass transfer in connected fields, we also found that advective processes can drive, and in some cases dominate, mass transfer. Most models of mass transfer do not consider an advective component to mass transfer, yet this component may be extremely important, as it is one that can hypothetically be controlled externally by imposing changes to the hydraulic gradient.

We supplemented our simulations by visualization experiments, confirming that these processes can actually occur in a real porous medium, and occur in connectedness characteristics and conductivity contrasts that are in agreement with our simulations. The experiments allow a detailed small-scale study of solute transport while simultaneously measuring upscaled solute transport, confirming that these smaller scale processes, such as advective and diffusive mass transfer, do lead to fundamentally different upscaled behaviors.

In the final chapter, we examined the implications of our work on one particular general model of mass transfer, the so-called memory function model. We found that the existence of mass transfer that is dependent on advective processes leads to a memory function that is dependent on the hydraulic gradient. This runs counter to the usual assumption of the memory function as an intrinsic property of the aquifer, unaffected by external forcing. The model does appear to be effective, however, at predicting late-time breakthrough for different initial conditions, suggesting that the memory function model may be a model of mass transfer into which advection can be incorporated with relative ease.

As a final piece of the work, we applied our earlier work to a hypothetical pump-and-treat remediation scenario. We particularly focused on the importance of advective mass transfer, a behavior that was affected by our choice in pumping rate. Our ability to control mass transfer to a degree through our pumping choice created complex tradeoffs that resulted in sometimes counterintuitive pumping rate choices, both for situations in which an aquifer begins at equilibrium with a contaminant, and in remediating “instantaneous” spills.

As noted in the introduction of this work, this research leaves open numerous avenues of future research, topics too vast to be dealt with in the context of this thesis.

Many research questions remain on methods to characterize connectedness in aquifers. In this research, we have taken the approach of “we know it when we see it”, which is pragmatic but not intellectually elegant or complete. The question remains, what are the best methods of describing connectedness? Is it a parameter that can be summarized with a single function, like the covariance? Is it simply a higher-order correlation parameter? Or would it be better to characterize it with an effective parameter, such as the effective conductivity?

There is also the question of what connectedness, however we choose to characterize it, means to solute transport. How "connected" does a field need to be in order to drive mass transfer behavior? Is the transition between a fundamentally connected and fundamentally unconnected field sharp, as in the case of fracture flow with its percolation threshold, or is it gradual? Surely not all connected fields can drive mass transfer behavior – we could imagine a case of a high permeability matrix with embedded elliptical inclusions with strong anisotropy perpendicular to flow. In such a case flow would almost certainly tend to act more like the behavior observed in a disconnected field. Can we account for this behavior in our method of describing connectedness?

Our solute transport work also has numerous avenues of potential study. The most obvious, though also probably the most difficult, would be in devising stochastic equations that could effectively describe solute transport through connected fields. Although we fit breakthrough curves with a mass transfer model, such fits are entirely *a posteriori*. It would be useful to develop equations with a somewhat more predictive nature, as have been developed for macrodispersion in multigaussian fields.

This research also points to the need to create a mass transfer framework that is capable of incorporating advection-driven mass transfer, perhaps by working it into the memory function model. How can we determine if advective mass transfer exists, since it difficult to distinguish from diffusive mass transfer? Our results in chapter 6 suggest that perhaps tracer tests with varying hydraulic gradients could deduce that information, or perhaps we could compare push-pull tracer results with well-to-well results.

All of our work in this thesis has used simple conservative solutes for our studies, but it is important to discern what effects connectedness would have on reactive transport, perhaps through further visualization experiments, or what effect heterogeneity in chemical properties of the subsurface could have. Would advective mass transfer processes drive fundamentally different reactive mixing than diffusive processes?

Our work has also focused exclusively on single-phase flow, but it would be an interesting study to see what effects connectedness could have on multiphase flow, such as flow in the unsaturated zone. This would be particularly interesting because multiphase flow often possesses significant positive feedback – for example, connected areas of wetting would tend to promote even more fluid flow.

Ideally, future work on how to characterize connectedness would dovetail into the future work on analytic models of transport in these fields, in a way that would be analogous to macrodispersion – i.e., by measuring the connectedness and variability of an aquifer, we would be able to predict transport in the aquifer without having to perform tracer tests. There are two potential problems to such an approach, though, the first being complexity – the equations may be extremely difficult to solve. Even assuming the problem was mathematically tractable, there is an additional issue of practicality – can we measure connectedness in an aquifer without being forced to resort to tracer tests? My own intuition is that it is unlikely, at least in most cases, particularly if the variability is quite small. In the end, it may be that we must increase our reliance on tracer tests instead of analytic predictions and models, but whether through tracer tests or conventional methods, this work suggests that we must improve our ability to effectively characterize aquifers and their small-scale properties. This is an area of research that can be approached from the angle of innovative characterization techniques or from simply applying more care using conventional methods. But it is clear that connectedness and small-scale variability can have a huge impact on the behavior groundwater and its constituents, and thus discerning these properties may be critical to our ability to model flow and transport in many aquifers.

# Appendix A

# Derivation of the Covariance Function for the Absolute Value Transform of a Multigaussian Field

Here we derive the spatial correlation function for the absolute value transform of a stationary multinormal field. We show that the length scale of heterogeneities in the transformed field is less than that of the original field by deriving an analytic relationship for the covariance of the transformed field as a function of the covariance of the original multigaussian field.

**Mean and Variance of the transformed field.**

Let x be a normally distributed ($\mu = 0, \sigma^2 = 1$) random variable, and y be the absolute value of x, $y = |x|$. Then the expected value (i.e., the mean) of y is:

$$\mu' = E[y] = \int_{-\infty}^{\infty} |x| \frac{1}{\sqrt{2\pi}} \exp\left(\frac{-x^2}{2\sigma^2}\right) dx = 2\int_0^{\infty} x \frac{1}{\sqrt{2\pi}} \exp\left(\frac{-x^2}{2\sigma^2}\right) dx = \sqrt{\frac{2}{\pi}} \qquad \text{A1}$$

Similarly, the variance of y is:

$$\sigma'^2 = E[y^2] - \mu'^2 = \int_{-\infty}^{\infty} |x|^2 \frac{1}{\sqrt{2\pi}} \exp\left(\frac{-x^2}{2\sigma^2}\right) dx - \mu'^2 = \sigma^2 - \mu'^2 = 1 - \frac{2}{\pi} \qquad \text{A2}$$

since $\sigma^2 = 1$.

**Covariance of the transformed field.**

We would like to find the correlation function $\rho'(h)$ for two transformed variables $y_1$ and $y_2$ at locations separated by a distance h as a function of the correlation function $\rho(h)$ for the untransformed variables $x_1$ and $x_2$. By definition the correlation coefficient $\rho'(h)$ is:

$$\rho'(h) = \frac{E[y_1\, y_2] - \mu'^2}{\sigma'^2} = \frac{E[y_1\, y_2] - \sqrt{\frac{2}{\pi}}}{1 - \frac{2}{\pi}} \qquad \text{A3}$$

We will find $E[y_1\ y_2]$ as a function of the cdf of the multigaussian distribution of the untransformed variables $x_1$ and $x_2$:

$$f(x_1, x_2; \rho(h)) \equiv \frac{1}{2\pi\sqrt{1-\rho^2(h)}} \exp\left[-\frac{x_1^{\ 2} - 2x_1x_2\rho(h) + x_2^{\ 2}}{2\left(1-\rho^2(h)\right)}\right] \qquad \text{A4}$$

To account for the absolute value, $E[y_1\ y_2]$ is written as the sum of four integrals, which account for the four possible sign combinations of $x_1$ and $x_2$ (both $x_1$ and $x_2$ positive, both negative, $x_1$ positive and $x_2$ negative, and $x_1$ negative and $x_2$ positive):

$$\begin{aligned} E[yy'] = & \int_{-\infty}^{0}\int_{-\infty}^{0} |x_1||x_2| f(x_1, x_2; \rho(h)) dx_1 dx_2 + \int_{0}^{\infty}\int_{-\infty}^{0} |x_1||x_2| f(x_1, x_2; \rho(h)) dx_1 dx_2 \\ & + \int_{-\infty}^{0}\int_{0}^{\infty} |x_1||x_2| f(x_1, x_2; \rho(h)) dx_1 dx_2 + \int_{0}^{\infty}\int_{0}^{\infty} |x_1||x_2| f(x_1, x_2; \rho(h)) dx_1 dx_2 \end{aligned} \qquad \text{A5}$$

The first and fourth integrals are the same and may be written:

$$I_1 = I_4 = \int_0^\infty \int_0^\infty x_1 x_2 f(x_1, x_2; \rho(h)) dx_1 dx_2 \qquad \text{A6}$$

Since $x_1$ and $x_2$ are interchangeable, the second and third integrals are also equal and may be written:

$$I_2 = I_3 = \int_0^\infty \int_0^\infty x_1 x_2 f(x_1, x_2; \text{-}\rho(h)) dx_1 dx_2 \qquad \text{A7}$$

where the only difference is that the correlation coefficient is negative (due to the absolute value transform affecting only one of the two variables) by the relation:

$$\mathrm{Cov}(a,-b) = -\mathrm{Cov}(a,b) \qquad \text{A8}$$

The solution of the first integral may be written:

$$I_1 = I_4 = \frac{\rho(h)}{4} + \frac{\sqrt{1-\rho^2(h)}}{2\pi} + \frac{\rho(h)\arcsin(\rho(h))}{2\pi} \qquad \text{A9}$$

and the second integral is:

$$I_2 = I_3 = -\frac{\rho(h)}{4} + \frac{\sqrt{1-\rho^2(h)}}{2\pi} + \frac{\rho(h)\arcsin(\rho(h))}{2\pi} \qquad \text{A10}$$

Incorporating A9 and A10 into A5, and substituting into A3 gives:

$$\rho'(h) = \frac{2\left(-1 + \sqrt{1-\rho^2(h)} + \rho(h)\arcsin(\rho(h))\right)}{\pi - 2} \qquad \text{A10}$$

Thus, the correlation coefficient for the transformed variable y is a function of the correlation coefficient of the original variable at the same separation distance h, and is independent of the correlation at other separation distances. Figure A1 shows that the correlation coefficient for the transformed variable is always less than that of the untransformed variable. Thus the connected and disconnected fields have reduced spatial correlation, and hence reduced integral scales.

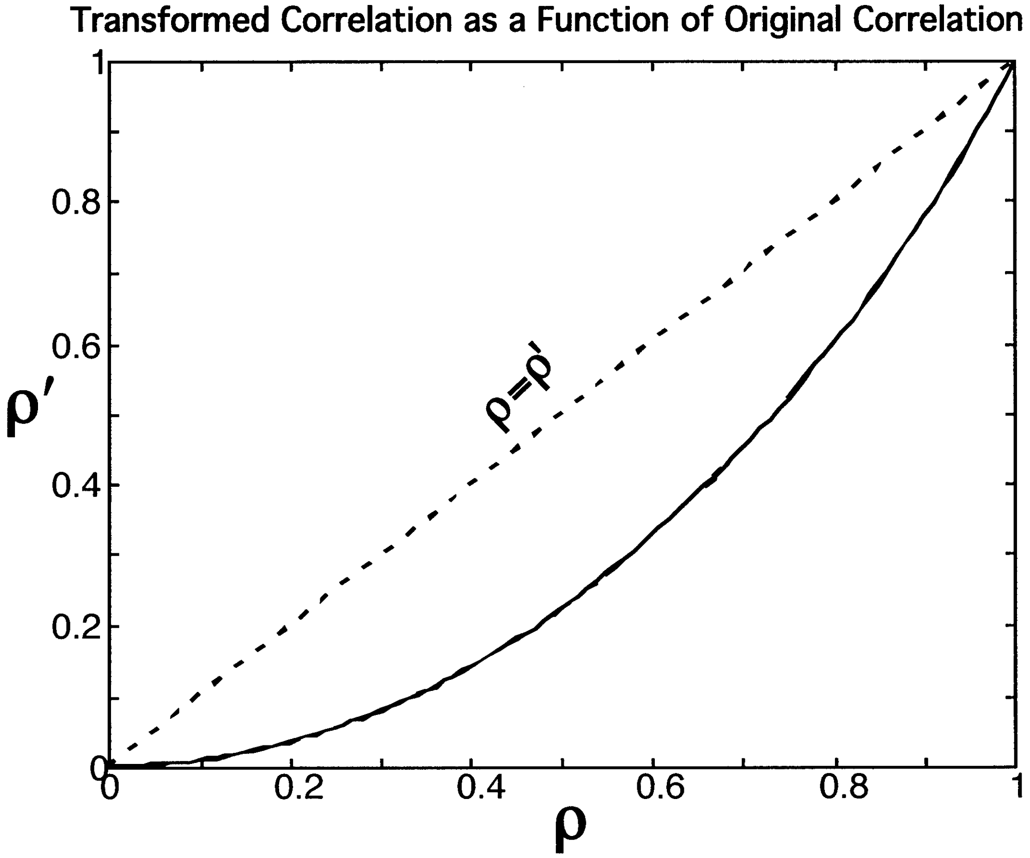

**Figure A1**: Spatial correlation after absolute value transformation as a function of the original spatial correlation. The dashed line indicates the non-transformed case (ρ=ρ′) for comparison.

# Appendix B

# Approximate Model of Advection through a Cylinder with Longitudinal Dispersion/Diffusion

In this appendix we describe the model derived for use in fitting the advective mass transfer through cylinders (see chapter 4, figure 8). We start with the results of *Dagan and Lessoff*[2001] that flow through the cylinders occurs at an approximately constant velocity. However, we do not use their derivation of the velocity inside the cylinder, which we estimate when fitting the curve.

Starting with the constant velocity assumption, we then assume that the cylinder (radius = R) begins saturated with dye, and that at time=0, the outer boundary around the cylinder changes from dye-saturated to clean. The initial condition assumption requires that flow outside the cylinder is significantly faster than inside, a reasonable approximation for our scenario. Flow in the cylinder is assumed from left to right, though this does not affect the derivation.

We have a situation where the volume out of the cylinder on the downstream side (i.e., the semicircle that constitutes the right hand side of the cylinder) will equal the volume of water in, entering on the upstream side. This will give a solute mass outflow of:

$$m(t) = C_0 \int_S \mathbf{q}(S,t) \bullet \hat{\mathbf{n}} dS \qquad \text{(B1)}$$

where S is the outflow surface (the right hand semicircle), **q** is the volumetric fluid flux of dye-saturated water (not total fluid flux), and $C_0$ is the initial concentration of solute in the cylinder.

This problem is analytically simple if we wish to only solve for advection, but more difficult to do once we add a longitudinal Fickian dispersion. In order to approximate the answer, we divide the flow into a series of horizontal streamtubes, each carrying an equal volumetric fluid flux. Each streamtube is assumed not to mix with its neighbor, but exhibits longitudinal mixing. With N tubes, total dye mass out of the cylinder is:

$$m(t) = 2\theta w_t h v_{in} \sum_{i=1}^{N} C_i(t) \tag{B2}$$

where $v_{in}$ is the (constant) velocity inside the cylinder and $C_i(t)$ is the concentration in each tube as a function of time, $w_t$ is the width of each tube (equal to the radius divided by the number of tubes), h is the thickness of the tank, and $\theta$ is the porosity inside the cylinder. From here, we use the solution for one-dimensional flow with Fickian spreading, assuming initial saturation with solute and constant flushing with clean water, to derive the concentration in each tube as a function of time:

$$C_i(t) = C_0\left(1 - \frac{1}{2}\mathrm{erfc}\left(\frac{x_i}{2\sqrt{D_{in}t}}\right)\right) \tag{B3}$$

where $D_{in}$ is the dispersion/diffusion coefficient inside the cylinder and $x_i$ is the length of each streamtube. Using our requirement that we are dividing the outflow into equally sized tubes, the lengths will then be:

$$x_i = 2\sqrt{R^2 - r_i^2} \tag{B4}$$

where $r_i$ (the distance from the center of the cylinder to the center of the stream tube) is:

$$r_i = \left(i - \frac{1}{2}\right)\frac{R}{N}, \qquad i = 1, 2, \ldots, N \tag{B5}$$

which leaves a mass release from the cylinder of:

$$m(t) = \frac{2\theta R h v_{in} C_0}{N} \sum_{i=1}^{N}\left(1 - \frac{1}{2}\mathrm{erfc}\left(\frac{x_i}{2\sqrt{D_{in}t}}\right)\right) \tag{B6}$$

with $x_i$ given by equations B4 and B5. We must choose a value of N and input values of R, $\theta$, h, and $C_0$ – leaving only $v_{in}$ and $D_{in}$ as unknowns. It is these parameters we adjust to fit to the breakthrough curve.

Lastly, we convert the mass outflow into concentration:

$$C(t) = \frac{N_{cyl}\, m(t)}{Q} \tag{B7}$$

with Q the rate of volumetric flow rate of the tank (a constant for our experiments) and $N_{cyl}$ the number of cylinders (since m(t) is the mass outflow from only one cylinder).

# References

Allaire-Leung, S.E., S.C. Gupta, and J.F. Moncrief, Dye adsorption in a loam soil as influenced by potassium bromide, *J. Env. Qual.*, 28(6), 1831-1837, 1999.

Altman, S.J., V.C. Tidwell, S.A. McKenna, and L.C. Meigs, Use of x-ray absorption imaging to evaluate the effects of heterogeneity on matrix diffusion, Characterization and Evaluation of Sites for Deep Geological Disposal of Radioactive Waste in Fractured Rocks, *Proceedings from the Third ASPO International Seminar*, SKB Technical Report, TR-98-10, 1998.

Anderson, M. P., Hydrogeologic facies models to delineate large-scale spatial trends in glacial and glaciofluvial sediments, *Geol. Soc. Am. Bull.*, 101(4), 501-511, 1989.

Anderson, T. *An Introduction to Multivariate Statistics.* New York, Wiley and Sons, 1958.

Aris, R., On the dispersion of a solute in a fluid flowing through a tube, *Proc. Roy. Soc. London.*, Ser. A, 235, 67-77, 1956.

Bahr, J. M., and J. Rubin, Direct comparison of kinetic and local equilibrium formulations for solute transport affected by surface reactions, *Water Resour. Res.*, 23(3), 438-452, 1987.

Barenblatt, G. E., I. P. Sheltov, and I. N. Kochina, Basic concept of the theory of seepage of homogeneous liquids in fissured rocks, *J. Appl. Math Mech.*, 24, 1286-1303, 1960.

Bear, J., *Dynamics of Fluids in Porous Media*, Elsevier, New York, 764 pp. 1972

Berkowitz, B., H. Scher and S.E. Silliman, Anamalous transport in laboratory-scale, heterogeneous porous media, *Water Resour. Res.*, 36(1), 149-158, 2000.

Carrera, J., X. Sanchez-Vila, I. Benet, A. Medina, G. Galarza, and J. Guimera, On matrix diffusion: Formulations, solution methods, and qualitative effects, *Hydrogeol. J.*, 6(1), 178-190, 1998.

Corapcioglu, M.Y., and P. Fedirchuk, Glass bead micromodel study of solute transport, *J. Contam Hydrol.*, 36 (3-4), 209-230, 1999.

Chen, Q., W. Kinzelbach, and S. Oswald, Nuclear magnetic resonance imaging for studies of flow and transport in porous media, *J. Env. Qual.*, 31(2), 477-486, 2002.

Cushman, J. H., edit. *Dynamics of Fluids in Hierarchical Porous Media.* San Diego, Academic Press, 1990.

Dagan, G., Solute transport in heterogeneous porous formations, *J. Fluid Mech.*, 145, 151-177, 1984.

Dagan, G. *Theory of Flow and Transport in Porous Formations.* New York, Springer-Verlag, 1989.

Dagan, G., V. D. Cvetkovic, and A. Shapiro, A solute flux approach in transport in heterogenous formations 1: The general framework, *Water Resour. Res.*, **28**(5), 1369-1376, 1992.

Dagan and Fiori, 1997, The influence of pore-scale dispersion on concentration statistical moments in transport through heterogeneous aquifer, *Water Resour. Res.*, 33(7), 1595-1605, 1997.

Dagan, G., and S.C. Lessoff, Solute transport in heterogeneous formations of bimodal conductivity distribution, 1, Theory; 2, Applications, *Water Resour. Res.*, 37(3), 465-480, 2001.

Darnault, C.J.G., J.A. Throop, D.A. DiCarlo, A. Rimmer, T.S. Steenhuis, and J.Y. Parlange, Visualization by light transmission of oil and water contents in transient two-phase flow fields, J. Contam. Hydrol., 31(3-4), 337-348, 1998.

De Hoog, F.R., J.H. Knight, and A.N. Stokes, An improved method for numerical inversion of Laplace transforms. *J. Sci. Stat. Comput.*, 3(3), 357-366, 1982.

Deng, F.-W., and J. H. Cushman, Higher-Order Corrections to the Flow Velocity Covariance Tensor, Revisited. *Water Resour. Res.*, 34(1), 103-106, 1998.

Desbarats, A.J. Macrodispersion in Sand-Shale Sequences. *Water Resour. Res.*, 26(1), 153-163, 1990.

Detweiler, R.L., S.E. Pringle, and R.J. Glass, Measurement of fracture aperture fields using transmitted light: An evaluation of measurement errors and their influence on simulations of flow and transport through a single fracture, *Water Resour. Res.*, 35(9), 2605-2617, 1999.

Deutch, C. V., A. G. Journel. Geostatistical Software Library and User's Guide (Applied Geostatistics Series). Oxford Univ Press, 1997.

Di Federico, V., S. P. Neuman, D. M. Tartakovsky, Anisotropy, lacunarity, and upscaled conductivity and its autocovariance in multiscale random fields with truncated power variograms, *Water Resour. Res.*, 35(10), 2891-2908, 1999.

Feehley, C.E., C. M. Zheng, and F. J. Molz. A dual-domain mass transfer approach for modeling solute transport in heterogeneous aquifers: Application to the Macrodispersion Experiment (MADE) site, *Water Resour. Res.* 36(9), 2501-2515, 2000.

Flury, M., and H. Fluhler, Tracer characteristics of brilliant blue FCF, *Soil Sci. Soc. Am. Jour.*, 59(1), 22-27, 1995.

Fogg, G., Groundwater flow and sand body interconnectedness in a thick, multiple-aquifer system, *Water Resour. Res.*, 22(5), 679-694, 1986.

Freyberg, D. L., A natural gradient experiment on solute transport in a sand aquifer, 2. Spatial moments and the advection and dispersion of nonreactive tracers, *Water Resour. Res.*, 22(13), 1986.

Gelhar, L. W., A. L. Gutjahr, and R. L. Naff, Stochastic anslysis of marcrodispersion in a stratified aquifer, *Water Resour. Res.*, 15(6), 1387-1397, 1979.

Gelhar, L. W., and C. Axness, 3-dimensional stochastic-analysis of macrodispersion in aquifers, *Water Resour. Res.,* 19(1), 161-180, 1983.

Gelhar, L.W. *Stochastic Subsurface Hydrology*, Prentice Hall, Englewood Cliffs, New Jersey, 1993.

Glass, R.J., S.H. Conrad, and W.J. Peplinski, Gravity-destabilized nonwetting phase invasion in macroheterogeneous porous media: Experimental observations of invasion dynamics and scale analysis, *Water Resour. Res.*, 36(11), 3121-3137, 2000.

Goltz M. N., and P. Y. Roberts. 3-Dimensional Solutions For Solute Transport In An Infinite Medium With Mobile And Immobile Zones. *Water Resour. Res.,* 22(7), 1139-1148, 1986.

Goltz, M. N., and P. Y. Roberts. Using the method of moments to analyze 3-dimensional diffusion-limited solute transport from temporal and spatial perspectives, *Water Resour. Res.*, 23(8), 1575-1585, 1987.

Gomez-Hernandez, J. J., and X.-H. Wen, To be or not to be multi-Gaussain? A reflection on Stochastic Hydrogeology, *Advances in Water Resources,* 21(1), 47-61, 1998.

Goode, D. J, Particle Velocity in Block-Centered Finite Difference Groundwater Flow Models, *Water Resour. Res.,* 26(5), 925-940, 1990.

Gramling, C.M., C.F. Harvey, and L.C. Meigs, Reactive transport in porous media: A comparison of model prediction with laboratory visualization, *Environ. Sci. Technol.*, 36(11), 2508-2514, 2002.

Griffioen, J. W., D. A. Barry, and J. Y. Parlange, Interpretation of two-region model parameters. *Water Resour. Res.,* 34(3), 373-384, 1998.

Guswa, A. J., and D. L. Freyberg, Slow advection and diffusion through low permeability inclusions, *Jour. Contam. Hydro.*, 46, 205-232, 2000.

Guswa, A. J., and D. L. Freyberg, On using the equivalent conductivity to characterize solute spreading in environments with low-permeability lenses, *Water Resour. Res.*, in press.

Haggerty, R., and S. M. Gorelick, Multiple-rate mass transfer for modeling diffusion and surface reactions in media with pore-scale heterogeneity, *Water Resour. Res.,* 31(10), 2383-2400, 1995.

Haggerty, R. and P. Reeves, *STAMMT-L: Solute Transport and Multirate Mass Transfer, User's Manual*, Sandia Natl. Lab., Albuquerque, N. M., in press, 2000.

Haggerty, R., S. A. McKenna, and L.C. Meigs, On the late-time behavior of tracer test breakthrough curves, *Water Resour. Res.*, 36(12), 3467-3479, 2000.

Harvey, C. F., and S. M. Gorelick. Temporal moment-generating equations - Modeling transport and mass-transfer in heterogeneous aquifers, *Water Resour. Res.,* 31(8), 1895-1911, 1995.

Harvey, C. F., and S. M.Gorelick, Rate-limited mass transfer or macrodispersion: Which dominates plume evolution at the Macrodispersion Experiment (MADE) site?, *Water Resour. Res.,* 36(3), 637-650, 2000.

Hess, K. M., S. H. Wolf, and M. A. Celia, Large-scale natural gradient tracer test in sand and gravel, Cape Cod, Massachusetts, 3, Hydraulic conductivity variability and calculated macrodispersivities, *Water Resour. Res.*, 28(8), 2011-2027, 1992.

Hoeksema, R. J., and P. K. Kitanidis, Analysis of the spatial structure of properties of selected aquifers, *Water Resour. Res.,* 21(4), 563-572, 1985.

Hollenbeck, K.J., C.F. Harvey, R. Haggerty, and C. J. Werth, A method for estimating distributions of mass transfer rate coefficients with application to purging and batch experiments, *Jour. Contam. Hydro.*, 37, 367-388, 1999.

Journel, A. G. Nonparametric-estimation of spatial distributions, *Math. Geol.*, 15(3), 445-468, 1983.

Journel, A. G., and F. Alabert, Non-gaussian data expansion in the earth sciences, *Terra Nova,* (1), 123-134, 1989.

Journel, A. G., and C. V. Deutch, Entropy and spatial disorder, Math. Geol., 25(3), 329-355, 1993.

Julian, H.E., J.M. Boggs, C.M. Zheng, and C. E. Feehley, Numerical simulation of a natural gradient tracer experiment for the natural attenuation study: Flow and physical transport, *Groundwater*, 39 (4), 534-545, 2001.

Koltermann, C.E., and S. M. Gorelick, Heterogeneity in sedimentary deposits: A review of structure-imitating, process-imitating, and descriptive approaches, *Water Resour. Res.*, 32(9), 2617-2658, 1996.

Kreft, A. and Zuber, A. On the physical meaning of the dispersion equation and its solutions for different initial and boundary conditions, *Chem. Eng. Sci.*, 33, 1471-1480, 1978.

LaBolle, E. M., and G. E. Fogg, Role of molecular diffusion in contaminant migration and recovery in an alluvial aquifer system. *Trans. Porous Med.,* 42, 155-179, 2001.

Lennox, W.C., and C.A. Kennedy, A pore-scale investigation of mass transport from dissolving DNAPL droplets, *J. Contam. Hydrol.*, 24(3-4), 221-246, 1997.

Matheron, G., *Elements pour une theorie des milleuz poreux*, Masson et Cie, Paris, 1965.

Matheron, G., and G. de Marsily, Is transport in porous media always diffusive? A counterexample, *Water Resour. Res.,* 16(5), 901-917, 1980.

McKenna, S. A., L. C. Meigs, and R. Haggerty, Tracer tests in a fractured dolomite 3: Double-porosity, multiple-rate mass transfer processes in convergent flow tracer tests, *Water Resour. Res.*, 37(5), 1143-1154, 2001.

Meigs, L. C., and R. L. Beauheim, Tracer tests in a fractured dolomite 1: Experimental design and observed tracer recoveries, *Water Resour. Res.*, 37(5), 1113-1128, 2001.

Norton, D.L. and R.J. Glass 1993, Full field dye concentration measurement within saturated/unsaturated thin slab of porous media, *Proceedings of High Level Radiaoctive Waste Management Conference*, Las Vegas, NV, USA, 1993.

Ogawa, K., T. Matsuka, S. Hirai, and K. Okazaki, Three-dimensional velocity measurement of complex interstitial flows through water-saturated porous media by the tagging method in the MRI technique, *Meas. Sci. & Tech.*, 12(2), 172-180, 2001.

Oostrom, M., J.S. Hayworth, J.H. Dame, O. Guven, Behavior of dense aqueous phase leachate plumes in homogeneous porous media, *Water Resour. Res.,* 28(8), 2123-2134, 1992.

Parker, J. C. and Genuchten, M. T. V., Flux-averaged and volume averaged concentrations in continuum approaches to solute transport, *Water Resour. Res.*, 20(7), 866-872, 1984.

Pollock, D.W. Semianalytical computation of path lines for finite-difference models, *Groundwater*, 26(6), 743-750, 1988.

Renard, P., and G. de Marsily, Calculating equivalent permeability: a review, *Adv. in Water Resour.,* 20(516), 1997.

Schroth, M.H., J.D. Istok, J.S. Selker, M. Oostrom, and M.D. White, Multifluid flow in bedded porous media: laboratory experiments and numerical simulations, *Adv. Water Resour.*, 22(2), 169-183, 1998.

Silliman, S.E., Particle-transport though 2-dimensional, saturated porous-media – influence of physical structure of the medium, *J. Hydrol.,* 167(1-4), 79-98, 1995.

Silliman, S.E., Laboratory study of chemical transport to wells within heterogeneous porous media, *Water Resour. Res.*, 37(7), 1883-1892, 2001.

Silliman, S. E., and A. L. Wright, Stochastic analysis of paths of high hydraulic conductivity in porous media, *Water Resour. Res.*, 24(11), 1901-1910, 1988.

Somerton, C.W., and P. Wood, Effect of walls in modeling flow through porous media, *J. Hydraulic Eng.*, 114(12), 1431-1448, 1988.

Strack, O., *Groundwater Mechanics*, Prentice Hall, Englewood Cliffs, New Jersey, 1989.

Taylor, G.I., Dispersion of soluble matter in solvent flowing slowly through a tube, *Proc. Roy. Soc. London Ser. A,* 219, 186-203, 1953.

Tidwell, V.C., and R.J. Glass, X ray and visible light transmission for laboratory measurement of two-dimensional saturation fields in thin-slab systems, *Water Resour. Res.*, 30(11), 2873-2882, 1994.

Tidwell, V.C., R.J. Glass, and W. Peplinski, Laboratory investigation of matrix imbibition from a flowing fracture, *Geophys. Res. Lett.*, 22(11), 1405-1408, 1995.

Tidwell, V. C., and J. L. Wilson, Permeability upscaling measured on a block of Berea Sandstone: Results and interpretation, *Math. Geol.*, 31(7), 749-769, 1999.

Tidwell, V.C., L.C. Meigs, T.L. Christian-Frear, and C.M. Boney, Effects of spatially heterogeneous porosity on matrix-diffusion as investigated by X ray absorption imaging, *J. Contam. Hydrol.*, 42, 285-302, 2000.

Vanderborght, J. and Vereecken, H., Solute transport in a heterogeneous soil for boundary and initial conditions: Evaluation of first-order approximations, *Water Resour. Res.*, 34(12), 3255-3270, 1998.

Welker, A. L., J.J. Bowders, and R.B. Gilbert, Applied research using a transparent material with hydraulic properties similar to soil, *Geotech. Test. Jour.*, 22(3), 266-270, 1999.

Wen, X.-H., and J. J. Gomez-Hernandez, Numerical modeling of macrodispersion in heterogeneous media: a comparison of multi-Gaussian and non-multi-Gaussian models, *J. Contam. Hydrol.,* 30, 129-156, 1997.

Western, A.W., Bloschl, G., and R. B. Grayson, Toward capturing hydrologically significant connectivity in spatial patterns, *Water Resour. Res.,* 37(1), 83-97, 2001.

Wheatcraft, W.W., and F. Winterberg, Steady state flow passing through a cylinder of permeability different from the surrounding medium, *Water Resour. Res.*, 21(12), 1923-1929, 1985.

Xiao, H. A Description of the Behavior of Indicator Variograms for a Bivariate Normal Distribution. Master's thesis, Stanford University, 1985.

Yu, W. Socio-Hydrologic Approaches for Managing Groundwater Contamination Problems: Strategies for the Arsenic Problem in Bangladesh. Doctoral Thesis, Harvard University, 2003.